Dissertations, Theses, and Masters Projects   Theses, Dissertations, & Master Projects

1997

Collision-induced secondary electron and negative ion emission from metallic surfaces

John Christopher Tucek

College of William & Mary - Arts & Sciences

Follow this and additional works at: https://scholarworks.wm.edu/etd

Part of the Atomic, Molecular and Optical Physics Commons

Recommended Citation

INFORMATION TO USERS

This manuscript has been reproduced from the microfilm master. UMI films the text directly from the original or copy submitted. Thus, some thesis and dissertation copies are in typewriter face, while others may be from any type of computer printer.

The quality of this reproduction is dependent upon the quality of the copy submitted. Broken or indistinct print, colored or poor quality illustrations and photographs, print bleedthrough, substandard margins, and improper alignment can adversely affect reproduction.

In the unlikely event that the author did not send UMI a complete manuscript and there are missing pages, these will be noted. Also, if unauthorized copyright material had to be removed, a note will indicate the deletion.

Oversize materials (e.g., maps, drawings, charts) are reproduced by sectioning the original, beginning at the upper left-hand corner and continuing from left to right in equal sections with small overlaps. Each original is also photographed in one exposure and is included in reduced form at the back of the book.

Photographs included in the original manuscript have been reproduced xerographically in this copy. Higher quality 6" x 9" black and white photographic prints are available for any photographs or illustrations appearing in this copy for an additional charge. Contact UMI directly to order.

UMI

COLLISION INDUCED SECONDARY ELECTRON AND NEGATIVE ION EMISSION FROM METALLIC SURFACES

———————————

A Dissertation
Presented to
The Faculty of the Department of Physics
The College of William and Mary in Virginia

In Partial Fulfillment
of the Requirements for the Degree of
Doctor of Philosophy

———————————

by
John Christopher Tucek
June, 1997

UMI Number: 9815245

APPROVAL SHEET

This dissertation is submitted in partial fulfillment of

the requirements for the degree of
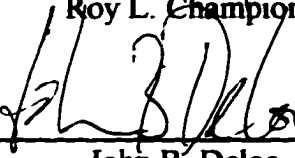
Doctor of Philosophy

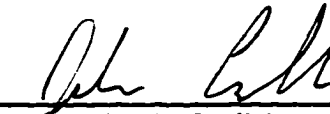John Christopher Tucek

Approved, June 1997

Roy L. Champion

John B. Delos

Gina L. Hoatson

Dennis M. Manos

John A. Carlisle
Department of Physics
Virginia Commonwealth University

ii

For Julie

iii

TABLE OF CONTENTS

ACKNOWLEDGMENTS

I would like to acknowledge several individuals whose contributions to this work have been invaluable.

My advisor, Roy Champion for his guidance and above all, his creativity. His enthusiasm for these experiments made even the most difficult days fun. Ultimately, I learned from him that all the bells and whistles are worth nothing; it is the physics that is interesting.

The members of my committee: Dennis Manos, Gina Hoatson, John Delos and John Carlisle for reading this manuscript and providing pertinent criticisms.

Sylvia Stout, Paula Perry and Dianne Fannin, for handling everything else at the College.

The members of the truck lab, Scott Walton and Brian Peko. Scott, for putting up with me on a daily basis both in the lab and at home. Brian, for always doing things in triplicate and for his great impersonations. Go golden boy! I am lucky to have these guys as friends and fellow truck drivers.

Doug Baker, for starting me down the path of surface science. His assistance gave me the tools to complete these experiments and his patience allowed me to learn from my mistakes.

My fellow graduate students especially Jim Fedchak, Julie Grossen and Chris Lasota.

Tom Venhaus, Jay Diggs and the rest of the Applied Science, for always providing a spare gasket when it was needed.

My most sincere gratitude to my Mom and Dad, for their constant love and support throughout all my life. You have always been behind me for all of my achievements.

My brother Chris, who has motivated me to wrap this up here and to go out and get a job.

Most of all, my deepest thanks and love to my best friend and wife, Julie. Her encouragement, inspiration and perseverance enabled me to complete this dissertation. She is the one who makes the rest of my life fun.

vi

LIST OF FIGURES

viii

LIST OF TABLES

x

ABSTRACT

Absolute yields of negative ions and secondary electrons resulting from collisions of positive sodium ions (Na^+) with polycrystalline aluminum (Al) and molybdenum (Mo) surfaces and the Mo (100) surface have been measured as a function of the oxygen (O) coverage at impact energies, $E < 500$ eV. The sputtered negative ions have been identified with mass spectroscopy, and negative oxygen ions (O^-) are found to be the dominant sputtered negative ions and for the three surfaces at all O coverages and Na^+ impact energies. Thus, for all practical purposes, the negative ion yield is the negative *oxygen* ion yield. For all the surfaces, the yields share a common impact energy threshold at $E_{th} \approx 50$ eV. Both the secondary electron and the O^- yields are found to have a strong dependence on the oxygen coverage of the surface. In fact, at a moderate collision energy of 250 eV, there is a two order of magnitude increase in the electron yield as the oxygen coverage of the Al surface increases from none up to a full monolayer. While the macroscopic work functions of the surfaces are observed to strongly affect the O^- emission, the work function has a significantly smaller effect on secondary electron emission. By varying the work function of the surfaces through controlling the amount of adsorbed Na on the surfaces, it was ascertained that the increase in the secondary electron yields cannot be ascribed simply to an oxygen altered work function.

Additionally, the kinetic energy distributions of the secondary electrons and sputtered O^- were determined as functions of oxygen coverages and impact energies for the three surfaces. In general, the shapes of the O^- kinetic energy distributions and the most probable kinetic energies of the ions are independent of the Na^+ impact energy, the O coverage and the metal substrate. The O^- distributions are characterized by a narrow, low energy peak (at $\sim 1 - 2$ eV) followed by a low level, high energy tail. The secondary electrons have a narrow (FWHM $\sim 1 - 2$ eV) kinetic energy distribution, centered essentially at the same most probable kinetic energy as the ions. Similar to the ions, the shapes of the distributions and the most probable kinetic energies of the secondary electrons are essentially invariant with impact energy, oxygen coverage and the metal surface.

The experimental O^- kinetic energy distributions were analyzed in terms of conventional collision cascade model, but the calculation could not be fitted to the experimental results. Without an adequate description of either the low energy sputtering event or the origin of secondary electrons, an electronic excitation mechanism is proposed to augment the collision cascade and to provide a mechanism for secondary electron emission. In this mechanism, adsorbed O, which resides on the surface essentially as O^-, is collisionally excited into an $(MO^-)^*$ repulsive state, and as the O^- exits the surface along the surface potential energy curve, it can decay by emission of an electron to the metal or to the vacuum, or it can survive as an ion. The parameters of this model can be adjusted such that the calculated ion kinetic energy distribution, together with that of the collision cascade, can reasonably reproduce the experimental observations for the ions, and also, the model can provide a reasonable fit to the corresponding electron kinetic energy distributions.

COLLISION INDUCED SECONDARY ELECTRON AND NEGATIVE ION

EMISSION FROM METALLIC SURFACES

CHAPTER 1

INTRODUCTION

A knowledge of the dynamics which underlie the secondary electron and negative ion emission resulting from low energy, ion-surface collisions and the role that adsorbates play in these processes are crucial to a full understanding of interactions at surfaces. In addition to being fundamental to the field of surface physics, the effect of adsorbates on electron and ion emission is of great practical interest since the surfaces of all functional devices are inevitably covered with some adsorbates. In fact, the results of many surface experiments performed in high vacua have been accompanied by a caveat concerning their interpretation for precisely the reason that both the extent and role of the adsorbates in the surface interactions are unknown. Experiments have indicated that secondary electron emission from clean metal surfaces, prepared in an ultrahigh vacuum, is very improbable at low impact energies [1-5]. The electron yields for these surfaces are on the order of 0.01%. Just the converse is observed for adsorbate covered surfaces where large (typically a few percent) secondary electron yields are measured routinely [6-9]. The underlying reason for the enhancement in the secondary emission is not known, nor has it been quantified to any extent. In the same sense, secondary negative ion emission from metal and semiconductor surfaces also can be increased significantly by the presence of adsorbates [10,11], and this is particularly true in the case of alkali-metal coverage of the surface [7,12,13]. While extensive research efforts have concentrated on the various aspects of sputtering and secondary electron and ion emission at high impact energies

2

[5,14-18], few results are available for well-characterized, ultrahigh vacuum prepared, metallic surfaces at impact energies below 500 eV, an energy range relevant to many areas of discharge physics where secondary emission is important in determining the equilibrium concentrations in the discharge. The primary objectives of this work are to quantify the effect of oxygen coverage upon secondary electron and negative ion emission from metallic surfaces and to develop an understanding of the role of adsorbed oxygen in the dynamics of these processes for collision energies up to 500 eV.

When ions strike a metallic surface with an impact energy of a few hundred eV, several processes can occur. First, some of the incident ions will be scattered from the surface as neutral atoms, having gained an electron in an exothermic charge transfer process. Second, energy from an incoming ion can be transferred to atoms of the surface layer through the collisions of the incoming ion with atoms and electrons of the solid. The energy transferred to a surface atom may exceed its surface binding energy, and that atom may be ejected from the surface (possibly as an ion). Third, the ion-surface collision can also lead to electron emission from the surface or photon emission from collisionally excited particles. The principal observable in studying these emission processes has been the yield, Y_i, defined as the number of *ejected* particles of type i, divided by the *incoming* particle flux.

The two main ion-induced electron emission processes at low impact energy are referred to as "kinetic" and "potential" emission. Investigations have clearly distinguished between them [1,2]. Kinetic emission can occur following a substantial momentum transfer from the incoming projectile to a conduction band electron. The center of mass

energy of the incoming particle-electron system must exceed the work function of the surface for the electron to be ejected by the collision. Accordingly, kinetic emission is only likely to occur for impact energies in the keV range, where the velocity of the incoming particle is similar to that of a conduction electron with the Fermi energy. In the potential emission process, neutralization of the incident positive ion via electron tunneling will release energy which may be transferred to another electron in the solid. That second electron can be emitted into the vacuum if the energy gained from neutralization, i.e., the ionization potential of the impacting ion, is greater than twice the surface's work function [19]. Another less likely emission process is known as kinetic Auger emission [5,20-22], in which atomic collisions can excite electrons into outer shells, creating inner shell vacancies, which are subsequently filled by an Auger mechanism. If the energy released in the hole filling is high enough, and it is transferred to a second electron, that electron can be ejected into the vacuum. Excitation leading to kinetic Auger emission can be produced through projectile-target collisions or from a recoiling target atom and another atom of the substrate. The latter process is not a significant mechanism for secondary electron emission at low impact energies.

The removal of surface atoms by particle bombardment is referred to as sputtering. First observed as the erosion of the cathode in a gas discharge [23-26], it has since been widely investigated, and the basic physical phenomena of the sputtering process are fairly well understood today. In general, sputtering can be further classified into two categories: chemical and physical. Chemical sputtering is a process by which the incident ion forms a volatile compound with atoms of the surface which subsequently desorbs from the surface.

On the other hand, physical sputtering is described as a momentum transfer process governed by the energy transferred between the incident ion and surface atoms through binary, atomic collisions. If a surface atom receives sufficient energy to overcome the surface binding energy, that atom can be ejected from the surface. The series of collisions in the solid initiated by the impinging ion is known as the collision cascade, and the cascade is said to be linear if a small number of surface atoms are set in motion by the impacting ion. In this case, the sputtering yield will be small compared to the number of atoms in the cascade, and the description of sputtering by the collision cascade is known as the Thompson-Sigmund model [27-28].

Atoms which are sputtered from the surface can acquire an electron from the metal and survive as a negative ion into the vacuum. The probability of forming a negative ion and having it survive has been described reasonably well by the electron tunneling model for clean and adsorbate covered surfaces. This theory has been discussed in detail and derived in various forms by many workers [29-35]. The electron tunneling model assumes a metal "jellium" which is characterized primarily by the Fermi level, and the work function is the difference between the Fermi level and the vacuum level. When an atom is near the surface of this jellium, the electron affinity level of the atom is shifted down by a screened image potential such that for small distances from the surface, the energy of the affinity level can lie below the Fermi level of the metal. An electron can tunnel from an electronic level in the metal to an unoccupied atomic level of the same energy by a resonant transfer process. Hence, an atom may reside on the surface essentially as a negative ion. If this negative ion is sputtered by the collision cascade, it can survive as a

negative ion due to the finite width of the atomic level. The probability that it will survive is dependent upon the exit velocity normal to the surface and the work function. Experiments performed by Yu [36] and Bernheim and Le Bourse [13] investigating the sputtering of oxygen negative ions from metal surfaces, have verified the survival probability's dependence on exit velocity. Additionally, the dependence of the survival probability on the work function was validated by varying the alkali metal coverage of the surface, which serves to lower the macroscopic work function [12].

Ion-induced electron and negative ion emission from surfaces play a critical role in any application involving the interaction of energetic ions with a surface, i.e. all plasma based phenomena. Surface generated secondary electrons and negative ions affect the sheath thickness, ion-energy distributions and equilibrium concentrations in plasmas during plasma etching [37-39]. Increased negative emission from the walls of a plasma reactor decreases the edge plasma temperature and, consequently, reduces target sputtering and changes the equilibrium concentration of the plasma. Both the yields and energy distributions of secondary electrons and negative ions are essential to the comprehensive understanding of the plasma sheath potential required for efficient and credible modeling using plasma-surface interaction codes [40,41]. For example, these factors have been identified as a source of magnetron plasma instabilities [42], where the plasma is sustained by secondary electrons emitted from the magnetron surfaces exposed to ions from the plasma. As the sputtering proceeds, the surfaces presumably will be cleaned of adsorbed oxygen, reducing the number secondary electrons emitted into the plasma, and consequently, the plasma potential increases. Initially, the increased plasma potential

generates more secondary electrons, as higher energy ions will strike the surfaces. But this also increases the rate at which oxygen is removed from the surfaces, which, in turn, lowers the yield for secondary electrons. Eventually, the yield becomes so small that the plasma can no longer be maintained, and it is extinguished.

Secondary electron emission and the sputtering of negative ions from aluminum surfaces, one of the surfaces studied here, have been particularly important in understanding ion source performance [43]. The production of highly charged ions is only possible if the discharge within the source has an adequate electron density, which has been found to depend rather strongly upon which metal is chosen for the electrodes and the containment chamber. Emission from aluminum is also fundamental to measurements of glow discharge features in a Gaseous Electronics Conference (GEC) reference cell [44,45]. The GEC reference cell is used for generating standardized, radio-frequency (rf) glow discharges and provides a common experimental platform for different research groups, eliminating such variables as reactor geometry and construction materials. The discharge in the GEC reference cell is generated by two parallel, aluminum electrodes, and the discharge "equilibrium" conditions are somewhat time dependent, presumably for reasons similar to those mentioned above for the magnetron discharge. Other areas where an understanding of secondary emission processes is important include the future development of particle detectors [46-48] and the erosion of satellite materials in low earth orbits [49].

This thesis examines secondary electron and negative ion emission from metal surfaces for impact energies below 500 eV, focussing primarily on the role of adsorbed

oxygen in these processes. Experimentally, collisions of positive sodium ions with polycrystalline aluminum and molybdenum surfaces and a molybdenum (100) surface have been investigated while the amount of adsorbed oxygen on these surfaces was varied from none up to several monolayers. Sodium was chosen as the positive ion probe beam, as its ionization potential is well below that required for secondary electron emission via the potential emission process. Aluminum (Al) is the most abundant metallic element on the surface of the earth, having an atomic number of 13 and an atomic mass of 27 amu. The electronic configuration of an Al atom is $1s^2 2s^2 2p^6 3s^2 3p^1$. It was the first surface selected for investigation for several reasons. First, an Al surface adsorbs oxygen rather slowly, and the secondary electron and negative ion yields from an Al surface are large, making the experimental measurements somewhat easier to complete. Second, the oxygen adsorption process [50] and the adiabatic interaction of oxygen *negative ions* with Al surfaces [51] has been studied extensively. Molybdenum (Mo) was investigated to augment the previous investigations by Baker, et al. [7] of gas covered Mo surfaces. Also, Mo is considerably more massive than Al, having an atomic mass of 96 amu, providing a substrate mass comparison. Mo has an atomic number of 42 and an electronic configuration of $[Kr]4d^5 5s$. Molybdenum metal is used in high temperature applications due to its high melting point (2617 °C), and molybdenum oxides are used as industrial catalysts. Investigations of the Mo (100) surface provide for even greater surface characterization, specifically, the orientation of O and Mo atoms on the (100) surface.

In what follows, the absolute probabilities for emission of secondary electrons and negative ions have been measured as functions of oxygen coverage and impact energy.

The kinetic energy distributions of the secondary electrons and ions have been determined, and the sputtered negative ions have been identified with a quadrupole mass analyzer or via time of flight mass spectroscopy. The possibility of simultaneous, correlated electron-negative ion emission also was investigated. The experimental results for negative ion emission will be analyzed in terms of conventional models, and their deficiencies will be illustrated. Ultimately, a proposed model, employing an electronic excitation mechanism for AlO^- (MoO^-), will be presented to augment the conventional ion emission model and, at the same time, provide a mechanism for secondary electron emission at low impact energies. A portion of this thesis concerning the Al target has been reported in the following publications:

"Secondary-electron and negative-ion emission from Al: Effect of oxygen coverage," J. C. Tucek, S. G. Walton and R. L. Champion, Phys. Rev B **53**, 14127 (1996).

"On the dynamics of secondary-electron and anion emission from an Al/O surface," J. C. Tucek and R. L. Champion, Surf. Sci. **xxxx**,xxx (1997).

CHAPTER 2

EXPERIMENTAL METHOD

2.1 Apparatus

The experimental apparatus was constructed specifically for the investigation of low energy, ion-surface collisions with several goals in mind. First, it was designed to provide *in situ*, well-characterized surfaces upon which to perform the experiments. Second, elements were included to identify the negative products of the ion-surface collisions and to measure their kinetic energies. Last, and most importantly, the apparatus was designed to make absolute yield measurements of the collision-induced, secondary negative products. The negative ion yield, Y_X^-, is defined as the ratio of sputtered negative ions to incident positive ions, and similarly, the secondary electron yield, Y_e^-, is the ratio of secondary electrons emitted to the incident positive ions. The total yield, Y_T^-, is defined as the sum of the two: $Y_T^- = Y_X^- + Y_e^-$. During the course of this work, the apparatus was in a constant state of evolution and underwent several major modifications, instigated by the experimental results themselves. It will be described in its latest state and previous modifications will be noted. Though the specific intentions of each modification may have varied, two intentions always were to ensure absolute collection efficiency of the ejected negative products and to provide for better surface characterization.

The apparatus consists of three major systems: the vacuum chamber and its vacuum pumps, a gas handling system and the internal experimental components and their associated electronics. The experiments were conducted in an ultrahigh vacuum (UHV)

10

chamber schematically shown in Fig. 2.1. The main chamber is a metal-sealed, stainless steel, Varian FC-12E Table Top vacuum chamber sealed with a Wheeler flange. All other seals are made with Conflat flanges with oxygen-free, high-conductivity copper gaskets. The vacuum in the main chamber is maintained by a 260 ℓ/s turbomolecular drag pump, five 50 ℓ/s sputter ion pumps, and a titanium sublimation pump. The 260 ℓ/s turbomolecular drag pump on the main chamber is mounted horizontally on a large (6" OD) port to provide the maximum throughput. A 6" pneumatic gate valve is located between the turbomolecular drag pump and the main chamber to isolate the pump from the main chamber. The main chamber has a base pressure of less than 2×10^{-10} Torr and is monitored by a residual gas analyzer (RGA) and a standard Bayard-Alpert ion gauge. An additional 100 ℓ/s sputter ion pump is connected to the external apparatus housing, which contains an electrostatic energy analyzer (EEA).

The vacuum in the differential line for the argon ion gun is maintained by an additional 260 ℓ/s turbomolecular drag pump and monitored with a standard, Bayard-Alpert ion gauge. The differential line also is connected to the chamber to provide additional pumping on the main chamber during bakeouts. Pneumatic valves (2¾") on the differential line are located at the chamber port and the argon gun to isolate the differential line and its turbomolecular drag pump. The pressure in the differential line is typically $< 3 \times 10^{-9}$ Torr when the argon gun is not operating.

The gas handling system has two separate gas reservoirs: one to provide argon gas for the argon ion/fast atom gun and one to hold other gases which can be introduced into the main chamber via a variable precision leak valve, capable of leak rates of
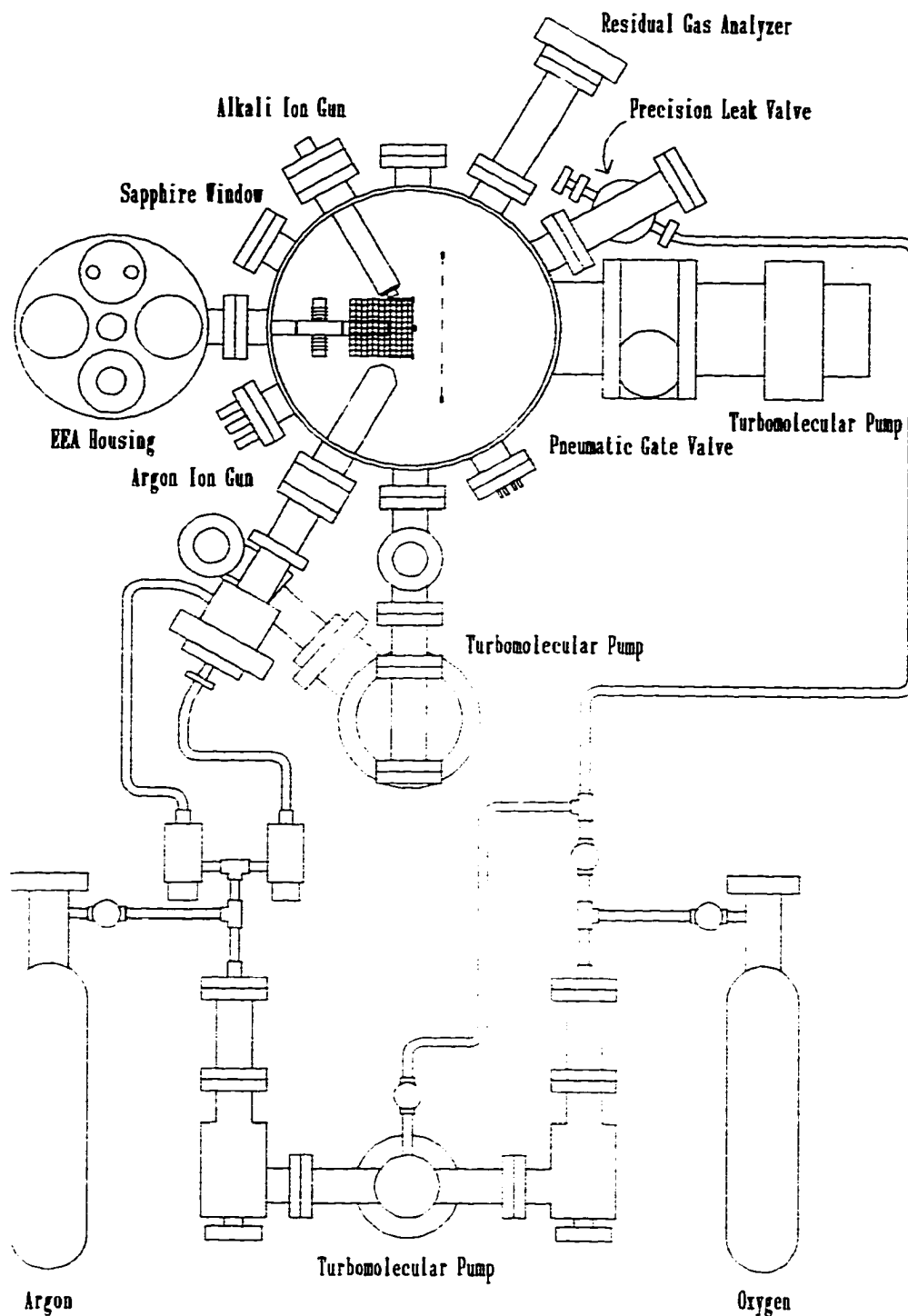
Fig. 2.1 Schematic of the surface analysis apparatus including the gas handling system. The six sputter-ion pumps (including the one on the EEA housing) and the titanium sublimation pump are not illustrated.

10^{-11} Torr ℓ/s. Two leak valves on the argon reservoir enable argon gas to be introduced to the ionization cell and the charge transfer cell in the argon gun independently. The vacuum in the gas handling system is maintained with a 60 ℓ/s turbomolecular drag pump and is monitored with a standard, Bayard-Alpert ion gauge. The gas handling system has a base pressure of $< 5 \times 10^{-9}$ Torr. There is an additional valve on the gas handling system to allow for the evacuation of the line between the reservoir and the variable leak valve. All of the aforementioned turbomolecular drag pumps are backed by Sargent-Welch, DirecTorr rotary vane pumps.

An electronic control panel houses controls for all of the pneumatic valves and two Fenwall temperature controllers which power heating tapes during the bake-out procedure. Power failure reset circuits were built to interlock the turbomolecular-fore pump systems to prevent accidental restarts following power interruptions. An additional reset circuit protects all of the pneumatic valves in order to prevent accidental venting of the chamber or exposure of an operating turbomolecular pump to atmosphere following a power failure. All of the safety circuits must be reset manually following the loss of power, not an infrequent event in Williamsburg. In order to obtain UHV, the entire system, including the gas handling system, is heated to temperature of 100 °C for approximately 24 - 48 hours following evacuation of the system to remove adsorbed water from the chamber walls. Internally, a halogen lamp is used to heat the surface mounting assembly and the extraction lens stack, and an additional lamp is used to heat the EEA inside its magnetic shielding. The two temperature controllers control the heating of the chamber by monitoring the temperature of the chamber via thermocouples attached to the

top and bottom halves of the chamber to provide uniform heating. During each heating cycle, the filaments of the titanium sublimation pumps are out-gassed, and following the process, the argon gun filaments also are out-gassed.

In the UHV chamber, the alkali ion gun is aligned at an angle of 60° with respect to the surface normal. The alkali ion gun consists of an ion source, an einzel lens and a quadrupole lens, all contained within a ground shield, and a final lens at the gun's tip. Positive sodium ions (Na^+) are produced from a thermal emission cation source, and its operation does not alter the pressure in the vacuum chamber. The ion source is made of a porous tungsten surface impregnated by an alkali metal compound which emits Na^+ ions when heated. The purity of the emitted ions is reported to be greater than 99%, and no metastable ions should be emitted [52]. The ions are extracted from the source and focussed on the surface by applying the appropriate voltages to the lens elements. Opposite the Na^+ gun is a Fisons 0.1 - 5.0 keV argon ion/fast atom gun which has been used to provide an Ar^+ beam incident on the surface at an angle of 60° with respect to the surface normal. The Ar^+ beam, used for cleaning the surface, is fully rasterable over the entire surface area of the sample.

The experimental arrangement, inside the UHV chamber, is shown schematically in Fig. 2.2. The surface mounting assembly aligns the sample vertically, perpendicular to the plane formed by the Na^+ and the Ar^+ beams, and consists of two mounting arms, a cylindrical grid and a back plate. In the studies of polycrystalline metals, the samples were thin ribbons which were held by the mounting arms directly. Leads attached to each arm permitted the sample to be heated directly by passing current through the sample. Current
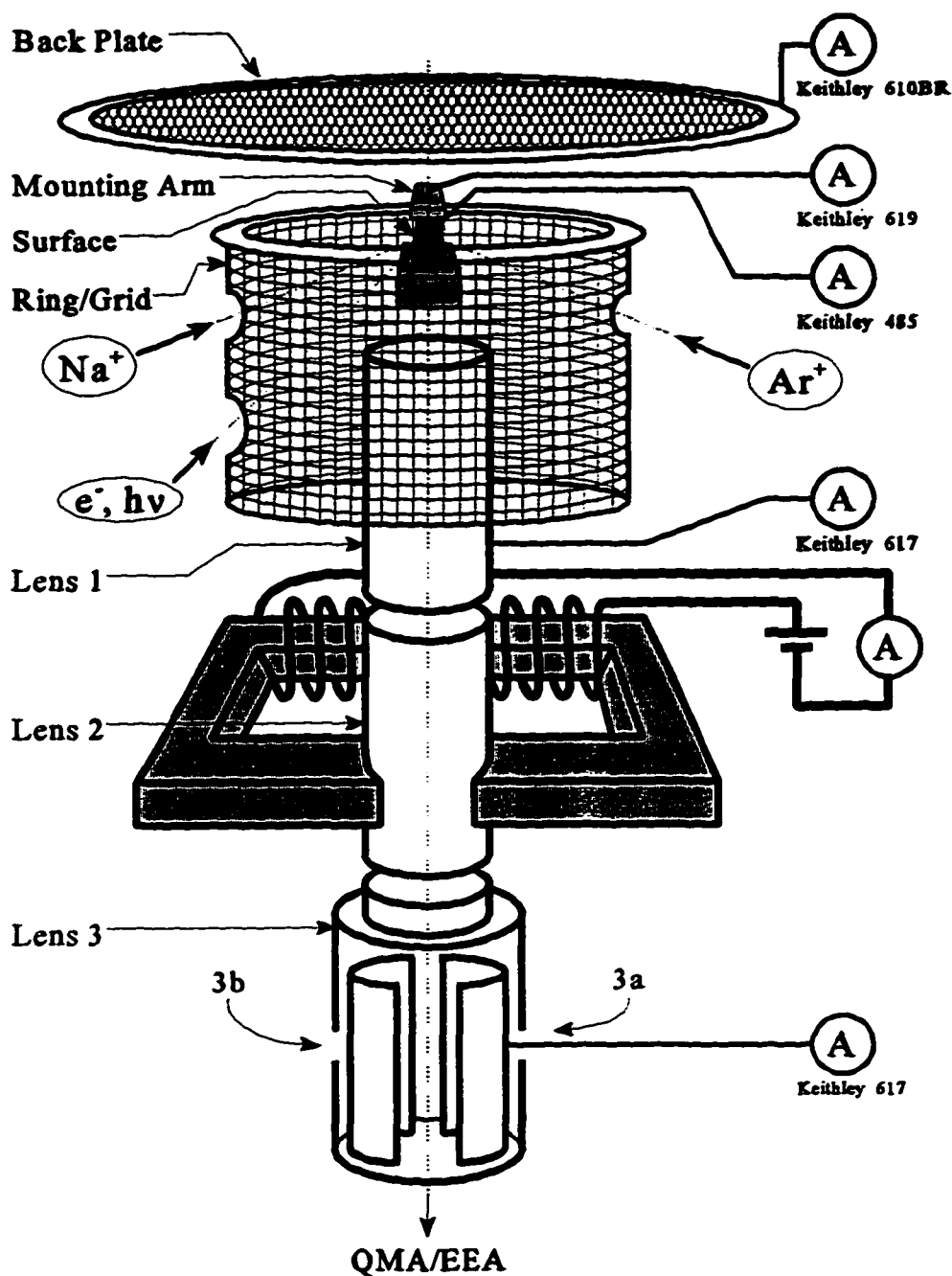
Fig. 2.2 Arrangement of the apparatus inside the UHV chamber (not to scale). The elements of the surface mounting assembly and the extraction lens stack, and where applicable, the electrometers monitoring those elements are identified. The two halves of the split lens (lenses 3a and 3b) are electrically isolated and lie inside lens 3.

at the surface, consisting of arriving Na^+ ions and departing negative ions and electrons, was measured with a Keithley 485 picoammeter. In the investigations of single-crystal surfaces, the crystal was held by an aluminum crystal mount, attached to the mounting arms, which is isolated from the crystal itself. This allowed for the current on the crystal mount to be monitored independently (by a Keithley 619 electrometer) of that on the single crystal sample (measured with the Keithley 485) to assist in the focussing of low energy ion beams. The crystal can be heated by electron bombardment from a tungsten filament located between the crystal mount and the back plate. The back plate is actually a screen of 93% transparent tungsten mesh, attached to a circular (150 mm in diameter) ring mounted vertically, lying 25 mm behind the surface. This assists in focussing the negative ions and electrons ejected from the surface into the extraction lens system, and the positive ion current reaching the back plate is measured with an electrometer. The cylindrical grid is mounted on a 64 mm diameter ring in the plane of the surface, forcing azimuthal symmetry about the horizontal extraction axis in the region in front of the surface. The grid extends from the plane of the surface to 25 mm beyond the entrance of the first lens in the extraction stack and has small apertures for admitting the Na^+ beam, the Ar^+ beam and for either light or an electron gun to be focussed on the sample at an angle of 30° with respect to the surface normal.

The extraction lens stack consists of six electrostatic lens elements which collect and focus the negative ions and electrons emitted from the surface. The collection lens (lens 1), typically biased at + 70 V, collects about 75% of the negatively charged products, and the remaining portion passes down the extraction stack and is collected at the split

lens. The negative current at these lenses is measured with two Keithley 617

electrometers. It is assumed that the sampled portion provides an accurate measure of the

electron-ion fraction for all of the negative products collected. This assumption is

supported by the observation that the electron-ion fraction is constant over a wide range

of extraction focal conditions. A small iron-core electromagnet is attached to lens 2

which, when operating, produces an 80 Gauss transverse magnetic field which deflects the

electrons from the extracted negative products without appreciably affecting the negative

ion trajectories. The third extraction lens (lens 3) houses a split lens assembly which

consists of two half cylinders isolated from each other and from lens 3. The split lens has

two modes of operation: to determine the ratio of negative ions to electrons for the

sampled portion in order to calculate their absolute yields, and to direct the negative ions

into the quadrupole mass analyzer (QMA) or the electrostatic energy analyzer (EEA). In

the former mode, the collection side of the split lens (lens 3a) is typically biased at +100 V

with respect to the other half (lens 3b) to collect the negative ions and electrons.

Otherwise, the two split lenses are essentially at a common potential and are tuned to

direct the ions into the entrance aperture of the QMA or EEA. In either case, they are

ultimately detected by a channel electron multiplier (CEM).

The design of the experimental arrangement for the focussing and collection of the

negative ions and electrons was aided through the use of SIMION [53], a numerical code

which calculates the trajectories of charged particles in the presence of electrodes. It was

used to simulate the trajectories of both the Na^+ beam and the secondary electrons and

negative ions emitted from the surface. The simulation provided estimates of the ideal

position, size and focussing potential of each element of the surface mounting assembly and extraction lens stack to properly focus the negative products. These simulations were necessary to ensure absolute collection efficiency for wide ranges of ejection angles and kinetic energies of the sputtered ions and secondary electrons. Typical focussing potentials and simulated trajectories generated with the SIMION code for the experimental arrangement are shown in Fig. 2.3.

The iron-core electromagnet was particularly sensitive in its operation due to its hysteresis. Special care was taken to set the magnetic field to zero during the magnet's on-off cycle. Prior to a set of measurements, the magnet had to be tuned by setting the control current (typically 250 mA) in order to collect all of the electrons from the sampled portion at the split lens. This was the "zero-point," and the control current was noted and incorporated into the computer programs which employed the electromagnet to make the yield measurements. The field was turned on and off by slowly ramping the control current up and down. In order to get back to the zero-point, the control current had to be slightly back-biased for a moment, and then it was set to the zero-point.

The QMA used in the experiments on polycrystalline Al was an existing, home-built, 10" quadrupole and its associated electronics. The QMA was driven by a controller which operated on one of four, manually-selected frequencies, generating four, over-lapping ranges of mass filtering. In practice, three frequencies were used to obtain a full mass spectrum. The 3.046 MHz, 1.077 MHz and the 622 kHz channels corresponded to mass ranges of 0.25 - 3.0 amu, 2.5 - 55 amu and 5.0 - 85 amu, respectively. The mass resolution, $\Delta m/m$, could be manually selected by adjusting the ratio of DC to RF voltages
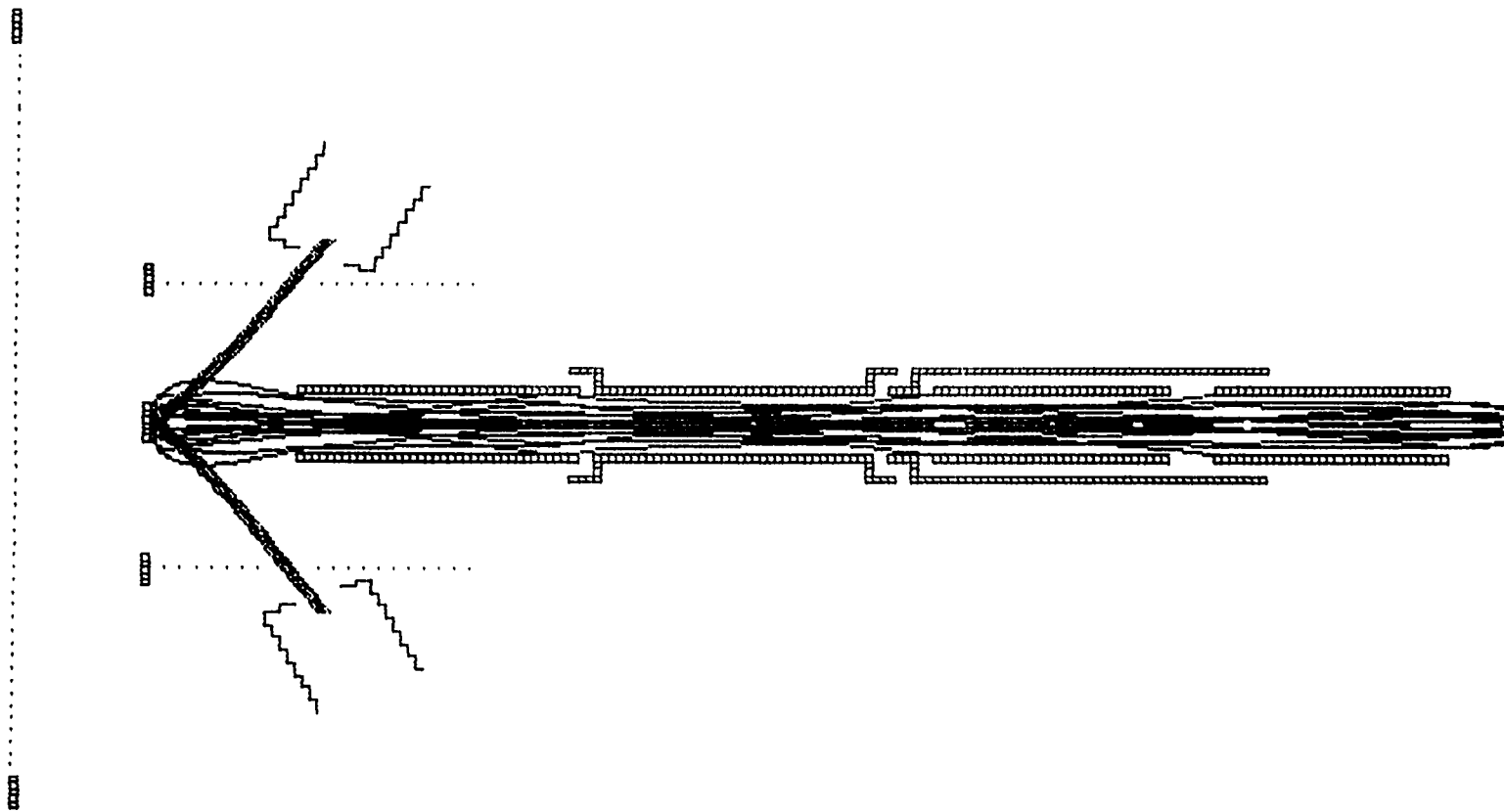
Fig. 2.3 SIMION ion trajectory simulation for the experimental apparatus. The potentials for each element are as follows: Back Plate, -19.7 V; Surface, -20.0 V; Ring/Grid, -43.8 V; Lens 1, +70.0 V; Lens 2, +272.2 V; Lens 3, +116.8 V; Split Lens (both halves), +90.0 V; Lens 4, +45.4 V. The trajectories for negative ions sputtered from the surface are simulated for negative ion initial kinetic energies of 0.5 - 5.0 eV and for angles up to 60° from the surface normal. In this simulation, the target is the Mo (100) crystal, and thus, sputtering from the entire face of the surface was simulated by varying the initial ejection point across the 9 mm diameter of the crystal. The Na⁺ and Ar⁺ ion beams incident on the surface are also shown.

19

on the quadrupole rods and was typically run at a resolution of 0.025. An analog voltage, linearly proportional to the amplitude of the rf voltage applied to the quadrupole rods (and hence, mass), was generated by the controller, measured with a Fluke 45 multimeter and coupled to the computer, via IEEE - 488 protocol, to create a mass spectrum. In order to calibrate the QMA, CCl_4 was placed on the surface such that the two chlorine isotopes $^{35}Cl^-$ and $^{37}Cl^-$, C^- and C_2^- could be sputtered from the surface in addition to the other negative ions typically observed. These peaks then were used to calibrate the two, high-mass ranges for four different mass resolutions. The 1.077 MHz channel provided the best combination of range and resolution to observe the principal negative ions, O^- and AlO^-. The 3.046 MHz and 622 kHz frequencies were used only to resolve the lowest (H^-) and highest (AlO_2^-) mass negative ions sputtered from the surface.

The EEA consists of two concentric spherical sector surfaces and has an average radius of curvature of 36.5 mm. The energy resolution of the spherical energy analyzer was determined by measuring the kinetic energies of secondary electrons ejected by a 1.0 keV Ar^+ beam at several transmission energies, E_{TRANS}. The slope of a linear fit to the full width half maxima of the distributions gives the resolution, $\Delta E/E_{TRANS}$, which was determined to be 0.0077. There is no discrimination against low kinetic energy ions and electrons in this experiment as the negative products are ejected into a region where the electrostatic field is ~ 100 V/cm. Hence, the measured spectra do not require adjustment as the transmission and detection efficiencies are independent of energy for the small range of ejection energies observed.

Time-of-flight (TOF) investigations of the sputtered negative ions can be

performed by pulsing the Na^+ primary beam. The pulsed beam was generated by pulsing the voltage on the third lens in the alkali gun with a Directed Energy Instruments (DEI) pulser. The DEI pulser is essentially a fast, high voltage switch which, when coupled with an external pulse generator, generates voltage pulses from two input voltages (V_{HIGH} and V_{LOW}). First, the potential on the third lens was set to completely block the ion beam (V_{HIGH} set to 20 V above the source potential). Then a negative voltage pulse (V_{LOW} set to the focal condition) was applied to the third lens, allowing the ion beam to pass. The typical pulse conditions were 50 - 100 V (negative) pulses with widths of 0.25 - 0.50 μs at ~ 2 kHz repetition rate. A Stanford Research Systems SR430 Multi-Channel Scaler, triggered by the pulse, collected the resulting secondary negative product signals from the CEM, generating a TOF spectrum. The principal use of the TOF technique was mass spectroscopy, replacing the QMA.

An additional feature of the TOF measurements is that, by varying the potential of the surface slightly, it is easy to confirm that the sputtered negative ions come exclusively from the surface being studied and not from any other element in the system. In a similar manner, a slight change in the surface potential produces a shift in the kinetic energy distributions measured with the EEA. The shift in the energy scale is exactly equal to the change in the surface potential, and thus, provided another verification that the products being analyzed originate at the surface of the sample. Additional tests, at impact energies below the observed energetic thresholds for sputtering, show that no negative secondaries are collected by the collection lenses even though elements near the surface (e.g., the grid) lie at potentials below that of the surface. Furthermore, each element of the extraction

system, in addition to the collection elements, was monitored independently to ensure that the current collected on those elements was negligible.

In order to investigate the effect of oxygen and sodium on the work function and its relationship to secondary emission from the polycrystalline Al surface, the surface was exposed to UV light and the photoelectron emission was monitored. Differences in the thresholds for photoelectron emission correspond directly to changes in the Al surface's work function. A Hamamatsu xenon flash lamp produced the UV light which was filtered through band-pass filters (10 nm width) and focussed on the surface through a sapphire window. The flash lamp was inherently noisy, necessitating time-averaged measurements of the photoelectron emission. In these experiments, the surface was exposed to a known amount of oxygen, and a 250 eV Na^+ beam was focussed on the surface. As the surface accumulated sodium, the beam was stopped momentarily, the flash lamp was triggered, and the emission was measured with the extraction system. First, the 300 nm filter was used to identify the 4.1 eV emission threshold, and then the 350 nm filter was inserted to find the 3.5 eV threshold. Due to the spectral response of the lamp's synthetic-silica housing, the intensity of the lamp was greater at 300 nm than at 350 nm by a factor of 1.71, and thus, the intensity of photoelectrons had to be appropriately scaled before linearly fitting the results. The linear fits, extrapolated to zero, define the threshold for photoelectron emission as a function of Na^+ dose, and the difference between the two thresholds corresponds directly to a change in the work function. The oxygen-induced change in the work function was determined by a comparison of the threshold difference for different exposures to Na results.

Oxygen-induced changes in the work function for molybdenum surfaces are well known, and photoelectron emission experiments were unneeded. Thus, upon the completion of the experiments on Al, the flash lamp and sapphire window were replaced with an electron gun in order to perform Auger Electron Spectroscopy (AES). The intention of using AES was not to provide quantitative surface analysis in the strict sense, but rather, to furnish a method by which qualitative surface analysis could be performed without changing the surface conditions appreciably. A 3 keV electron gun was mated with an R.M. Jordan electron gun power supply to control the emission current and an x-y steering unit to focus the beam. The same extraction system used to analyze the low energy, ion-induced secondary electron and anion kinetic energies was used to measure the kinetic energies of the Auger electron peaks in the total secondary electron distribution. The detection efficiency was high enough that the AES experiments did not have to be operated in a differential mode, and analysis was performed upon the raw spectra.

The data analysis system was operated by a computer with a National Instruments GPIB controller card, and programs were developed using Lab Windows to interface with all of the measurement, detection and control devices. Data from the electrometers, the multi-channel scaler, a Fluke 45 multimeter (for the QMA and the EEA), an Aston GPIB Scaler (used to count pulses from the CEM) and the RGA were collected, displayed in "real-time" and saved to files for further analysis. Kepco SN-488 digital programmers were used to drive other devices such as: two Kepco APH-500M power supplies, which set the potential of the EEA, a Kepco ATE6-25M power supply which drives the

electromagnet attached to the second extraction lens, the QMA and the Hamamatsu flash lamp.

2.2 Surface Preparation

The principal aim of this work is to develop an understanding of the enhancement of the secondary electron and negative ion yields due to the oxygen coverage of the surface. The principal uncertainty in these experiments is associated with the exposure of the surface to a known flux of oxygen. This requires knowledge of the oxygen partial pressure, measured with an Ametek Quadrupole Residual Gas Analyzer (RGA), which is known only to an accuracy of $\pm$ 15%. The RGA was typically operated in a pressure vs. time mode such that the oxygen partial pressure profile was recorded by the RGA during the exposure and then read by the computer.

The presence of significant amounts of adsorbed alkali-metal has been shown to lower the surface's work function and dramatically increase the negative ion yields from metal surfaces under ion bombardment. For large primary beam exposures to the surface, a significant amount of Na will adhere to the surface. This substantially alters the total yield (increasing both Y_x^- and Y_e^-), undoubtedly due to the lowering of the work function associated with alkali-metal coverage of the surface. Thus, care was taken to limit the total Na dose (< 20 nA min) of the surface during all measurements in order to make the effects of adsorbed Na on the results negligible. During a yield measurement, the operation of the electromagnet required that the Na$^-$ beam be incident upon the surface for ~ 30 s, and thus the total Na dose of the surface was restricted by lowering the Na$^+$

current with increasing oxygen exposure of the surface or impact energy. Decreasing the primary beam current did not affect the yields at a given oxygen coverage or impact energy, thus ensuring that secondary emission follows from a direct, first order process independent of the magnitude of the current striking the surface. Specifically, for polycrystalline Al, the maximum increase in Y_x^- due to the adsorbed Na is < 5%, and the effect on the secondary electron yield is < 0.25%. The yield results to be presented have not been adjusted to compensate for these relatively small effects. In order to measure the kinetic energy spectrum of the sputtered anions and secondary electrons, the Na^- beam was required to be incident upon the surface for ~ 90 s. These kinetic energy spectra were corrected for the slight change in the contact potential between the surface and the detector due to the lowering of the surface work function associated with the Na dosage. The effects of adsorbed Na on Y_x^- and Y_e^- will be described in detail later in this work.

2.2.1 Polycrystalline Metals

The samples used in the experiments on polycrystalline metals were 50 x 3 mm ribbons of high purity aluminum (99.995%, 0.038 mm thick) [52] and molybdenum (99.95%, 0.025 mm thick) [53]. Prior to each set of measurements, the surfaces were sputtered clean by a semi-automatic rastering of a 4.0 keV Ar^+ beam over the entire surface area for three hours at a beam current of > 1.0 μA. While the Mo ribbon could be heated directly, the Al ribbon was unable to be heated directly due to its relatively low melting point (~ 660°C) and the lack of a direct temperature measurement. Following the initial sputtering, the Mo ribbon was heated for 10 min. by passing current through the

sample, and then it was sputter cleaned again. For both surfaces, the surface cleanliness was ascertained by secondary ion mass spectroscopy (SIMS), and the oxygen coverage is determined by measuring the oxygen ion yield at an impact energy of 250 eV. Specifically, it was required that $Y_O^-(250 \text{ eV}) \leq 0.1\%$, and increasing the sputter cleaning time beyond three hours did not significantly lower $Y_O^-(250 \text{ eV})$. Auger Electron Spectroscopy (AES) was not available at the time of the polycrystalline experiments to check the surface cleanliness, hence this inequality provided our operational definition of clean.

2.2.2 Single Crystal Metals

The Mo (100) single crystal was a polished disk (9 mm in diameter, 2 mm thick, polished to an orientation of < 0.5° [56]) which was mounted on the head of a stainless steel screw. Care was taken during the process of spot-welding the screw to the rear of the single crystal not to mar the polished surface (e.g., the grounding electrode was attached to the side of the crystal). The surface of this sample was cleaned by cycling Ar⁻ ion sputtering and electron-bombardment heating in the following manner: rastering a 3.5 keV Ar⁺ ion beam over the entire surface area at a current density of ~ 0.6 μA cm⁻² for 1 hour, heating the sample by electron-bombardment (~ 7 W for 30 min.) and finally, sputter cleaning again for 20 minutes. A VG Microtech Physical Imaging Unit was used to raster the beam and image the surface on an x-y-z oscilloscope with the Ar⁺ current collected on the surface serving as the brightness (z axis). In order to generate the brightness level, the Ar⁺ surface current was amplified first with a Stanford Research Systems SR570, low

noise, current pre-amplifier, whose output was amplified again with an EG&G Ortec 572

amplifier. In this manner, we ensured that the whole surface area was sputter-cleaned.

Following the cleaning procedure, an AES spectrum (3 keV electron beam) was obtained

to confirm that all of the adsorbed oxygen was removed from the surface.

CHAPTER 3

ALUMINUM

Figure 3.1 clearly illustrates the rather dramatic effect that oxygen coverage can have on the secondary electron yields. In addition to the present measurements for clean and oxygenated Al surfaces, Fig. 3.1 shows the low impact energy portion of the secondary electron yield of a similar experiment of Na^+ impacting a clean Au surface [2]. There is virtually no direct kinetic electron emission from these clean surfaces at low impact energies for ions such as Na^+ with low ionization potentials. In fact, for clean Au, $Y_e^- < 0.1\%$ for impact energies below 350 eV, and similarly, Y_e^- for clean Al is small, increasing to only ~ 0.5% at an impact energy of 450 eV. However, the presence of less than a monolayer of adsorbed oxygen on the Al surface leads to a large increase in secondary electron emission. Remarkably, the increase in the electron yield, shown in Fig. 3.1, is greater than two orders of magnitude at an intermediate energy of 250 eV. The enhancement of the emission of electrons after an exposure of the Al surface to oxygen is illustrated clearly for the full range of impact energies and can be attributed directly to the adsorbed oxygen.

3.1 Oxygen Adsorption on Aluminum

The amount of adsorbed oxygen on the surface is related its exposure to oxygen, and it is generally accepted that an exposure of 100 L (1 L = 1 Langmuir = 10^{-6} Torr s) to polycrystalline Al corresponds to a surface coverage, Θ_S, of $0.75 < \Theta_S < 1.0$ monolayer
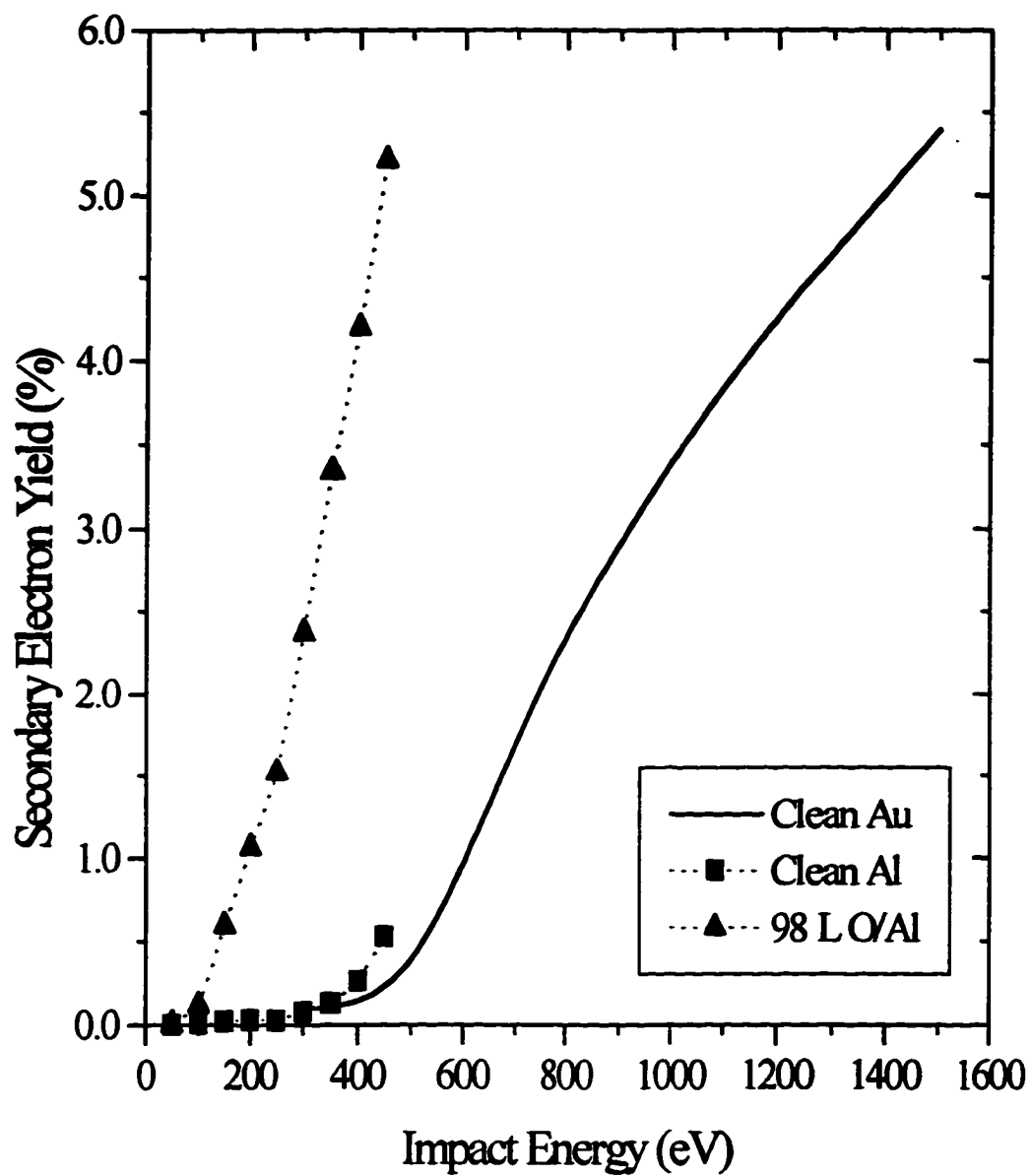
Fig. 3.1 Absolute secondary electron yields for Na^+ impacting Al: (■) clean and after a (▲) 98 L oxygen exposure. Low impact energy (——) results for Na^+ impacting clean Au and from Ref. [2].

(ML) of oxygen atoms with the formation of a complete monolayer occurring at ~ 300 L [50,57-59]. Very similar results are found for single crystal Al upon exposure to oxygen [60,61]. For illustrative purposes, the rate at which the surface becomes covered with gas molecules can be estimated with elementary kinetic theory and the ideal gas law. The flux of gas molecules at a density, n, and an average velocity, $\bar{v}$, which strike the surface can be expressed as,

$$\Phi = \frac{n\bar{v}}{4} = \frac{P}{(2\pi mkT)^{1/2}},\qquad(3.1)$$

where P is the pressure, T is the temperature and m is the mass of the gas molecules. Assuming every O_2 molecule sticks to the surface and dissociates, and a density of surface atoms on the order of ~ 10^{15} atoms/cm^2, the exposure required for one full monlayer would be,

$$\frac{10^{15}}{cm^2\, ML} \bullet \frac{(2\pi mkT)^{1/2}\, Torr\, cm^2\, s}{2P} \bullet \frac{1\, L}{10^{-6}\, Torr} = 1.4\, \frac{Langmuir}{monolayer}.\qquad(3.2)$$

Hence, the sticking coefficient for oxygen on Al is ~ 1%. In the experiments with polycrystalline Al, there was no direct method for measuring the oxygen coverage, Θ_s, other than when there was none. Thus, the results presented here will be expressed in terms of the oxygen exposure.

3.2 Aluminum Results

3.2.1 Yields

The total yield of negative products is shown in Fig. 3.2 as a function of impact energy for three different Al surfaces: a clean surface and two oxygen-exposed surfaces at 52 L and 98 L respectively, i.e., about ½ and ¾ ML coverage. Y_T^- is small for a clean surface at all impact energies, and there is a considerable increase in Y_T^- with increasing surface exposure to oxygen. A doubling of the oxygen exposure almost doubles Y_T^- at a given impact energy. The energetic threshold, E_{th}, defined by linearly extrapolating the total yield curves to zero yield, is distinct at $E_{th} \approx 50$ eV and independent of the aluminum's oxygen exposure.

SIMS spectra obtained with the QMA for overlapping mass ranges are shown in Figs. 3.3 and 3.4. Collectively, they illustrate that there are two atomic negative ions, H^- and O^-, and two molecular negative ions, AlO^- and AlO_2^-, which are sputtered from the surface over the range of oxygen coverages and impact energies studied. The two most abundant sputtered negative ions are O^- and AlO^-, and they are easily identifiable in the intermediate mass range (2.5 - 55 amu). In the low range (0.25 - 3.0 amu), a trace amount of H^- is observed, and in the high range (10 - 85 amu), sputtered AlO_2^- is observed (in addition to O^- and AlO^-). By comparing the intensity of the signals, the relative composition of the sputtered negative ions was determined. These spectra show that O^- is by far the dominant negative ion species for all coverages and energies, constituting about 94% of all the sputtered negative ions. The other negative ions contribute significantly smaller amounts: AlO^- (~ 5%), AlO_2^- (< 1%), and H^- (< 1%). Hence, the negative ion
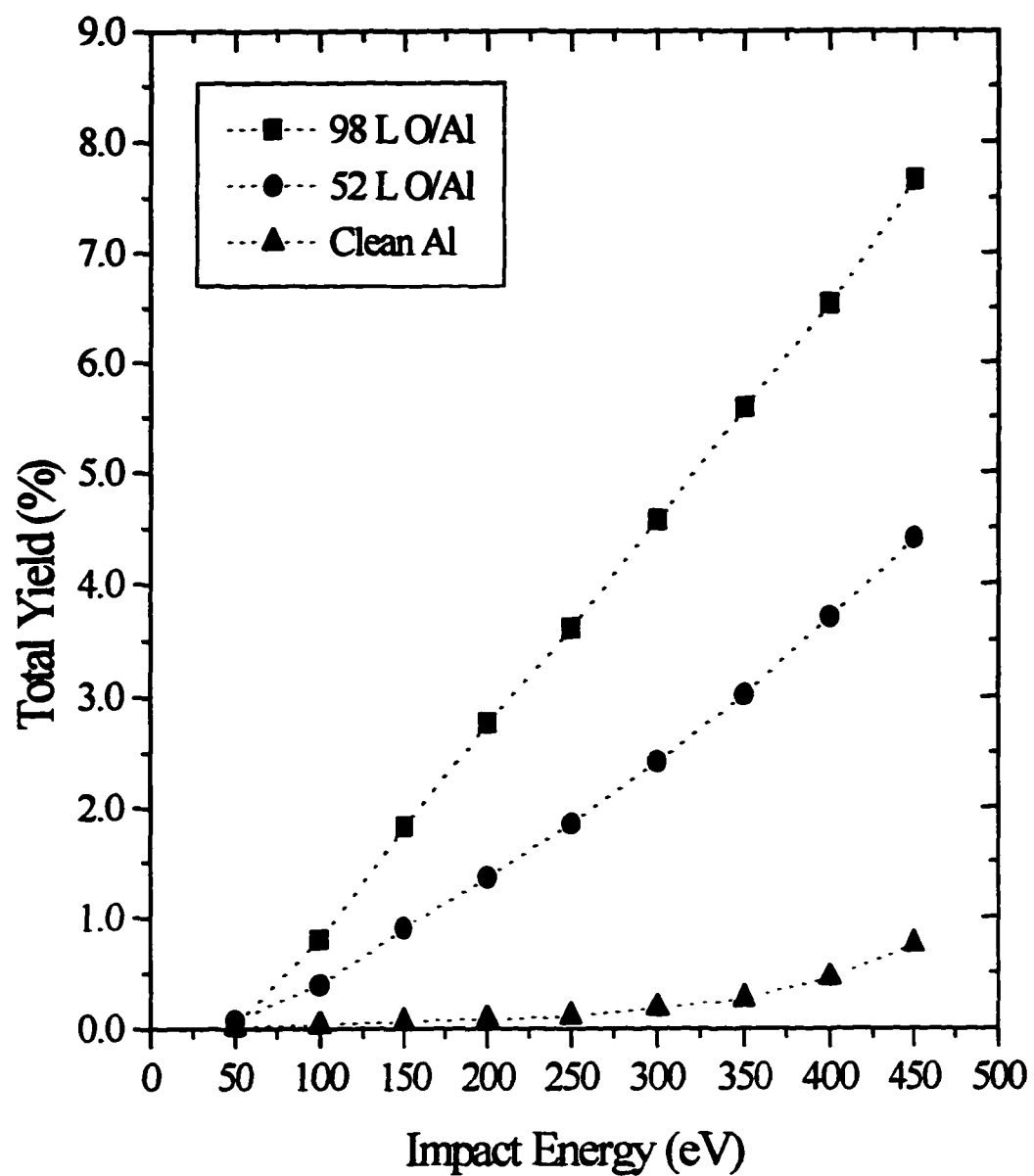
Fig. 3.2 Absolute yield for electrons and negative ions for Na$^+$ impacting Al: (▲) clean, and two oxygen exposed surfaces, (•) 52 L and (■) 98 L.
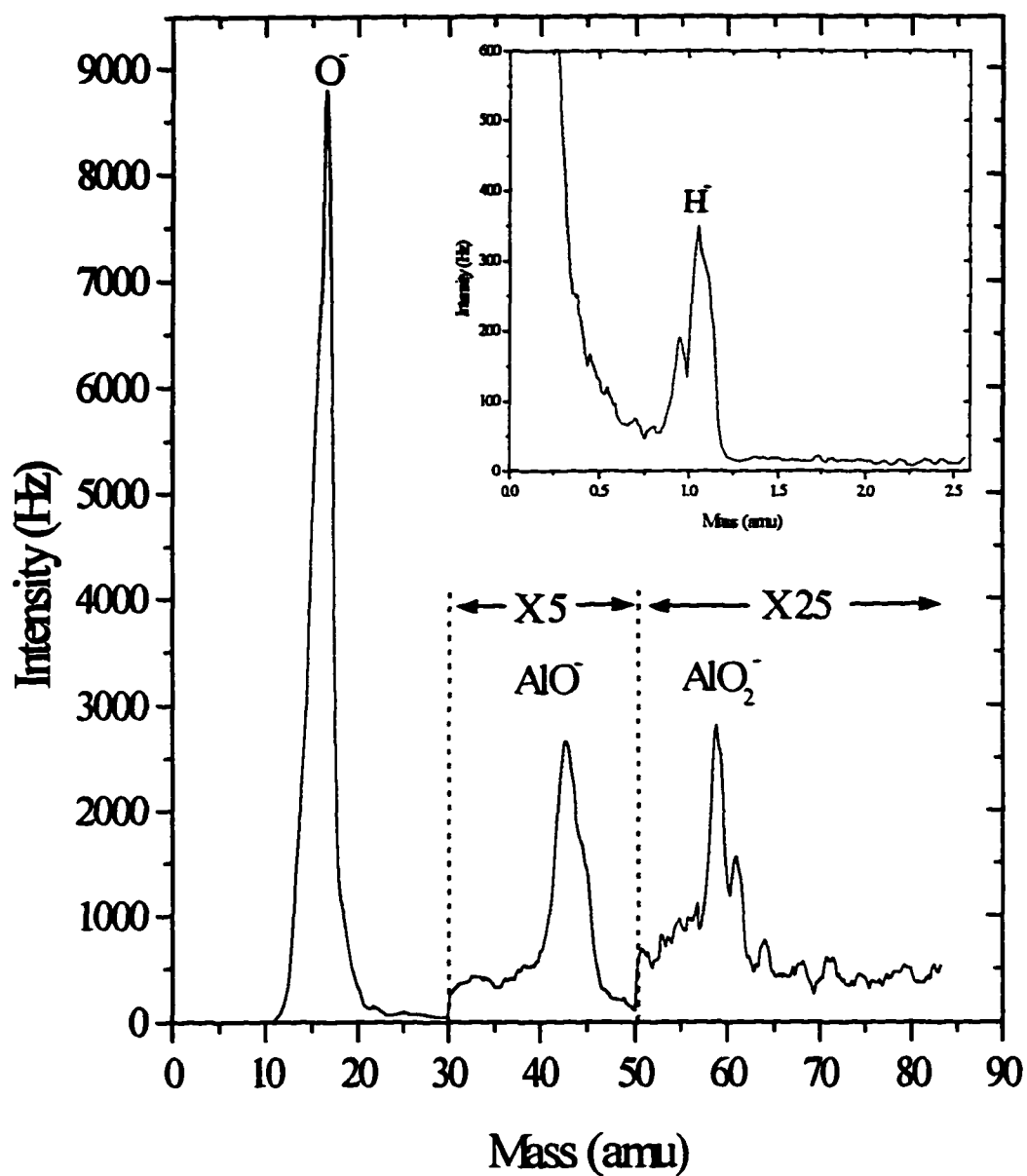
Fig. 3.3 Mass spectrum of sputtered negative ions obtained with the QMA for Na⁺ impacting an Al surface exposed to 53 L of oxygen at an impact energy of 250 eV. The AlO⁻ and AlO₂⁻ signals are enhanced by factors of 5 and 25 respectively. The inset shows the H⁻ signal for the same conditions.
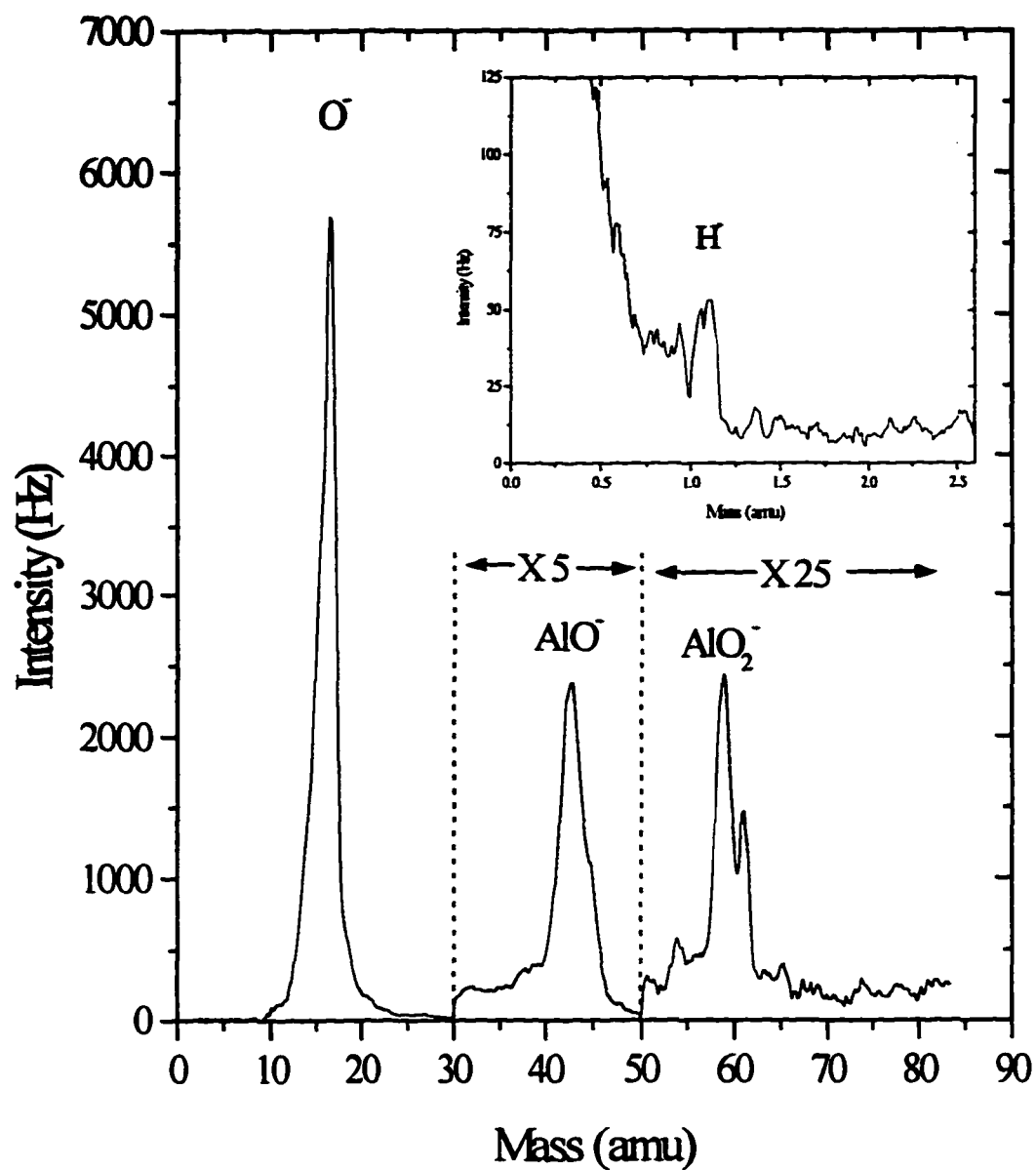
Fig. 3.4 Mass spectrum of sputtered negative ions obtained with the QMA for Na⁺ impacting an Al surface exposed to 24 L of oxygen at an impact energy of 450 eV. The AlO⁻ and AlO₂⁻ signals are enhanced by factors of 5 and 25 respectively. The inset shows the H⁻ signal for the same conditions.

yield is essentially the negative oxygen ion yield, $Y_X^- \approx Y_O^-$, and hereafter will be referred to as such.

Thus, the total yield can be separated into secondary electron and O^- yields, which are shown in Fig. 3.5 as a function of impact energy for the clean, 52 L and 98 L surfaces. The increased oxygen exposure of the Al significantly increases both Y_O^- and Y_e^-, but the threshold for both processes, which occurs for impact energies in the vicinity of 50 eV, is independent of exposure. Though the yields increase with impact energy, the dependence of Y_O^- and Y_e^- on the impact energy, E, is quite different. As Y_O^- begins to saturate around an impact energy of 250 eV, Y_e^- does not, surpassing Y_O^- at the higher impact energies (> 250 eV). The shared threshold and the increase in the yields with impact energy suggest that the yields themselves are related, and that the mechanism for secondary electron emission may be coupled with the production of negative oxygen ions at low impact energies. Finally, it is of interest to note that the impact energy at which the largest relative increase in $Y_e^-(E, \Theta_s)$ is observed at $E \approx 250$ eV for all Θ_s.

The secondary electron and O^- yields are shown in Fig. 3.6 as a function of the oxygen exposure of the Al surface for impact energies of 150 eV, 250 eV and 350 eV. Most importantly, both Y_e^- and Y_O^- are small for clean Al, and there is a large increase in the yields with oxygen exposure of the surface with both Y_e^- and Y_O^- beginning to saturate around 100 L. While Y_O^- is small at a given impact energy for clean Al, it displays a pronounced increase with increased oxygen exposure of the Al surface. The adsorbed oxygen obviously serves as the source of O^-, but it also has a major effect on secondary electron emission. Similar to Y_O^-, Y_e^- is very small for clean Al, and there is a large
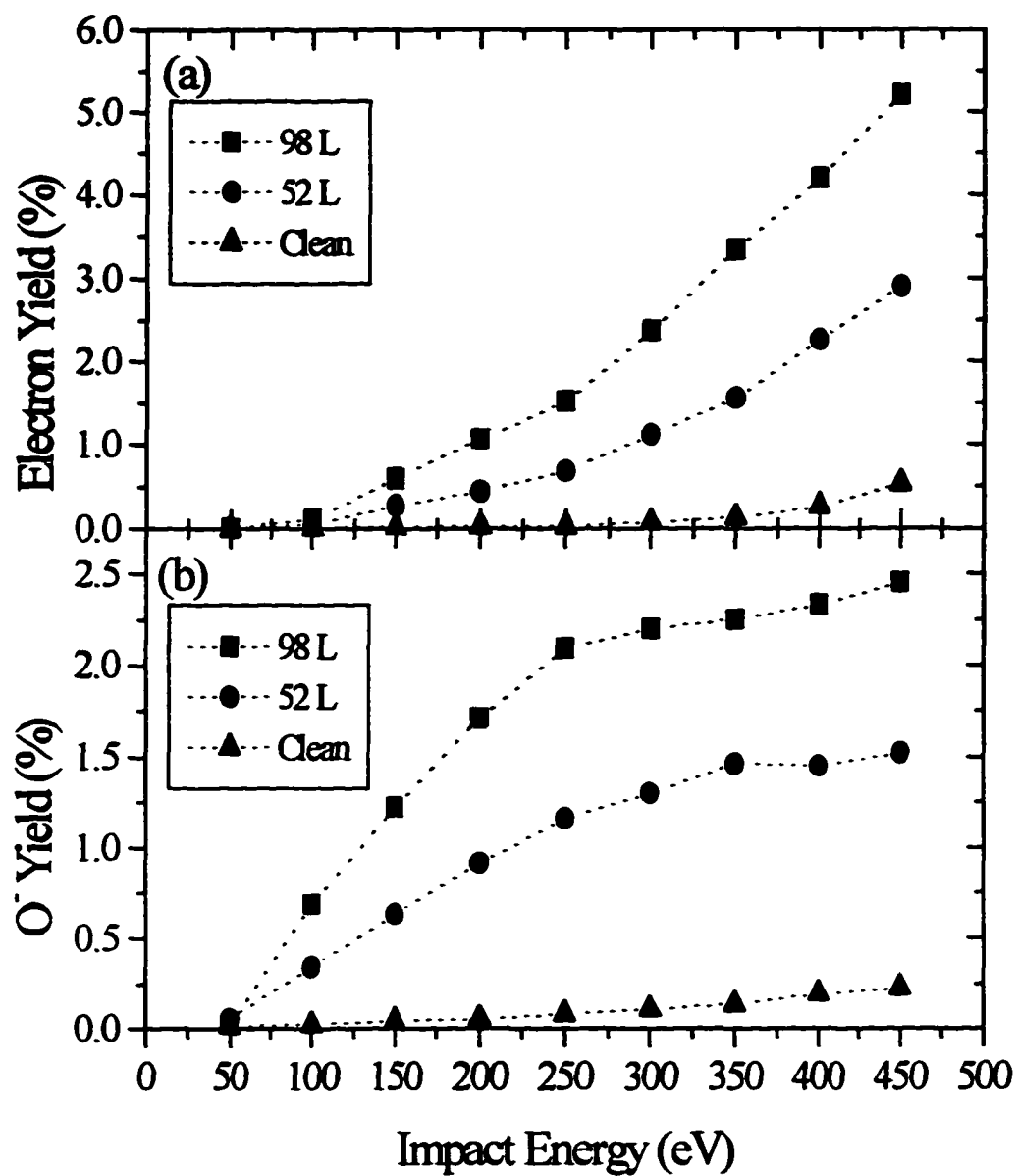
**Fig. 3.5** (a) Absolute secondary electron yields for Na$^+$ impacting Al: (▲) clean, and two oxygen exposed surfaces, (●) 52 L and (■) 98 L. (b) Absolute O$^-$ yields for the same three surfaces: (▲) clean, and two oxygen exposed surfaces, (●) 52 L and (■) 98 L.
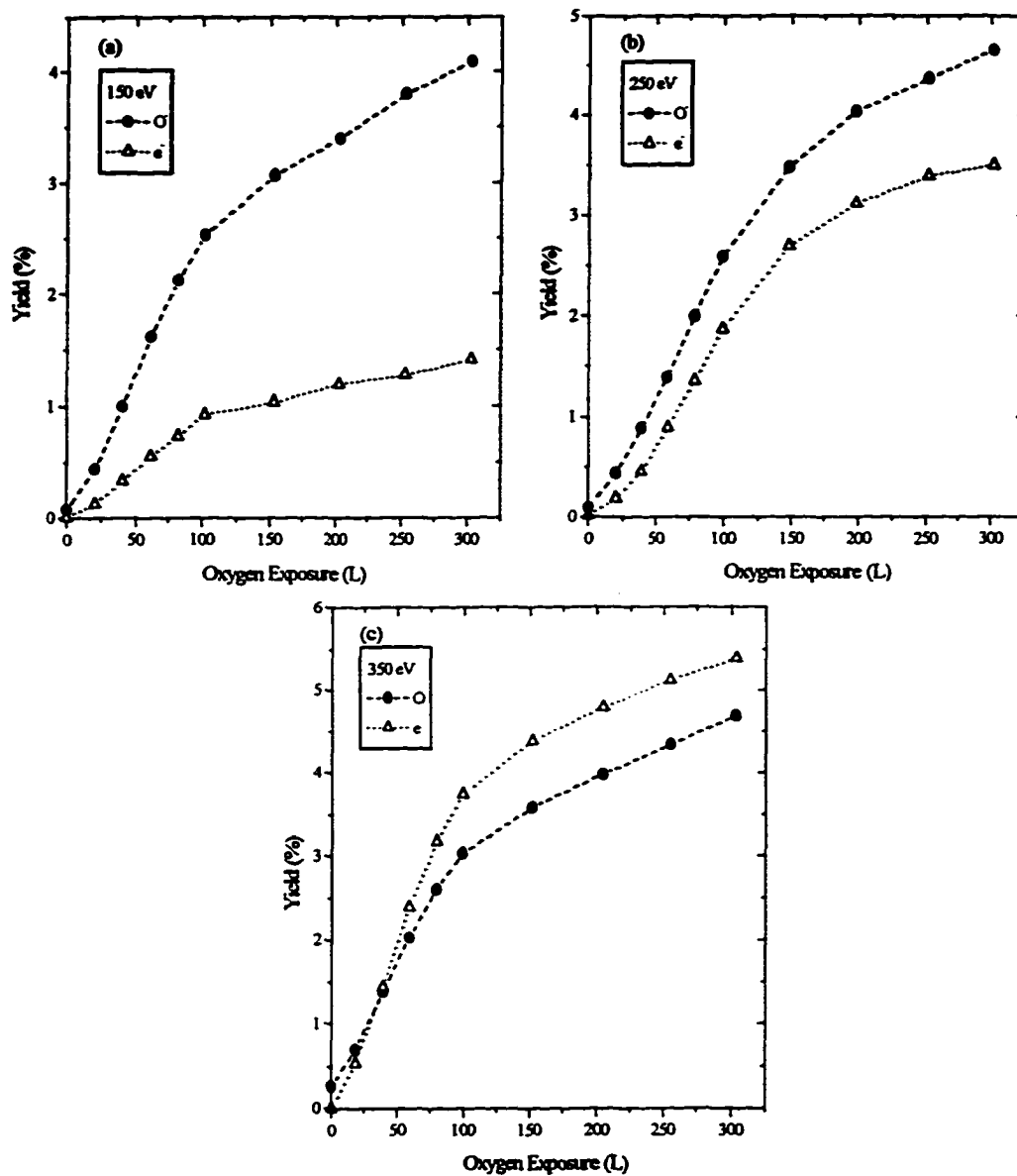
Fig. 3.6 Absolute (●) O⁻, and (△) electron yields as a function of oxygen exposure of the Al surface at fixed Na⁺ impact energies of (a) 150 eV, (b) 250 eV and (c) 350 eV.

increase in Y_e^- with increased oxygen exposure of the Al at a given impact energy.

In addition to the observed rapid increase in $Y_O^-(\Theta_S)$ and $Y_e^-(\Theta_S)$ as a function of Θ_S, there is an increase in the slopes of the yield curves for exposures up to about 50 L. For exposures ranging from 50 - 100 L, the yields exhibit a linear increase with exposure, and a change in the slopes of the yield curves is observed at an exposure of ~ 100 L, where the yields begin to approach limiting values. These three features possibly are related to recent observations of oxygen adsorption on polycrystalline Al which show a for exposures up to ~ 50 L, decrease in the work function, ϕ, of 0.2 eV and the saturation of oxygen uptake occurring at ~ 100 L [62]. Thus, from 0 - 50 L, the increasing slope of the yield curves may be related to the obvious increase in Θ_S and the corresponding decrease in ϕ. As the work function reaches a constant value at ~ 50 L, the increase of the yields becomes linear with oxygen exposure until the oxygen coverage approaches one monolayer, at an exposure of ~ 100 L, where the rate of increase in yields begins to decrease, and the yields approach their monolayer saturation values.

3.2.2 Kinetic Energy Distributions

Initially, a kinetic energy distribution was derived from TOF data for the sputtered O^- ions at an impact energy of 250 eV and an oxygen dose of about 50 L [6]. This represented an upper limit to the true width of the kinetic energy distribution because of the dispersion of the sputtered "pulse" of O^- ions. First, there was no way to accurately set the zero of the kinetic energy scale due to a lack of precise information about various delays associated with the optics of both the Na^+ ion beam and the sputtered O^- ions.

Second, broadening of the TOF distribution of the sputtered O⁻ ions owing to the fact that different sputtering angles lead to different trajectories through the extraction lens stack and the QMA, prior to detection was unknown. There was no way to account for either of these effects. Moreover, the TOF method was not suitable for measuring the kinetic energy distribution of the secondary electrons. Consequently, the electrostatic energy analyzer (EEA) was introduced in order to make accurate kinetic energy measurements of both the negative ions and secondary electrons.

The EEA was operated in a mode where the negative products pass through the analyzer at a fixed transmission energy. Figure 3.7 shows the O⁻ kinetic energy distributions at four impact energies for Na⁺ impacting an Al surface exposed to 92 L of oxygen. All the distributions peak at a kinetic energy of ~ 1 eV and all exhibit a significant high energy tail. The shapes of the distributions vary only slightly with impact energy, and also, the results for a surface exposed to smaller amounts of oxygen differ only in intensity of the sputtered ions.

Secondary electron kinetic energy distributions for the previously described surface at the same impact energies are shown in Fig. 3.8. The distributions peak between 0.8 and 1.0 eV and have full widths half maxima of 1.0 - 1.5 eV, with the widths increasing with increasing impact energy. The most probable kinetic energy is essentially independent of the impact energy, and again, the results an Al surface with other oxygen exposures differ only in the intensity of the secondary electrons. The kinetic energy measurements were extended to higher energies than those shown in Figs. 3.7 and 3.8, but no other structure in either the electron or negative ion distributions was found. The absolute energy scale of

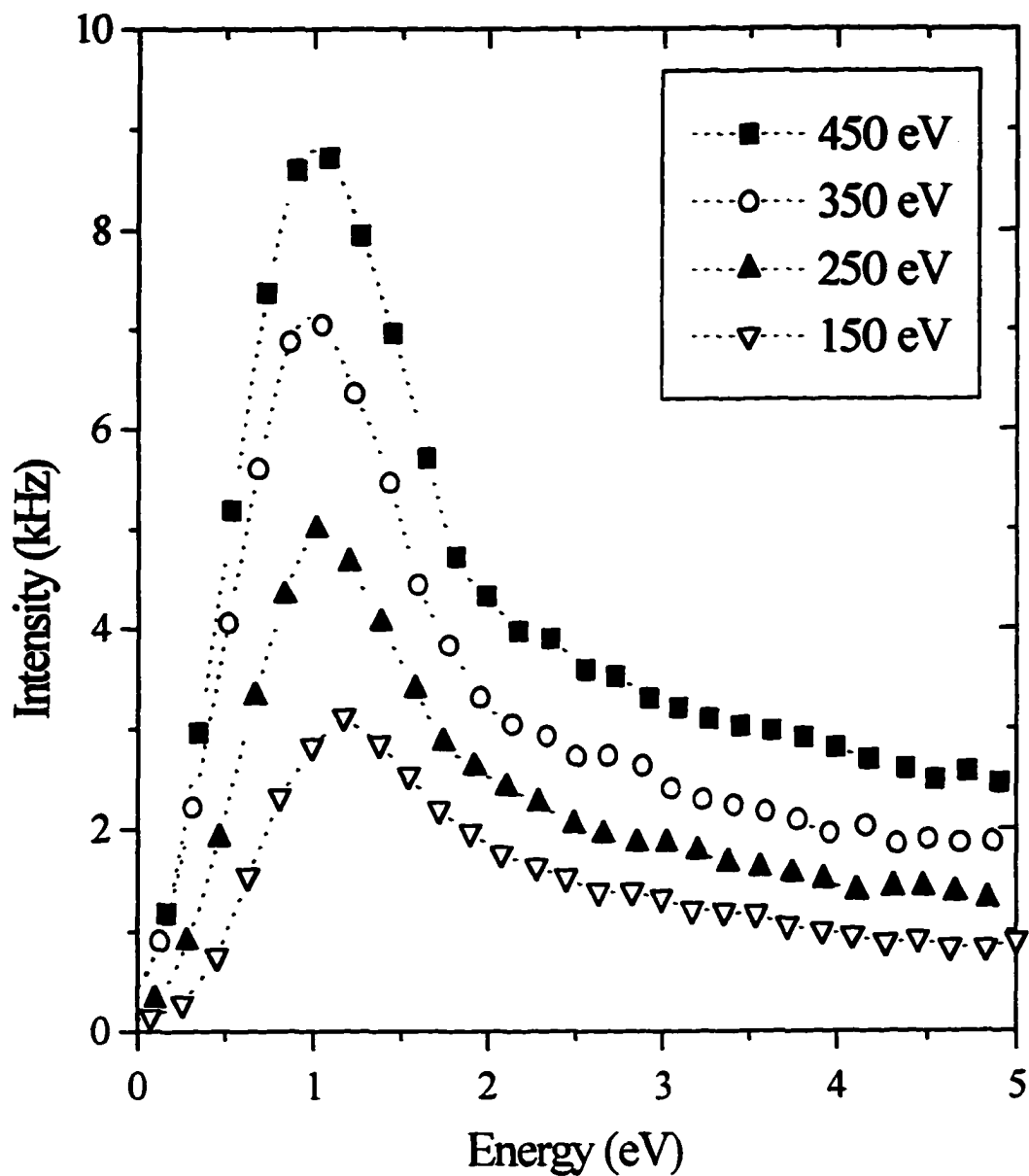**Fig. 3.7** Sputtered O⁻ kinetic energy distributions for Na⁻ impacting a 92 L oxygen exposed Al surface at impact energies of (▽) 150 eV, (▲) 250 eV, (o) 350 eV and (■) 450 eV.

Fig. 3.8 Secondary electron kinetic energy distributions for Na⁺ impacting a 92 L oxygen exposed Al surface at impact energies of (▽) 150 eV, (▲) 250 eV, (○) 350 eV and (■) 450 eV.

the results presented in Figs. 3.7 and 3.8 should be accurate to $\pm$ 0.2 eV. Similar

distributions were measured for collisions of O_2^+ with Al/O surface at impact energies of

0.3 - 2.5 keV [63].

3.3 Aluminum Discussion

To reiterate, the purpose of this investigation is to understand the origin of

secondary electrons and negative ions emitted from the surface under low-energy ion

bombardment. For emission to be significant at low impact energies, it is clear that there

must be oxygen on the surface, and the manner in which the adsorbed oxygen resides on

the surface may be important to the emission mechanism. Conventional theories would

describe electron emission as arising from either direct kinetic or potential emission,

however these two processes can be ruled out immediately as the source of secondary

electrons. A direct kinetic emission process relies simply on momentum transfer from the

incoming particle to a conduction band electron. However, due to the mass disparity

between an electron and the incoming heavy particle (Na^- ion in these experiments),

kinetic emission can only be expected to become significant for impact energies above

several keV, well beyond those studied here. In order for an electron to be ejected from a

surface into the vacuum by a potential emission process, the ionization potential of the

incoming particle must be greater the twice the surface's work function. Sodium's

ionization potential (5.1 eV) is much less the twice the work function of either Al

($\sim$ 4.2 eV) or Mo ($\sim$ 4.6 eV), and thus potential emission will not occur. Thus, another

mechanism must account for the electrons arising from ion-surface impacts. Physical

sputtering is typically described as resulting from a so-called collision cascade mechanism in which the momentum of the projectile is transferred to a number of substrate atoms. This model provides a good starting point for the discussion of negative ion emission resulting from low-energy ion-surface collisions. In what follows, it will be illustrated how the collision cascade fails to fully describe low-energy sputtering of O⁻ from an Al surface. Also, several possible sources of electron emission will be investigated. Ultimately, an electronic excitation mechanism for the emission of *both* secondary electrons and negative ions will be proposed.

3.3.1 Oxygen Interaction with an Aluminum Surface

Coupling of the electronic states of the metal with those of a negative ion results in a shift of the affinity level when the negative ion is sufficiently close to the metal's surface. Recent calculations specifically for the energy and width of the affinity level of O⁻, as a function of the distance, z, from an Al surface, have been presented by Bahrim, et al. [51]. The shift of the affinity level was found to be very similar to that predicted by a simple image charge potential. For small distances from the reflection plane, the magnitude of the affinity level, $|E_A(z)|$, canexceed the metal's work function, ϕ as shown Fig 3.9. When this occurs, the O⁻ state will lie below the fermi level, and it is then energetically favorable for an electron from the conduction band to fill the vacancy on the oxygen atom adsorbed on the Al surface. The tunneling of an electron from the metal to the oxygen atom can occur for $z < 2.5$ a_o for the Al/O system. Thus, oxygen adsorbed on aluminum resides on the surface essentially as a negative ion, O⁻.
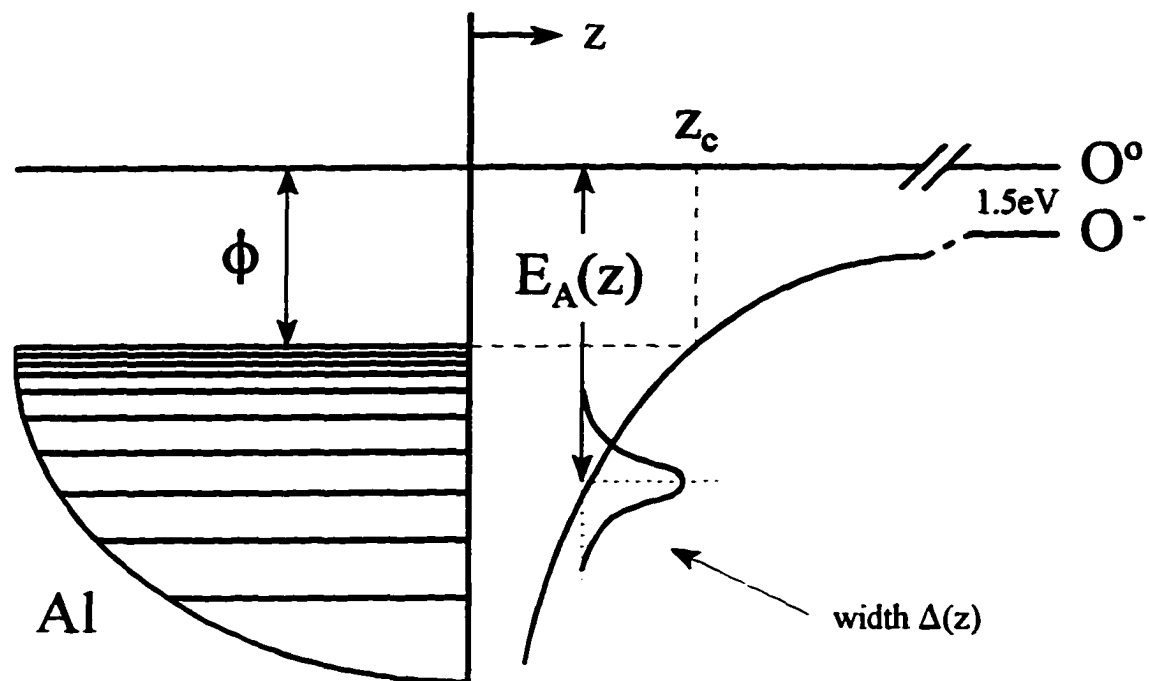
Fig. 3.9 Oxygen negative ion affinity level as a function of distance from an Al surface. The width of the level is $\Delta(z)$, and the distance where the magnitude of the affinity level is equal to the work function, ϕ, is z_c.

3.3.2 Collision Cascade

Sputtering mechanisms describing the removal of surface atoms depend upon collisions of impacting ions (or neutrals) and atoms of the substrate, and the resulting collisions of substrate atoms thereafter. The dynamics of these mechanisms have been described extensively [15,16,64,65] and may depend to some extent on the amount of oxygen on the surface. In particular, the collision cascade mechanism, which has been shown to describe sputtering for impact energies as low as a few hundred electron volts [18], also may govern the low-energy, ion-induced desorption of adsorbed oxygen from

an Al surface. For low oxygen coverages, the impacting Na^+ ion will be neutralized by an electron from the metal, and the resulting Na can then sputter an O^- by one of several distinct processes: (1) Na impacts an Al atom which then makes several collisions in the surface layer before ejecting an O^- from the surface; (2) Na itself scatters from several Al atoms and then imparts momentum to O^- ejecting it from the surface; or (3) Na impacts an O^- directly which then rebounds from the surface. For higher oxygen coverages, the Na^+ is more likely to be neutralized via charge transfer directly with the O^- existing on the surface. Following such a charge transfer process, an energetic oxygen atom, possibly even an excited oxygen atom, will recoil into the surface layer and then can be reflected toward the vacuum. This oxygen atom will prefer being O^- again and can acquire an electron from the metal on a time scale of $\sim 10^{-15}$ s, which is short compared to that for exiting the surface, $\sim 10^{-14}$ s.

Under any circumstances, if O^- is ejected from the surface by the collision cascade with a large enough velocity, it will survive as a negative ion independently of the exact sputtering mechanism or oxygen coverage. The survival probability depends on the exit velocity normal to the surface and can be calculated from the fundamental rate equation [34],

$$dP^-(t) = -\Delta[z(t)]P^-(t)dt, \qquad (3.3)$$

with the initial condition, $P^-(t_o) = 1$, and the decay width, $\Delta(z(t))$. The solution of Eq. 3.3 gives the survival probability, P_{ion}^∞, of the O^- ejected by the collision cascade and can be expressed as,

$$P_{ion}^{\infty}[v_{\perp}(z)] = \exp\left[-\int_{z_c}^{\infty}\frac{\Delta(z)dz}{v_{\perp}(z)}\right], \tag{3.4}$$

where $v_{\perp}(z)$ is the exit velocity of O^- normal to the surface, and z_c is the distance from the surface where the magnitude of the affinity level of O^- is equal to the metallic work function, $|E_A(z_c)| = \phi$. If O^- is ejected from the surface with a kinetic energy, E, at an angle, θ, (with respect to the surface normal), the probability that it survives as an anion, P_{ion}^{∞}, can be expressed as,

$$P_{ion}^{\infty}(E, \theta) \approx \exp\left[-\int_{z_c}^{\infty}\frac{\Delta_M(z)\,dz}{\sqrt{\frac{2}{m}\left[E + \frac{1}{4}\left(\frac{1}{z} - \frac{1}{z_c}\right)\right]}\cos(\theta)}\right], \tag{3.5}$$

where $\Delta_M(z)$ is the resonance width and m is the mass of O^-. The denominator in Eq. 3.5 represents the exit velocity of the ion, normal to the surface, under the influence of the image potential. In order to calculate an average survival probability with Eq. 3.5, the resonance width, $\Delta_M(z)$, of each magnetic substate and the angular and kinetic energy distribution for those O^- ions which are launched from the surface into the vacuum must be known. The widths, specifically for the Al/O system, have been calculated for each magnetic substate and approximated by the form [51],

$$\Delta_M(z) \approx \Delta_{Mo}e^{-\gamma_M z}. \tag{3.6}$$

The magnetic substates of O^- in front of an Al surface have rather different widths. The

width for the $m_t = 0$ state is substantially smaller than that for $m_t = \pm 1$, which implies that the $m_t = 0$ substate is the more likely substate to survive as a negative ion as it leaves the surface. Linear collision cascade theory predicts a launch distribution (as a function of the energy and sputtering angle) to be of the form [27,28],

$$E_{ion}^{cc}(E, \theta) = \left[\frac{CE}{(E + U)^3}\right]\cos(\theta),\qquad (3.7)$$

where C is a constant and U is typically referred to as the surface binding energy. Given the launch distribution, $E_{ion}^{cc}(E, \theta)$, the survival distribution function for each magnetic substate, averaged over all angles (assuming azimuthal symmetry), is,

$$S_{ion, m_t}^{cc}(E) \approx \frac{1}{2\pi}\int E_{ion}^{cc}(E, \theta)\, P_{ion, m_t}^{cc}(E, \theta)\, d\Omega.\qquad (3.8)$$

The total O⁻ kinetic energy distribution is the sum of all the magnetic substate distributions,

$$S_{tot}^{cc}(E) = \frac{1}{3}\sum_{m_t = 0, \pm 1} S_{ion, m_t}^{cc}(E).\qquad (3.9)$$

The energy distributions of the surviving ions calculated from Eq. 3.8 can be compared directly to the experimentally observed kinetic energy distributions of the sputtered O⁻.

Shown in Fig. 3.10 are the experimental results for an impact energy of 450 eV and an oxygen dose of about 100 L and collision cascade calculations using Eq. 3.8. The values of the parameters used in the calculation are listed in Table 3.1. The value for the
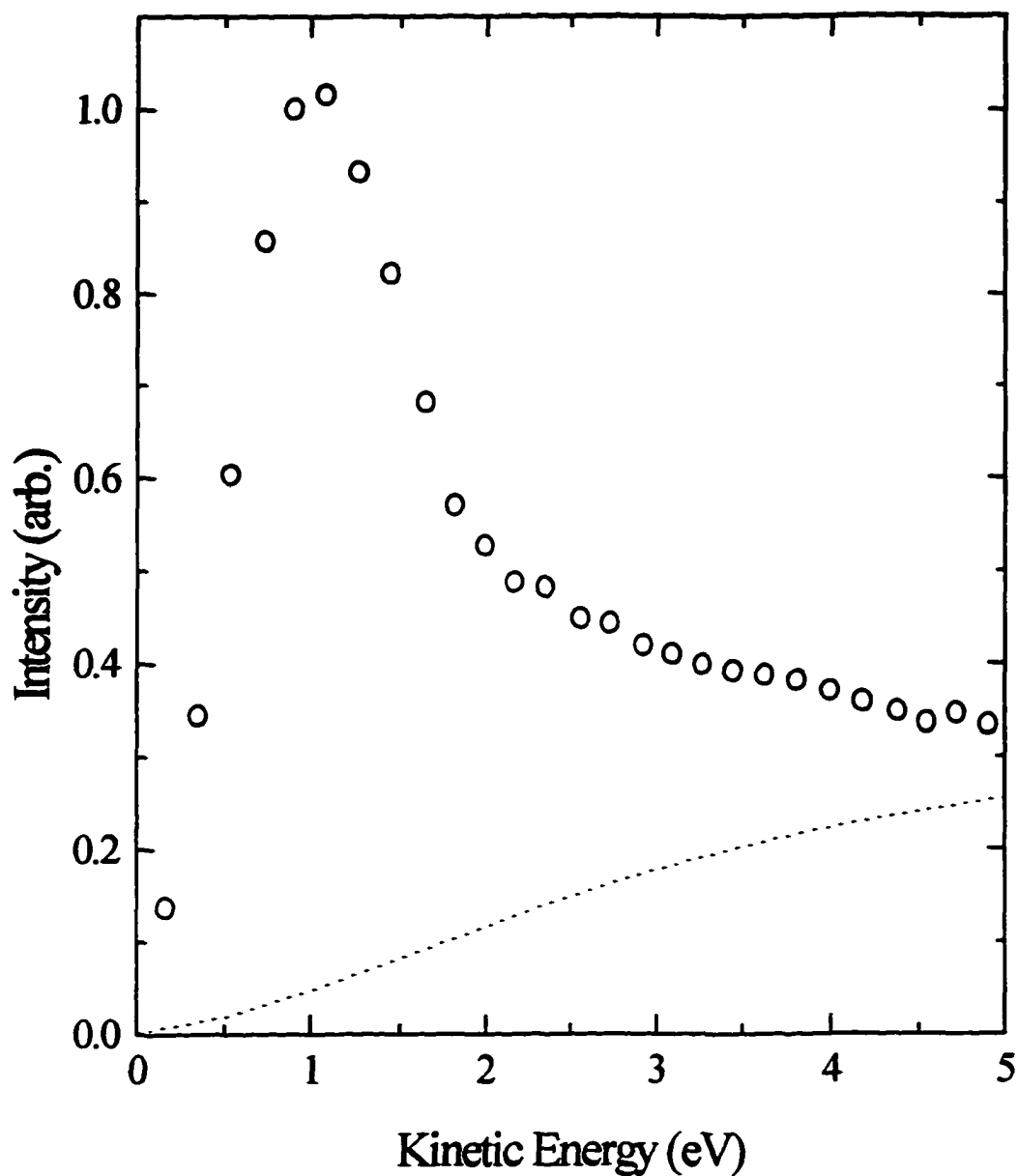
Fig. 3.10 Experimental (o) sputtered O⁻ kinetic energy distribution for 450 eV Na⁺ impacting an Al surface exposed to 92 L of oxygen and the calculated (····) O⁻ kinetic energy distribution due to the collision cascade of Eq. 3.8.

Table 3.1   Aluminum Collision Cascade Parameters

Parameter		Value
$m_\ell = 0$ Δ_{Mo}		2.414 eV
$m_\ell = 0$ γ_M		0.731 a_o^{-1}
$m_\ell = \pm 1$ Δ_{Mo}		3.172 eV
$m_\ell = \pm 1$ γ_M		0.630 a_o^{-1}
z_c		3.17 a_o
C		2.0 eV
U		1.0 eV

surface binding energy, U, was chosen to provide the best fit to the experimental results. The calculated energy distribution is the statistical sum of all the m_ℓ substate distributions as given by Eq. 3.9. As seen in Fig. 3.10, the simple, linear collision cascade model fails to completely reproduce the experimental results. Specifically, the maxima in the kinetic energy distributions generated by Eq. 3.8 occur at considerably higher kinetic energies than that which is experimentally observed. This is due to the fact that $P_{ion}^{\infty}(E,\theta)$ is a sharply increasing function of E, thus displacing the maximum in the collision cascade distribution function (which occurs at $E = U/2$) to much higher energies when the collision cascade function is convoluted with the survival probability. There are no plausible parameter adjustments which can bring the model's prediction into accord with the observed kinetic energy distribution.

To account for the observed spectra, particularly the relatively sharp peak

observed at ~ 1 eV, the collision cascade model must be augmented by another mechanism by which O⁻ can be sputtered from the surface due to low-energy ion bombardment. It should be mentioned that the experimental distribution could be fitted with the addition of a term which describes the desorption as a thermal phenomena into the energy distribution [66]. The thermal term predicts a Maxwell-Boltzmann distribution and would have the form,

$$S(E) \propto E \, e^{-\frac{E}{U}}. \qquad (3.10)$$

This type of distribution mimics the energy distribution associated with the sputtering after the collision cascade reaches a thermal equilibrium producing a "hot spot" or thermal spike from which ions can evaporate, i.e. the sputtering which occurs after most of the momentum of the impacting particle has been transferred to the lattice. However, this description of the ion-surface interaction is non-physical for the low impact energies of these experiments.

3.3.3 Origin of Secondary Electrons

The secondary electrons observed in these studies, at impact energies < 500 eV, cannot originate from potential emission because of the low ionization potential of Na, nor can they be attributed to direct kinetic emission since this requires substantial momentum transfer to a conduction band electron which is only likely to occur for impact energies in the keV range. Also, there is no evidence whatsoever of any additional structure in the

observed secondary electron kinetic energy spectra at higher kinetic energies (greater than a few eV). This implies that there are no electrons arising from the decay of either autoionizing O^{**}, or autodetaching levels of excited negative oxygen ions, $(O^-)^*$, exiting the surface, which would have kinetic energies in the range of $\sim 8 - 20$ eV [67, 68].

Secondary electron emission is correlated to the emission of negative oxygen ions in the sense that both $Y_O^-(\Theta_s)$ and $Y_e^-(\Theta_s)$ exhibit the same energetic threshold independent of the oxygen coverage, Θ_s, and both increase similarly with increasing Θ_s at a given impact energy. If the two processes are also correlated in time, a single event must provide enough energy (at least twice the work function) to simultaneously remove two negative charges from the surface. One way to supply this much energy is by the formation of excited oxygen atoms on the surface. The neutralization of an impacting Na^+ via direct charge transfer from the O^- residing on the surface provides a possible mechanism for the production of excited oxygen atoms. Charge transfer reactions for binary collisions of Na^+ with O^- can result in ground and excited state oxygen:

$$Na^+ + O^- \rightarrow Na + O(^3P) + 3.6 \text{ eV}$$
$$\rightarrow Na + O(^1D) + 1.6 \text{ eV} \qquad (3.11)$$
$$\rightarrow Na + O(^1S) - 0.5 \text{ eV},$$
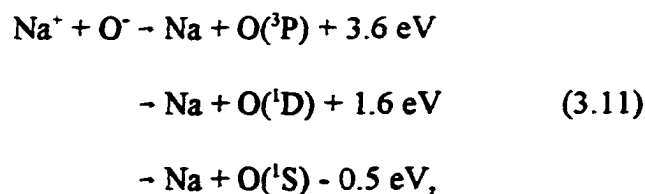
where the asymptotic exothermicities are listed. An excited oxygen atom, say an $O(^1S)$ recoiling toward the surface, then could initiate a process by which O^- is formed again and possibly ejected into the vacuum, and at the same time, a secondary electron could be

ejected. The condition for the emission of *both* an O⁻ and an electron from a single impacting Na⁺ is that the magnitude of the affinity level, at a distance z from the surface, be at least twice the work function. For $O(^1S)$, this can occur for z < 2.5 a_o since the affinity level of $O(^1S)$ lies ~ 4 eV below that of ground state oxygen, $O(^3P)$ [51]. At z = 2.5 a_o, the magnitude of the affinity level of $O(^1S)$ is 8.4 eV, i.e., twice the work function of Al. The formation of O⁻, by either resonant or direct transfer of a metal electron to $O(^1S)$, can provide sufficient excess energy to enable an additional electron to escape into the vacuum. For resonant transfer, an electron tunnels from the metal to the O⁻ vacancy, and a hole will be created in the conduction band and subsequently filled. The energy released by filling this hole can be transferred to a second electron which may be ejected into the vacuum if the de-excitation energy is greater than the work function. Similarly, the O⁻ vacancy can be filled directly by an electron from near the fermi level which can release enough energy to eject another electron. With either method, both an O⁻ and an electron could be ejected from a single impacting Na⁺.

The cross sections for the charge transfer reactions given in Eq. 3.11 have not been determined for binary gas-phase collisions, and nothing is known concerning their surface analogies. Nevertheless, one can speculate that the probability for forming $O(^1S)$ should be small at low collision energies owing to the large separation between the potential energy of the products {$Na(^2S) + O(^1S)$} and that for the coulombic reactants {$Na^+ + O^-$} which develops as Na⁺ approaches O⁻. Thus, although the asymptotic energy defect for forming $O(^1S)$ is small, the cross section for producing $O(^1S)$ would be small for low collision energies and should increase with increasing impact energy. In fact, the

cross section for forming $O(^1S)$ would be anticipated to increase in a manner not unlike that observed for $Y_e^-(E)$.

Additional results appeared to support a simultaneous ejection mechanism. The electron-O^- ratio (Y_e^-/Y_O^-, or the number of secondary electrons ejected for every O^-) increased with the oxygen exposure of the surface for all impact energies. As illustrated in Fig. 3.11, for small exposures, the ratio was small, *viz.*, ~ 0.2, but there was a large increase in the ratio with oxygen exposures up to ~ 100 L as more electrons were being ejected for every O^- sputtered. It was reasoned that as the oxygen coverage increased, the probability for forming $O(^1S)$ via charge transfer with Na^- would increase as would the corresponding probability for secondary electron emission. As there are several mechanisms for direct sputtering of O^- which do not involve the initial neutralization of O^- (and hence do not provide a mechanism for ejecting a secondary electron), the ratio Y_e^-/Y_o^- was expected to increase until surface saturation was achieved for exposures in the neighborhood of 100 L. This was in fact observed to be the case.

In order to investigate this correlated ejection mechanism directly, the TOF spectrometer was operated in a mode where the Na^+ beam was allowed to continuously impact the surface, while both the sputtered negative ion and electron events were collected in a multi-channel scaler (640 ns bin-width). Typically, around 2×10^5 events were recorded at a bin-occupancy probability of 10%, and this temporal spectrum was subjected to an autocorrelation study. If the emission of an electron occurs simultaneously with that of a negative oxygen ion, a peak should be identifiable in the resulting autocorrelation spectrum due to the difference in the flight times (~ 6 μs) of the electrons
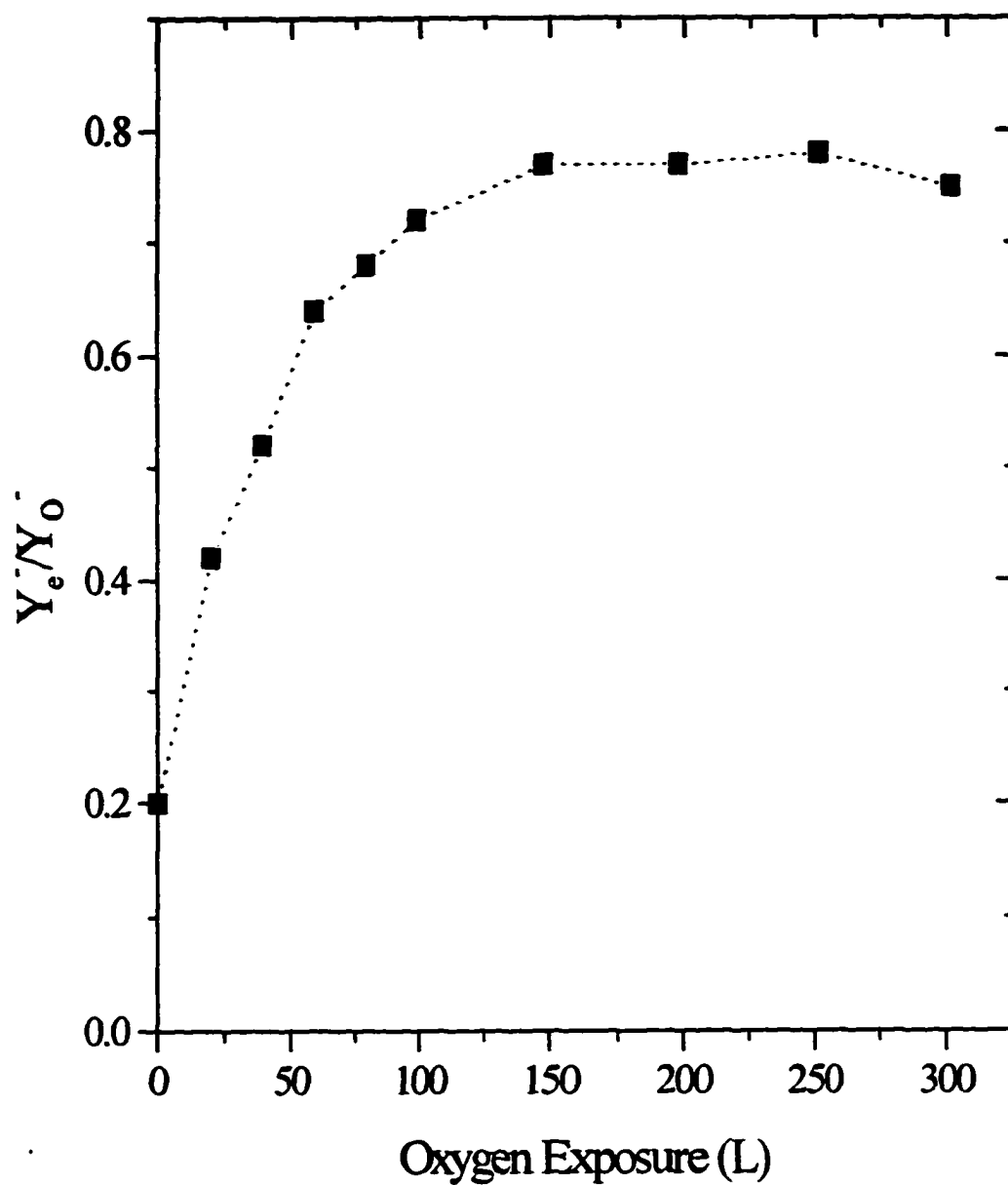
Fig. 3.11 Electron-O⁻ ratio, Y_e^-/Y_O^-, as a function of oxygen exposure of the Al surface at a fixed Na^+ impact energy of 250 eV.

and the O⁻ in traveling from the surface to the detector. No evidence of any correlation was found at any impact energy or oxygen exposure. Artificially generated data sets, with count rates adjusted to replicate the experiment, were run through the same autocorrelation routine and showed that a correlation would have been observed if it was as small as 0.1% (i.e., if 0.1% of the events were correlated). Hence, simultaneous emission of an electron and O⁻ does not readily occur, and this mechanism is not the primary source of secondary electron emission from oxidized aluminum at low impact energies. Thus, to summarize the observations concerning secondary electron emission: (1) the secondary electron yield is strongly dependent on the amount of adsorbed oxygen and increases in an approximately linear manner with the coverage; (2) the kinetic energy distributions have widths of 1.0 - 1.5 eV and peak around 0.9 eV, and they are insensitive to impact energy; (3) the ejection probability increases with increasing impact energy above a threshold of ~ 50 eV; (4) electron emission is not correlated with simultaneous O⁻ emission.

3.3.4 Ion and Electron Emission Mechanism

At this point, we have no mechanism which provides an adequate description of either the secondary ion or electron emission process. The salient features of the electron and ion kinetic energy spectra in the experiments are, most notably, their independence of impact energy and the similarity of their most probable kinetic energies. These features suggest that we describe the low-energy sputtering process in terms of an electronic excitation followed by desorption. This excitation, initiated by the impacting Na⁺ ion,

serves as a precursor for both O^- and electron ejection into the vacuum. Let us assume that oxygen, adsorbed on the Al surface as O^-, can be collisionally excited into an $(AlO^-)^*$ repulsive state as shown schematically in Fig. 3.12. We will take the excitation probability, $P_x(z)$ to be a Gaussian distribution centered at z_{eq}, the equilibrium distance of the adsorbed O^- from the reflection plane, having the form,

$$P_x(z) = \sqrt{b/\pi}\exp[-b(z - z_{eq})^2],\qquad (3.12)$$

where $1/b^{1/2}$ is the width of the distribution. After the excitation occurs, the negative ion can exit the surface and possibly decay by emission of an electron to metal or to the vacuum. While decay by electron emission to the metal can occur for any distance, decay by electron emission to the vacuum can occur for any value of z where the $(AlO^-)^*$ energy lies above that for AlO plus a free electron (≤ 4.35 a$_0$ in Fig.3.12). The O^- survival probability for the excitation mechanism, $P_{ion}^{ex}(z)$, as given by Eq. 3.4, can be written as,

$$P_{ion}^{ex}(z) \approx \exp\left[-\int_z^\infty \frac{\Delta_{TOT}(z')dz'}{v(z')}\right],\qquad (3.13)$$

where $v(z)$ is the exit velocity determined by the $(AlO^-)^*$ potential. Let us again approximate the widths for decay of the $(AlO^-)^*$ by electron emission to the metal and to the vacuum by the forms,

$$\Delta_M(z) \approx \Delta_{Mo}e^{-\gamma_M z} \quad \text{and} \quad \Delta_V(z) \approx \Delta_{Vo}e^{-\gamma_V z},\qquad (3.14)$$
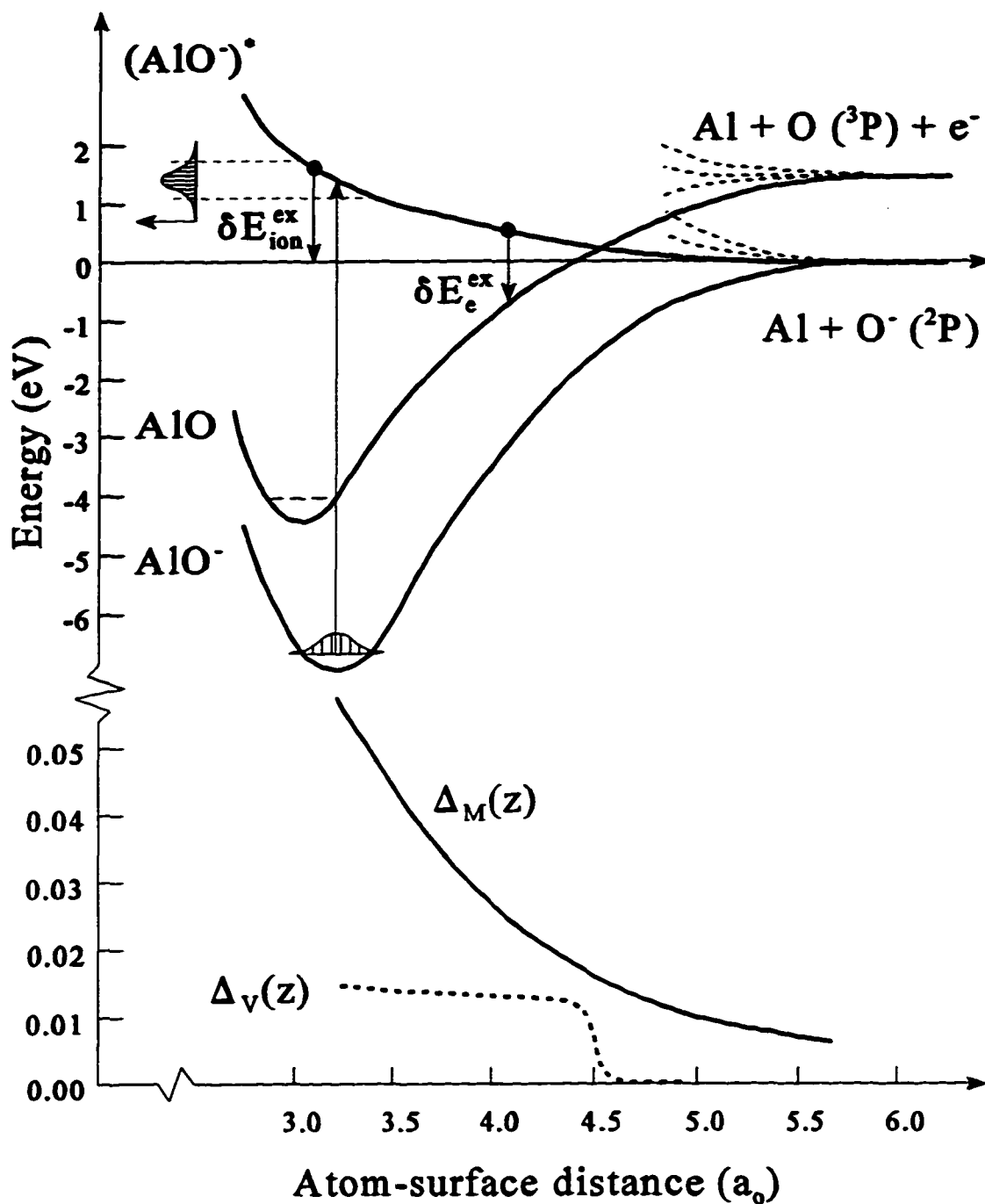
Fig. 3.12 Schematic diagram of the molecular states for the interaction of O and O⁻ with an Al surface as a function of distance from the surface. Also shown are the decay widths used to describe the two decay channels. The AlO and AlO⁻ ground states depicted are the isolated molecular curves representing the ion-surface interaction.

and the total decay width is then,

$$\Delta_{TOT}(z) = \Delta_M(z) + \Delta_V(z) \, . \tag{3.15}$$

The non-constant exit velocity is given by,

$$v(z) \approx \sqrt{\frac{2}{m} K_{ion}^{ex}(z)} \, , \tag{3.16}$$

where $K_{ion}^{ex}(z)$ is the kinetic energy of the ion as it exits the surface along the $(AlO^-)^*$ potential curve. The energy associated with the excitation above the vacuum level is approximated by,

$$\delta E_{ion}^{ex}(z) \approx E_s \left(\frac{z_{eq}}{z}\right)^2 , \tag{3.17}$$

where E_s is the energy of the $(AlO^-)^*$ potential curve, above the vacuum level, at the distance of the most probable excitation, z_{eq}. The kinetic energy of an exiting ion at a distance z, which was originally excited to the $(AlO^-)^*$ potential curve at a distance z_i, $(z > z_i)$ is given by,

$$K_{ion}^{ex}(z) = \delta E_{ion}^{ex}(z_i) \left[1 - \left(\frac{z_i}{z}\right)^2\right] + K_i \, , \tag{3.18}$$

where K_i is the initial kinetic energy of the ion due to momentum transfer. Thus, the

energy distribution function for the surviving negative ions is given by,

$$S_{ion}^{ex}(E) \approx \frac{1}{E_n^2} P_x(z) \, P_{ion}^{ex}(z) \, \delta E_{ion}^{ex}(z) \,, \qquad (3.19)$$

where E_n is a normalization constant determined from the total integrated survival probabilities. This mathematical function (Eq. 3.19) implies that if the O^- is excited, $P_x(z)$, and it survives to infinity, $P_{ion}^{ex}(z)$, then it would have a kinetic energy equal to $\delta E_{ion}^{ex}(z)$. The product, $P_x(z) \, \delta E_{ion}^{ex}(z)$, is shown as an approximation in Fig. 3.12.

The kinetic energy distribution of the electrons which decay into the vacuum also can be calculated and compared to the experimental results. The probability of O^- decay by emission of an electron to the vacuum, $P_e^{ex}(z)$, can be expressed as:

$$P_e^{ex}(z) = \left[1 - P_{ion}^{ex}(z)\right] \left[\frac{\Delta_V(z)}{\Delta_{TOT}(z)}\right]. \qquad (3.20)$$

The first term represents the probability that the O^- does *not* survive into the vacuum (i.e. the probability of decay to all open channels), and the second term is the branching ratio of electron emission to the vacuum to the total decay. The energy of the electrons emitted to the vacuum is the energy difference between the $(AlO^-)^*$ and the neutral AlO potential energy curves. Due to the fact that the potential curves cross far from the surface, it is reasonable to assume a linear crossing in order to estimate the energy difference. The resulting energy of the electrons emitted to the vacuum is,

$$\delta E_e^{ex}(z) \approx F_x(z_x - z) \,, \qquad (3.21)$$

where z_x is the distance from the surface of the curve crossing and F_x is the electric field strength at the curve crossing and has units of eV a_o^{-1}. Accordingly, the kinetic energy distribution of the secondary electrons is,

$$S_e^{ex}(E) \approx \frac{1}{E_n^2} P_e^{ex}(z) \delta E_e^{ex}(z), \qquad (3.22)$$

where E_n is the normalization constant. In order to calculate the kinetic energy distributions of the negative ions and the secondary electrons generated by Eqs. 3.19 and 3.22 respectively, the widths, $\Delta_M(z)$ and $\Delta_V(z)$, must be estimated and are illustrated in Fig. 3.12. The estimates of the widths are based on those calculated for the Al/O system by Bahrim, et al. [51]. The values for these widths and the other parameters used in calculating the O⁻ kinetic energy distribution are summarized in Table 3.2.

The resulting kinetic energy distribution of O⁻ desorbing via this mechanism is shown in Fig. 3.13. The sum of this distribution and that due to the collision cascade can provide a reasonable fit to the experimentally observed kinetic energy distribution. The collision cascade model accounts for the high energy portion of the spectrum whereas $S_{ion}^{ex}(E)$ supplies the relatively narrow "pulse" at low kinetic energies. In the fit shown in Fig. 3.13, the relative contribution of the electronic excitation mechanism to the collision cascade in the total distribution is approximately 1.8:1.

Finally, the calculated electron kinetic energy distribution from the decay of O⁻ by electron emission to the vacuum is shown in Fig. 3.14. Again, this provides a reasonable fit to the observed electron kinetic energy spectrum. The most probable electron energy is

Fig. 3.13 Experimental (o) sputtered O⁻ kinetic energy distribution for 450 eV Na⁺ impacting an Al surface exposed to 92 L of oxygen and the calculated kinetic energy distribution of the collision cascade augmented by the excitation/desorption mechanism. The collision cascade (····) kinetic energy distribution, as predicted by Eq. 3.8, and the excitation mechanism (– – – –) kinetic energy distribution, as predicted by Eq. 3.19, add to form the total (——) distribution.
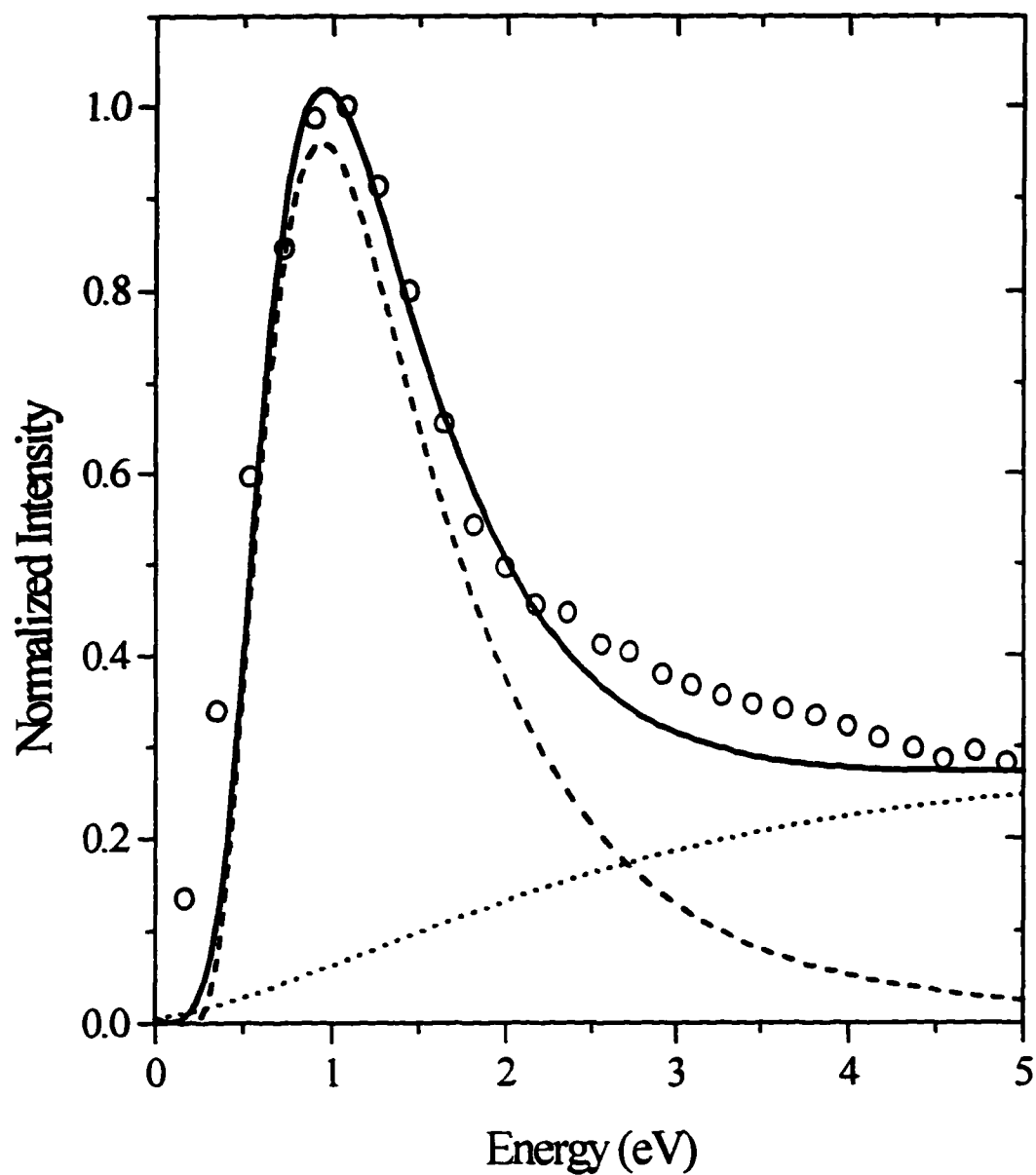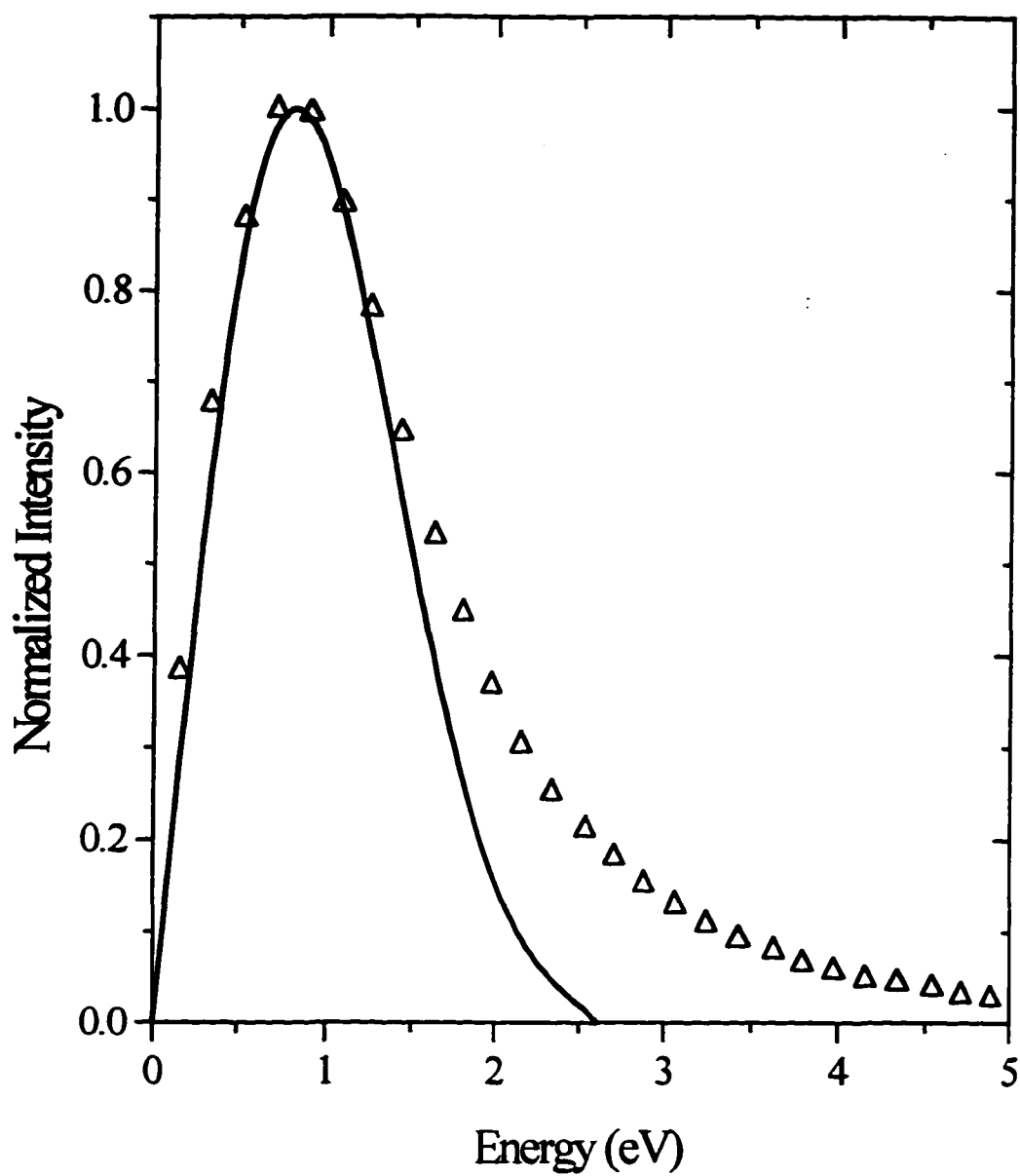
Fig. 3.14 Experimental (△) secondary electron kinetic energy distribution for 450 eV Na⁻ impacting an Al surface exposed to 92 L of oxygen and the calculated (——) secondary electron kinetic energy distribution predicted by Eq. 3.22.

Table 3.2   Aluminum Excitation Mechanism Parameters

Parameter	Value
E_s	1.4 eV
K_i	0.1 eV
E_n	0.46 eV $a_o^{-1/2}$
F_x	0.6 eV a_o^{-1}
b	0.3 a_o^{-2}
z_{eq}	3.17 a_o
z_x	4.35 a_o
Δ_{Vo}	0.0215 eV
γ_V	0.119 a_o^{-1}
Δ_{Mo}	1.0 eV
γ_M	0.9 a_o^{-1}

not associated with a small value of z ($z = z_x$, for example) owing to the fact that the

principal decay mechanism for small z, by far, is for the electron to return to the

conduction band of the metal. The values of the parameters used in calculating the

electron kinetic energy distribution also are summarized in Table 3.2.

In summary, the kinetic energy distributions of secondary electrons and O^-

sputtered from an aluminum surface have been determined. It has been shown that the

observed ion kinetic energy distributions cannot be explained by conventional collision

cascade theory alone. Similarities in the O^- and electron kinetic energy distributions and

their independence of impact energy have lead to an electronic excitation mechanism for

the emission of both negative ions and electrons. The widths used in these calculations have been adjusted to bring the calculation into accord with the observations, and the potential curves shown in Fig. 3.12 clearly are representative of a family of molecular states and are intended only to be a representation of the true ion-surface interaction. Yet, using plausible estimations, this mechanism, together with the collision cascade, can reproduce both the experimentally observed ion and electron kinetic energy distributions.

3.3.5 Work Function Effects on Emission

It has been known for some time that adsorbed alkali metal decreases the work function leading to increased ion emission from metal surfaces. In order to investigate the effects of Na and O coverages on the work function of the polycrystalline Al surface specific to these experiments and its relation to secondary emission, measurements of changes in the work function were made using photoelectron emission. The Al surface was exposed to a known amount of oxygen, and then the surface was allowed to accumulate Na via a 250 eV Na^+ beam. The photoelectron emission was monitored first as 350 nm UV light was incident upon the surface, to identify the 3.5 eV threshold, and then the 300 nm filter was inserted to identify the 4.1 eV threshold. The results are shown in Fig. 3.15 as a function of the Na^+ dose for oxygen exposures of 50 and 100 L. Linear fits to the photoelectron currents, extrapolated to zero, determine the thresholds in terms of Na^+ dose. In the case of sodium, the change in the work function, $\Delta\phi_{Na}$, due to a 100 nA min dose was ~ -0.6 eV. The oxygen-induced change in the work function was determined by comparing the threshold difference between the two exposures to $\Delta\phi_{Na}$.
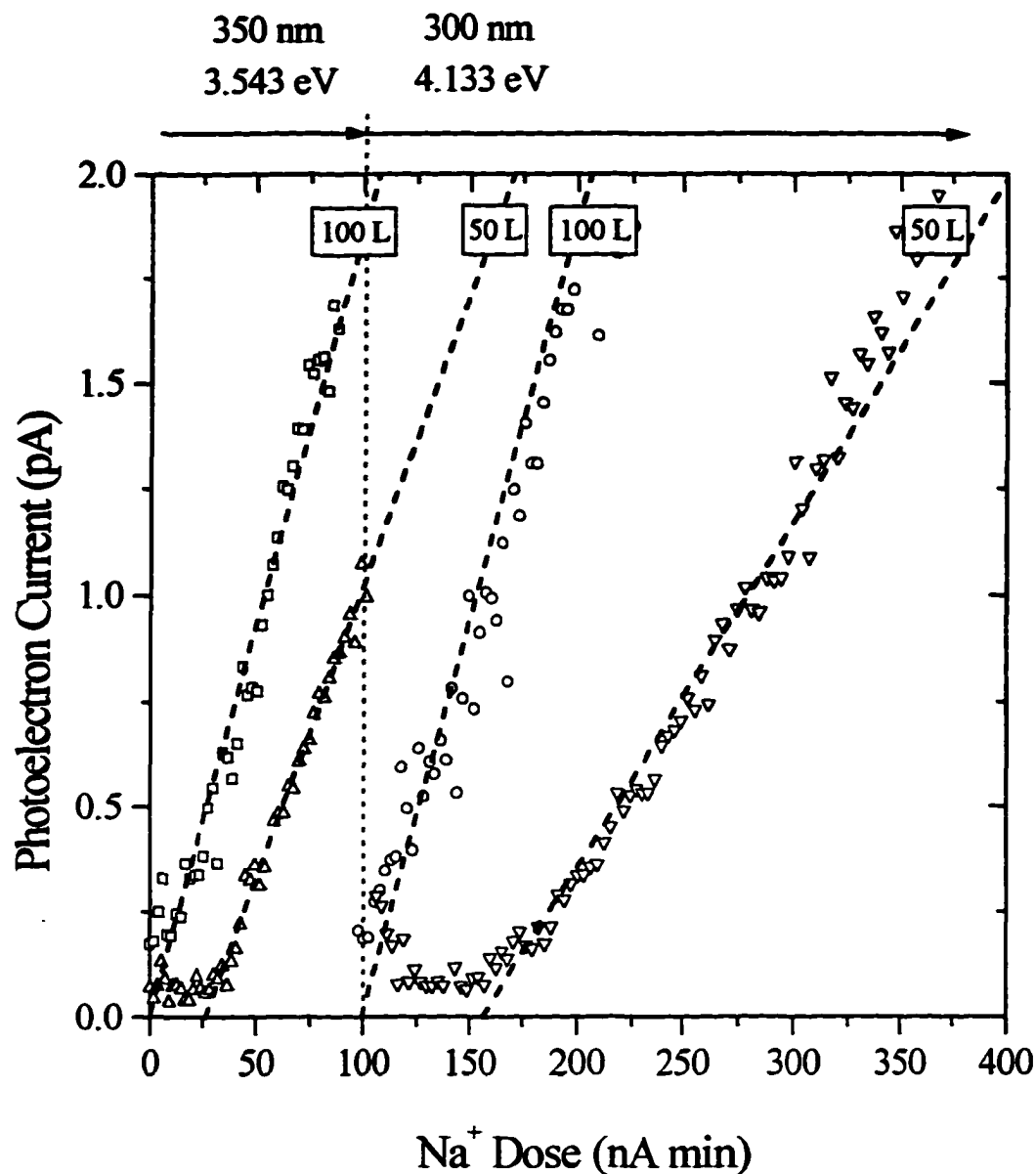
Fig. 3.15 Photoelectron current as a function of Na⁺ dose of the surface for 50 and 100 L oxygen exposed Al surfaces. For 0 - 100 nA min, the photoelectron emission was monitored as 350 nm UV light was incident on the surface, and above 100 nA min, it was measured as 300 nm UV light was incident on the surface. The results are shown for 50 L (△ - 350 nm, ▽ - 300 nm) and 100 L (□ - 350 nm, ○ - 300 nm) oxygen exposed surfaces. Linear fits (dashed lines) to the measured photoelectron currents identify the thresholds for emission which correspond to work functions of 3.5 and 4.1 eV. The difference in the thresholds at the same oxygen exposure is a 0.6 eV lowering of the work function induced by adsorbed Na. The change in the work function due to oxygen exposure is found by taking the difference between the thresholds for two different oxygen exposures (in terms of nA min) and comparing that to the change due solely to Na.

An exposure of 50 L of oxygen also decreases ϕ, with a $\Delta\phi_O$, $-0.48 \le \Delta\phi_O \le -0.12$ eV. A similar decrease in the work function of polycrystalline Al due to oxygen exposure has been reported by Esaulov, et al. [62], who measured a $\Delta\phi_O$ of ~ -0.2 eV for a 50 L exposure.

The O^- yield from an Al surface at a fixed impact energy is observed to increase approximately linearly as the amount of adsorbed O increases. This is undoubtedly due to there being more targets to sputter and the oxygen-induced decrease in the work function. In a similar manner, Y_O^- at a fixed impact energy from an Al/O surface also exhibits a large increase with Na coverage of the Al surface. As the accumulated Na decreases ϕ, the distance, z_c, at which $|E_A(z_c)| = \phi$ also increases leading to an increased survival probability of the O^- exiting the surface as an ion. Like Y_O^-, Y_e^- is strongly dependent on the O coverage, but there is only a small increase observed in Y_e^- with increased Na coverage. The difference in the dependence of Y_O^- and Y_e^- on the change in the work function is consistent at all impact energies and oxygen coverages of the surface. This difference is illustrated clearly in Fig. 3.16 where the electron-O^- ratios (Y_e^-/Y_O^-) are shown as functions of sodium dose and oxygen exposure for several impact energies. The decreasing ratios in Fig. 3.16a are evidence that more oxygen negative ions are sputtered for every secondary electron emitted as ϕ decreases. However, even though ϕ also decreases with oxygen coverage, the ratio *increases* as is shown in Fig. 3.16b. Thus, the increase in Y_e^- due to oxygen exposure cannot be attributed simply to an oxygen-altered work function. A similar conclusion was made for collisions of Ar^+ with Al/O at an impact energy of 30 keV [8]. Even though the total yield increases linearly with oxygen

coverage (for $\Theta_s < 1$), the branching ratio does change in favor of electron emission as shown in Fig. 3.16b.
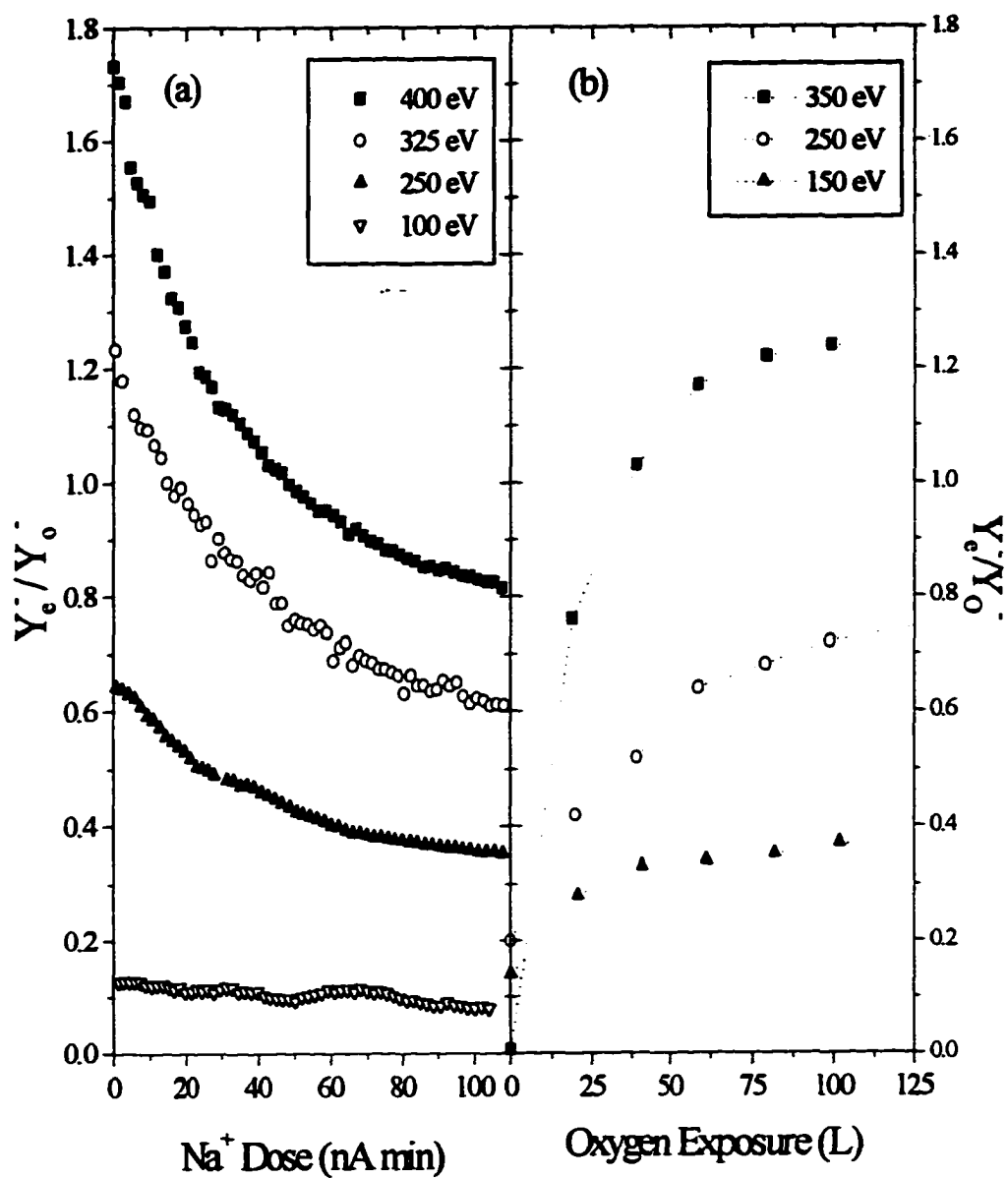
Fig. 3.16 (a) Electron-O⁻ ratio, Y_e^-/Y_O^-, as a function of Na⁺ dose for Na⁺ impacting an Al surface, with oxygen exposure of ~ 25 L, at impact energies of (▽) 100 eV, (▲) 250 eV, (○) 325 eV and (■) 400 eV. (b) The ratio as a function of oxygen exposure at impact energies of (▲) 150 eV, (○) 250 eV and (■) 350 eV.

CHAPTER 4

MOLYBDENUM

4.1 Polycrystalline Molybdenum

The experiments on polycrystalline Mo surfaces were designed to expand on the experimental investigations of gas covered Mo surfaces by Baker, et al. [7] examining, in detail, the secondary electron and negative ion emission dependence on oxygen coverage. Unless otherwise noted, the Mo samples were prepared in the following manner: (1) 4 keV Ar^+ sputtering over an area larger than that sampled for 1 hr. at a current density $> 1.0 \ \mu A/cm^2$; (2) resistively heating the sample to ~ 1000 K for 10 min.; (3) sputtering again for 30 min. The surface cleanliness was ascertained by SIMS and by measuring $Y_T^-(250 \ eV)$ and confirming that $Y_T^-(250 \ eV) \le 0.1$ %. After the first sputter cleaning cycle, a small amount of Na^- was observed in the SIMS spectra, indicating a small amount of Na which was not removed by sputtering. Thus, the surface was heated to desorb the remaining Na, followed by an additional sputter cleaning cycle to remove contaminants thermally desorbed from other elements near the surface during the heating process. As previously done with Al, the total Na dose of the surface was minimized for both the yield and energy distribution measurements.

4.1.1 Polycrystalline Molybdenum Results

4.1.1.1 Yields - Oxygen Saturated Surface

The previous experiments by Baker, et al. [7] ascertained the effects of sodium

69

coverage on secondary emission from an oxygen saturated, polycrystalline Mo surface at low impact energies, however, oxygen could not be removed from the metallic surfaces in those experiments. Similar experiments were performed with the present experimental arrangement by over-saturating the surface with a 25 L oxygen exposure, heating the sample and then allowing Na to accumulate on the surface via a 250 eV Na^+ beam. The yields are shown as a function of impact energy in Fig. 4.1. The yield results for an oxygen saturated, Na-free surface are observed to increase with impact energy above a common impact energy threshold at ~ 50 eV. As was the case with Al, the dependence of Y_x^- and Y_e^- on impact energy is rather different. As $Y_x^-(E)$ saturates at impact energies around 200 eV, $Y_e^-(E)$ is continually increasing and dominates the negative emission at the higher impact energies. These yield results for an oxygen saturated surface are in excellent quantitative agreement with those of Baker, et al. [7], where the experimental arrangement was considerably different. This fact is paramount to the present experimental observations for two reasons. First, it provides further support for the initial assumption that the electron-ion ratio determined at the split lens reflects the true electron-ion ratio for all the negative products collected at both the split lens and lens 1. Second, the magnitudes of the yields at a given impact energy are identical (within experimental accuracy of $\pm$ 15 %), thus ensuring absolute collection of all the secondary ions and electrons with the present experimental arrangement. Finally, as illustrated in Fig. 4.1, a monolayer of Na on the surface leads to an increase in both Y_x^- and Y_e^- at all impact energies. As was observed for the Al surface, the lowering of the work function associated with the Na coverage of the Mo surface has a greater effect on the negative ion
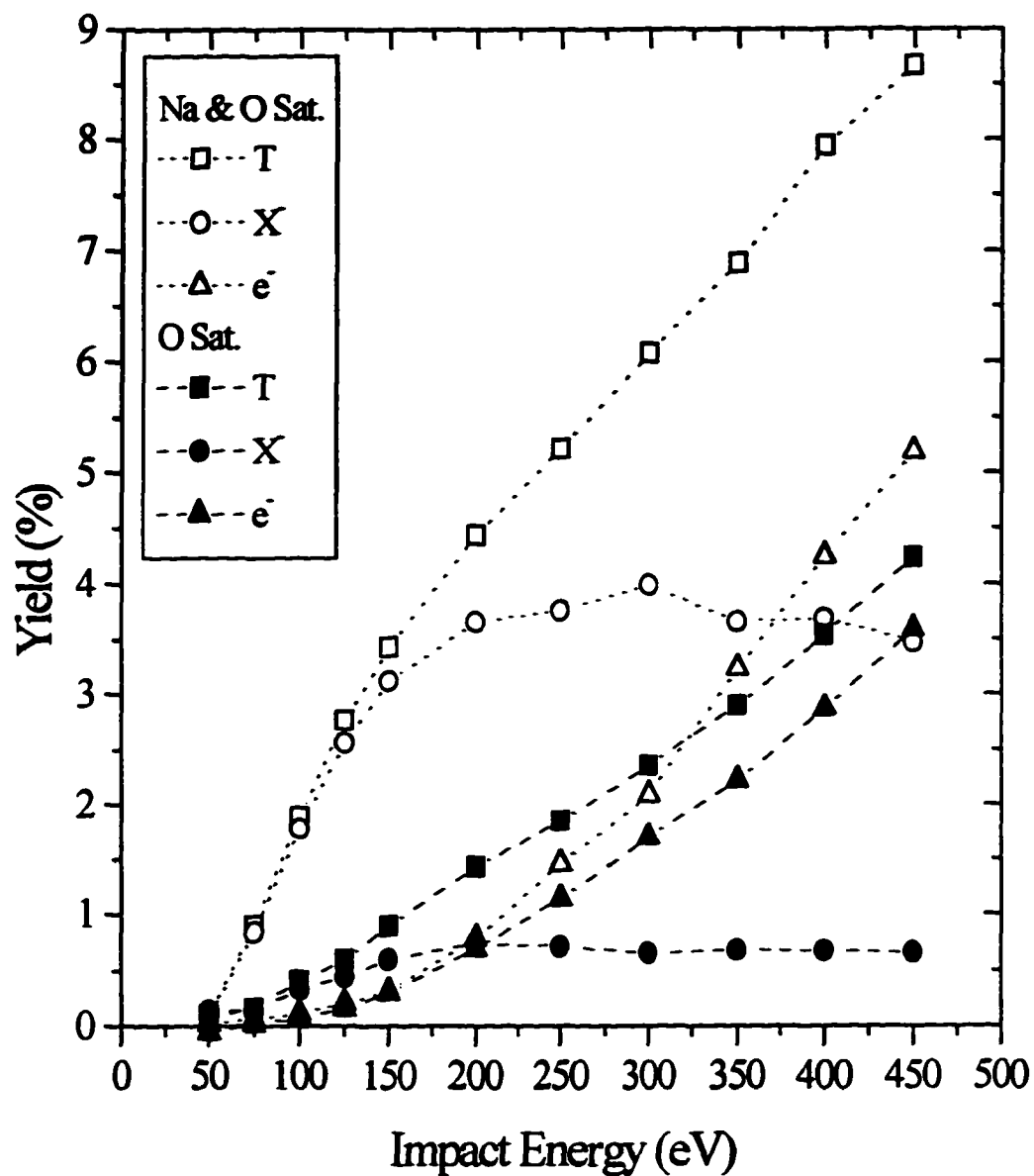
Fig. 4.1 Absolute (■) total, (●) negative ion and (▲) electron yields as a function of impact energy for Na^+ impacting an oxygen saturated Mo surface. Absolute (□) total, (○) negative ion and (△) electron yields as a function of impact energy for an oxygen *and* sodium saturated Mo surface.

emission relative to that for the secondary electron emission.

4.1.1.2 Yields - Oxygen Coverage Dependence

In order to determine the dependence of Y_X^- on oxygen coverage, the negative ion

constituents of Y_X^- were identified first with the previously described TOF technique by

pulsing the Na^+ beam at 2 kHz at a pulse width of 0.25 μs. Two TOF spectra for a

moderate oxygen exposure of ~ 6 L at impact energies of 250 eV and 350 eV are shown

in Fig. 4.2. The negative ions observed in these spectra are the dominant O^- and trace

amounts of H^- and O_2^-. Due to the dominance of O^- (this dominance is also observed at all

other impact energies and oxygen exposures) the negative ion yield is essentially the

negative oxygen ion yield, $Y_X^- \approx Y_O^-$. Thus, the secondary electron and oxygen negative

ion yields for the polycrystalline Mo surface are shown in Fig. 4.3 as a function of oxygen

exposure at an impact energy of 250 eV. Both yields are observed to increase with

exposure until they begin to saturate at ~ 3.5 L, which coincides with the onset of

saturation of oxygen uptake of the Mo surface [69]. While a large increase is observed in

$Y_e^-(\Theta_s)$ for exposures below ~ 3.5 L, there is a somewhat smaller increase in $Y_O^-(\Theta_s)$. The

different dependence of $Y_e^-(\Theta_s)$ and $Y_O^-(\Theta_s)$ on oxygen coverage can be seen in the

electron-ion ratio, $Y_e^-(\Theta_s)/Y_O^-(\Theta_s)$, illustrated in Fig. 4.4a. The ratio, initially at 0.35,

increases to 2.3 at an exposure of 2.5 L and remains essentially constant thereafter. As

shown in Fig. 4.4b, the rate of increase of the electron yield with exposure, $dY_e^-(\Theta_s)/d\Theta_s$,

is a maximum at ~ 2 L. Coincidentally, this maximum occurs at approximately the

exposure at which the oxygen-altered work function of a Mo (100) surface is a minimum
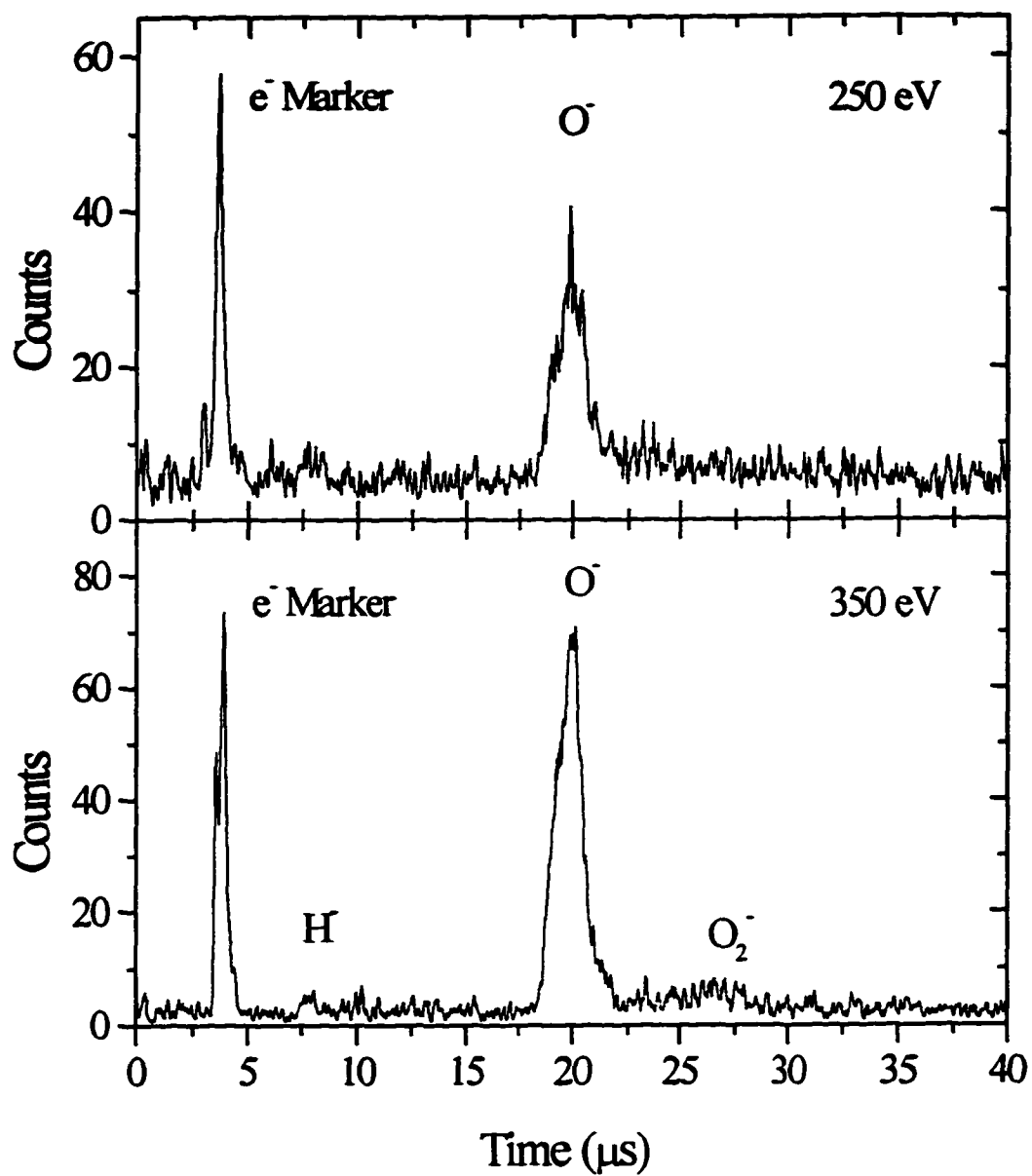
Fig. 4.2 Mass spectrum of sputtered negative ions obtained by TOF mass spectroscopy for Na$^+$ impacting a Mo surface exposed to 6 L of oxygen at an impact energies of (a) 250 eV and (b) 350 eV. The secondary electron signal used to determine the flight time of the negative ions is indicated, and the negative ions (H$^-$, O$^-$ and O$_2^-$) are identified.
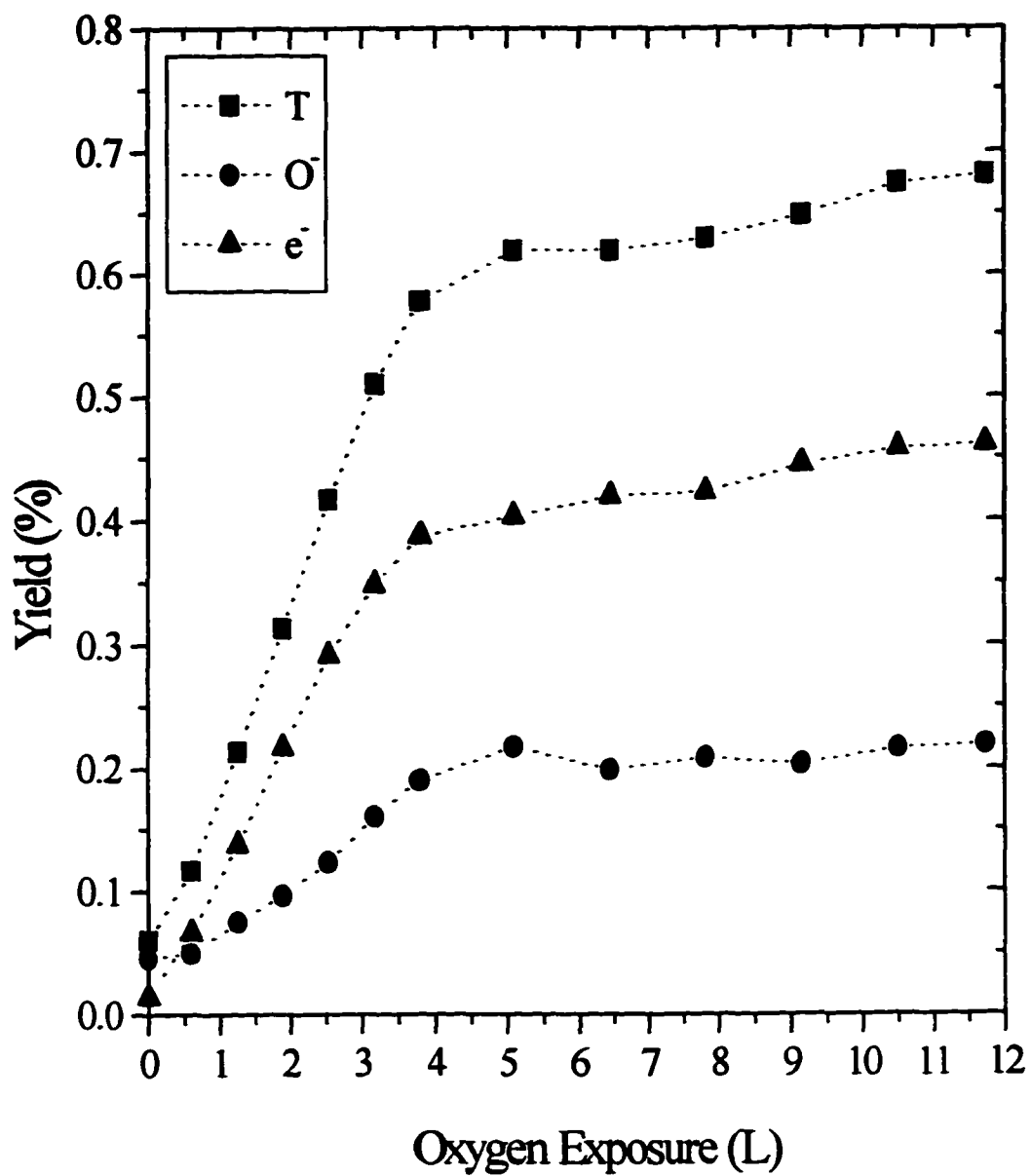
Fig. 4.3 Absolute (■) total, (●) O⁻ and (▲) electron yields as a function of oxygen exposure of the Mo surface at a Na⁺ impact energy of 250 eV.
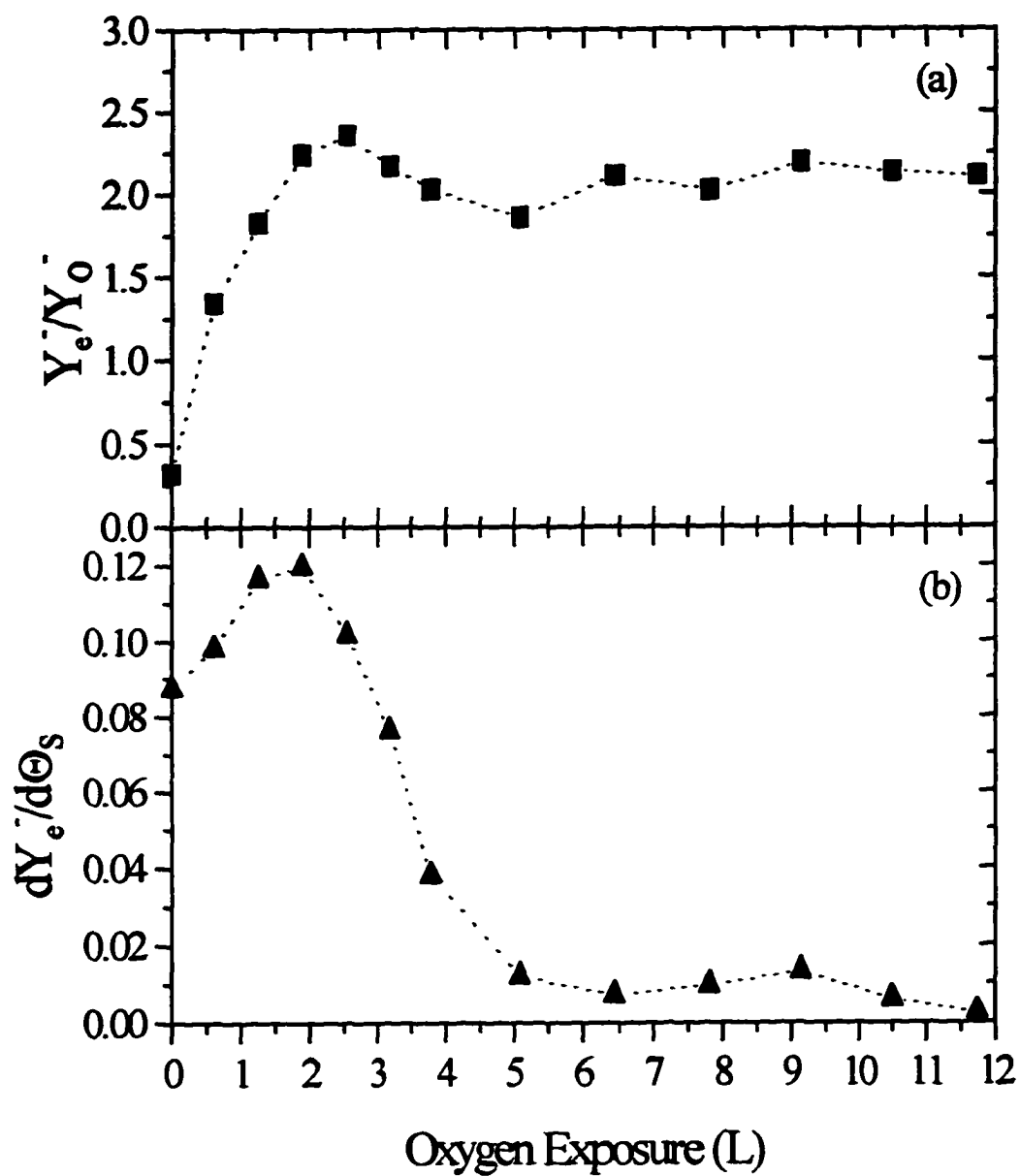
Fig. 4.4 (a) Electron-O⁻ ratio (■), Y_e^-/Y_O^-, and (b) the change in the electron yield (▲), $dY_e^-(\Theta_S)/d\Theta_S$, as a function of oxygen exposure of the Mo surface at a Na⁺ impact energy of 250 eV.

[69]. A similar maximum increase in electron emission, occurring at ~ 2 L, has been reported for 5 - 60 keV Ar^+ bombardment of Mo [8]. Though the results of the two experiments are similar, the electron emission in the latter, high energy experiment is dominated by direct kinetic and potential emission processes which are very improbable sources of secondary electrons in the present experiments.

Due to the apparent correlation between the exposure (~ 2 L) at which $dY_e^-(\Theta_S)/d\Theta_S$ is a maximum and the exposure (~ 1.25 L) where the work function of the Mo (100) surface is minimized [69], an additional test was performed to examine the dependence of Y_e^- on the work function of the Mo surface specific to these experiments. The yields, at an impact energy of 400 eV, were measured first as a function of oxygen exposure and then as a function of Na^+ dose of the surface as shown in Fig. 4.5. As was observed for an impact energy of 250 eV, $Y_e^-(\Theta_S, 400 \text{ eV})$ and $Y_O^-(\Theta_S, 400 \text{ eV})$ exhibit a different dependence on oxygen coverage. As seen in Fig. 4.5b, accumulated Na on the surface leads to a large increase in $Y_O^-(14.1 \text{ L}, 400 \text{ eV})$ owing to the fact that Na on the surface lowers the work function, increasing the survival probability for the negative ion to survive into the vacuum. The electron yield also increases due to accumulated Na, however, the electron-ion ratio decreases as seen in Fig. 4.5d. Even though the electron yield is observed to increase as Na lowers the work function and $dY_e^-(\Theta_S)/d\Theta_S$ is a maximum at approximately the work function minimum (Fig. 4.6), $Y_e^-(\Theta_S, 400 \text{ eV})$ still continues to increase as the work function increases for oxygen exposures > 2 L. Thus, the increase in secondary electron emission due to oxygen coverage of the surface cannot be attributed solely to an oxygen-altered work function. A similar conclusion was reached
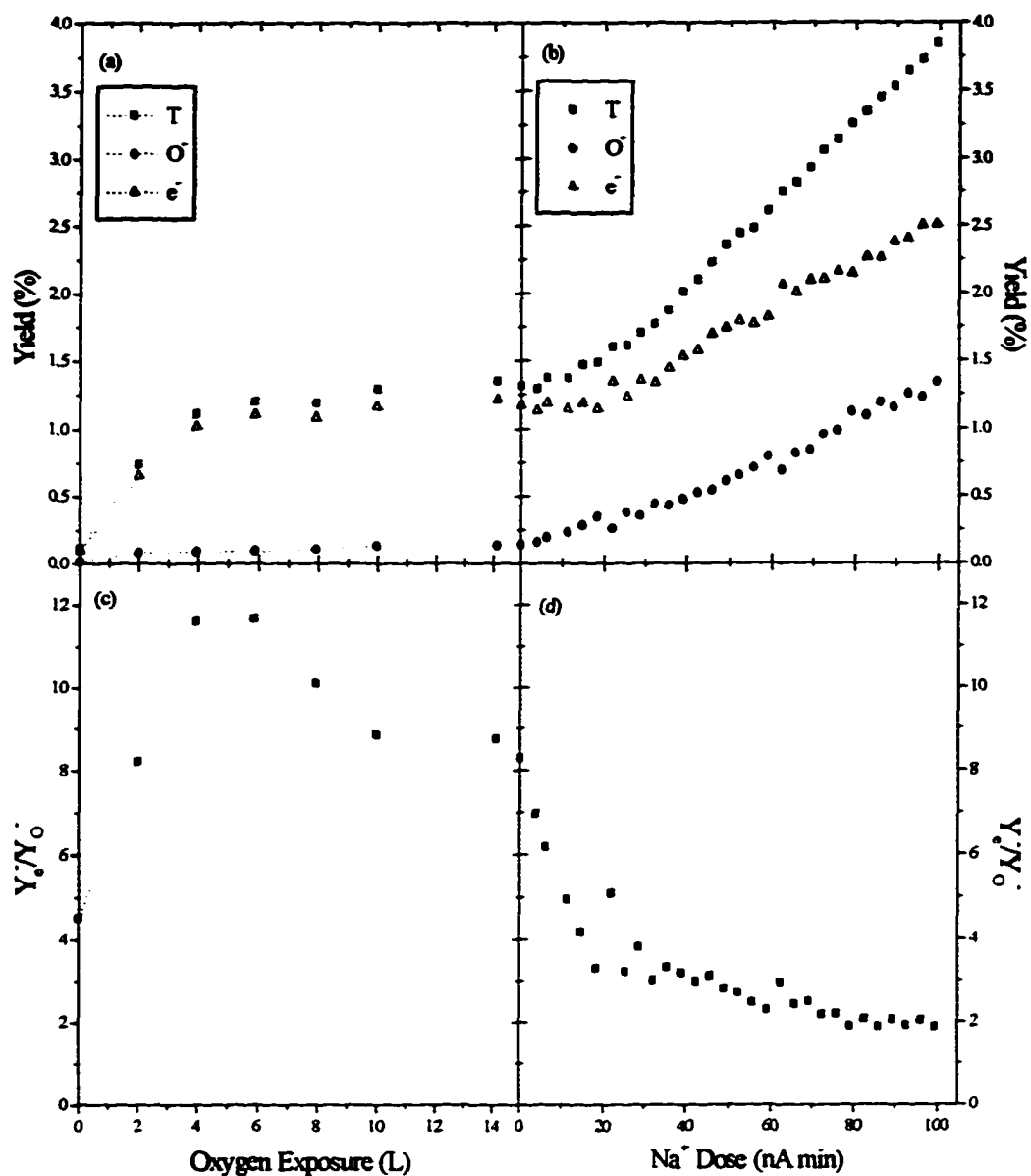
Fig 4.5 (a) Absolute (■) total, (●) O⁻ and (▲) electron yields as a function of oxygen exposure of the Mo surface at a Na⁺ impact energy of 400 eV. (b) Absolute (■) total, (●) O⁻ and (▲) electron yields as a function of Na⁺ dose of the Mo surface (following the 14.1 L oxygen exposure) at a Na⁺ impact energy of 400 eV. The electron-O⁻ ratio (■), Y_e^-/Y_O^-, as a function of (c) oxygen exposure and (d) Na⁺ dose of the Mo surface at a Na⁺ impact energy of 400 eV.

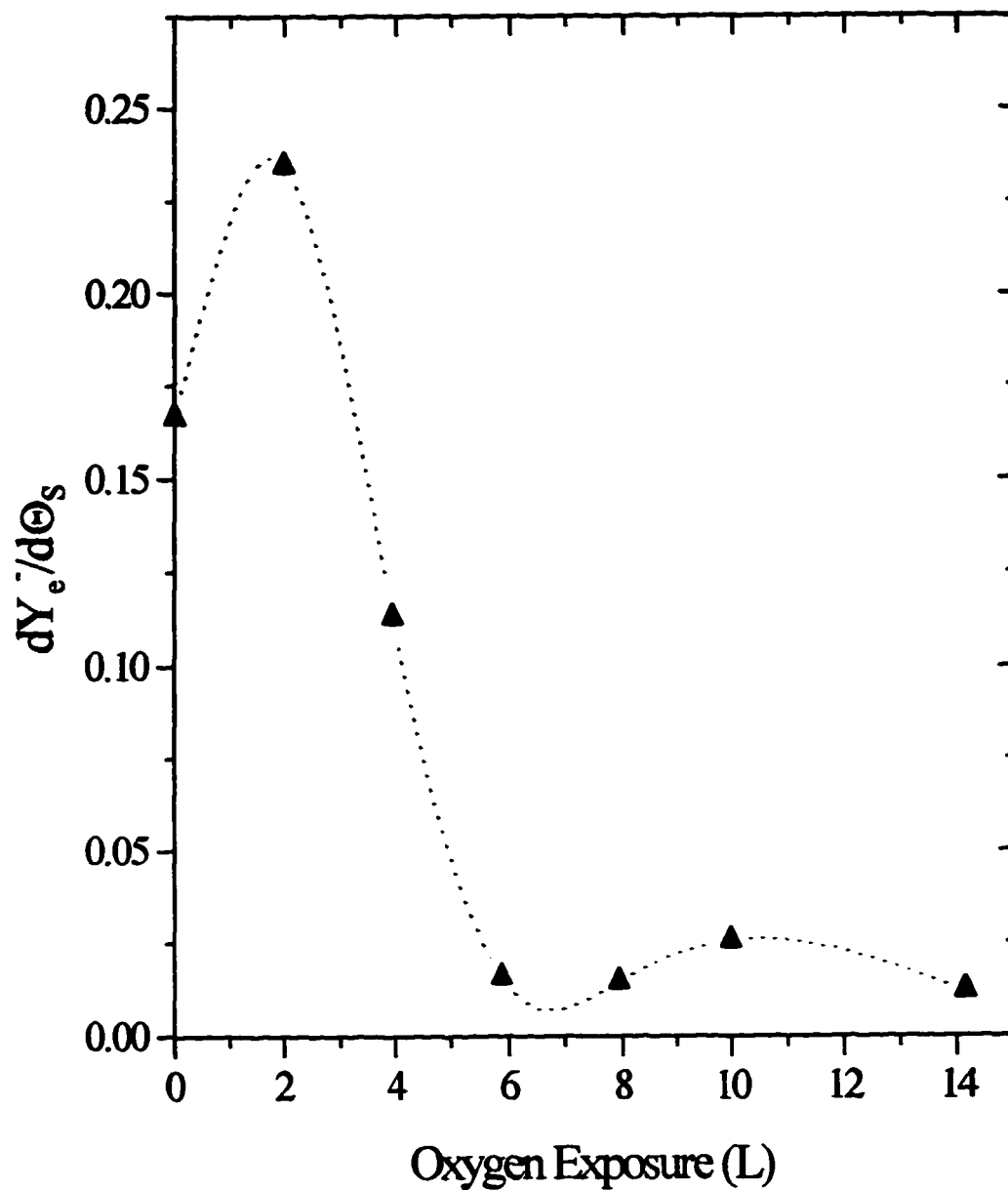**Fig. 4.6** Change in the electron yield, $dY_e^-(\Theta_S)/d\Theta_S$, as a function of oxygen exposure of the Mo surface at a Na^+ impact energy of 400 eV.

for direct kinetic and potential electron emission in the aforementioned experiments of Ar^+

collisions with an oxygen covered Mo surface [8].

4.1.1.3 Comparison of Oxidized and Oxygen Covered Surfaces

The yield results and the mass distribution of sputtered negative ions for a Mo

surface with up to a few monolayers of oxygen coverage are somewhat different than the

results of Baker, et al. [7] for an oxygen-saturated Mo surface. In those experiments,

where sputter-cleaning was not available, there was a significant amount of carbon

contamination of the surface, evidenced by the sputtering of C^- and C_2^-, and the O_2^- yield

was found to exceed that for O^- at low impact energies. They also observed that the

relative contribution of O_2^- to the total negative ion yield decreased with increasing impact

energy. This is a significant difference since they suggested that the source of the

secondary electrons may have been sputtered, unstable O_2^- ions. They proposed that in

the sputtering process, both stable and unstable O_2^- are formed which exit the surface.

$O_2^-(v)$ is stable for the three lowest vibrational states in the molecular ion's lowest

electronic state. $O_2^-(v)$ becomes unstable for vibrational quantum numbers, $v > 3$, and will

autodetach, giving a free electron. They reasoned that the collisional excitation of O_2^-

(i.e., the average vibrational quantum number, $\bar{v}$, for $O_2^-(\bar{v})$) would increase accordingly

with impact energy. Thus, in the near threshold region, $\bar{v}$ is likely to be less than 3, leading

to a large O_2^- yield relative to the electron yield. While at higher collision energies,

$O_2^-(\bar{v} > 3)$ is more likely to be formed, and as a result, the electron yield would exceed the

ion yield as was observed. In contrast, in the present experiments, the contribution of

sputtered O_2^- to the total negative ion yield is negligible at all impact energies and oxygen coverages from none up to a few monolayers. Hence, the sputtering of unstable $O_2^-(v)$, which subsequently autodetaches giving a free electron, is not a likely source of the secondary electrons observed here. In the aforementioned experiment, there was no way to remove oxygen from the surface, and repeated annealings to 1000 K may have lead to significant heavy oxide growth on the Mo surface from which sputtered O_2^- and secondary electrons were observed.

4.1.1.4 Kinetic Energy Distributions

Normalized kinetic energy distributions for O^- sputtered from a Mo surface exposed to ~ 10 L of oxygen are shown in Fig. 4.7 for Na^+ impact energies of 150 eV, 250 eV and 350 eV. The distributions have been normalized with respect to the low energy peak such that the leading edges of the distributions are aligned, setting the zero of the energy scale. All the distributions have a sharp peak at ~ 2.25 eV and a significant, low level, high energy tail. The shapes of the distributions are, for the most part, independent of impact energy, and the distributions for smaller exposures vary only in intensity of the sputtered O^-. The corresponding normalized secondary electron kinetic energy distributions for the previous conditions are shown in Fig. 4.8. The electron distributions are sharp, having FWHM from 1.75 eV to 2.25 eV, and they all peak at an energy of ~ 1.6 eV, slightly less than the most probable O^- kinetic energy. Again, the distributions are essentially invariant with impact energy, and the amount of the oxygen exposure affects only the intensity of the distributions. This independence of both oxygen

Fig. 4.7 Normalized sputtered O⁻ kinetic energy distributions for a 10 L oxygen exposed Mo surface at Na⁺ impact energies of (■) 150 eV, (○) 250 eV and (▲) 350 eV.
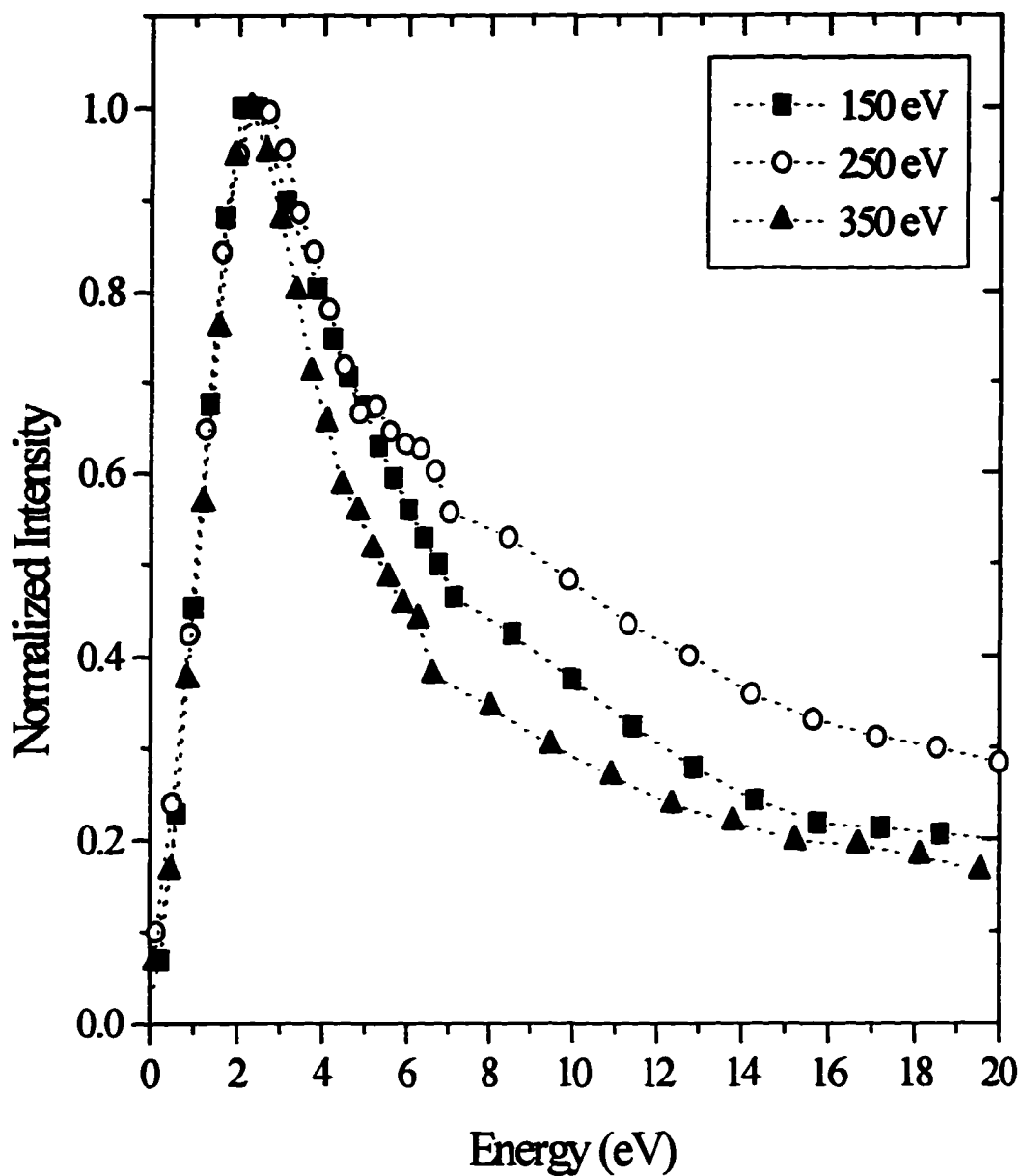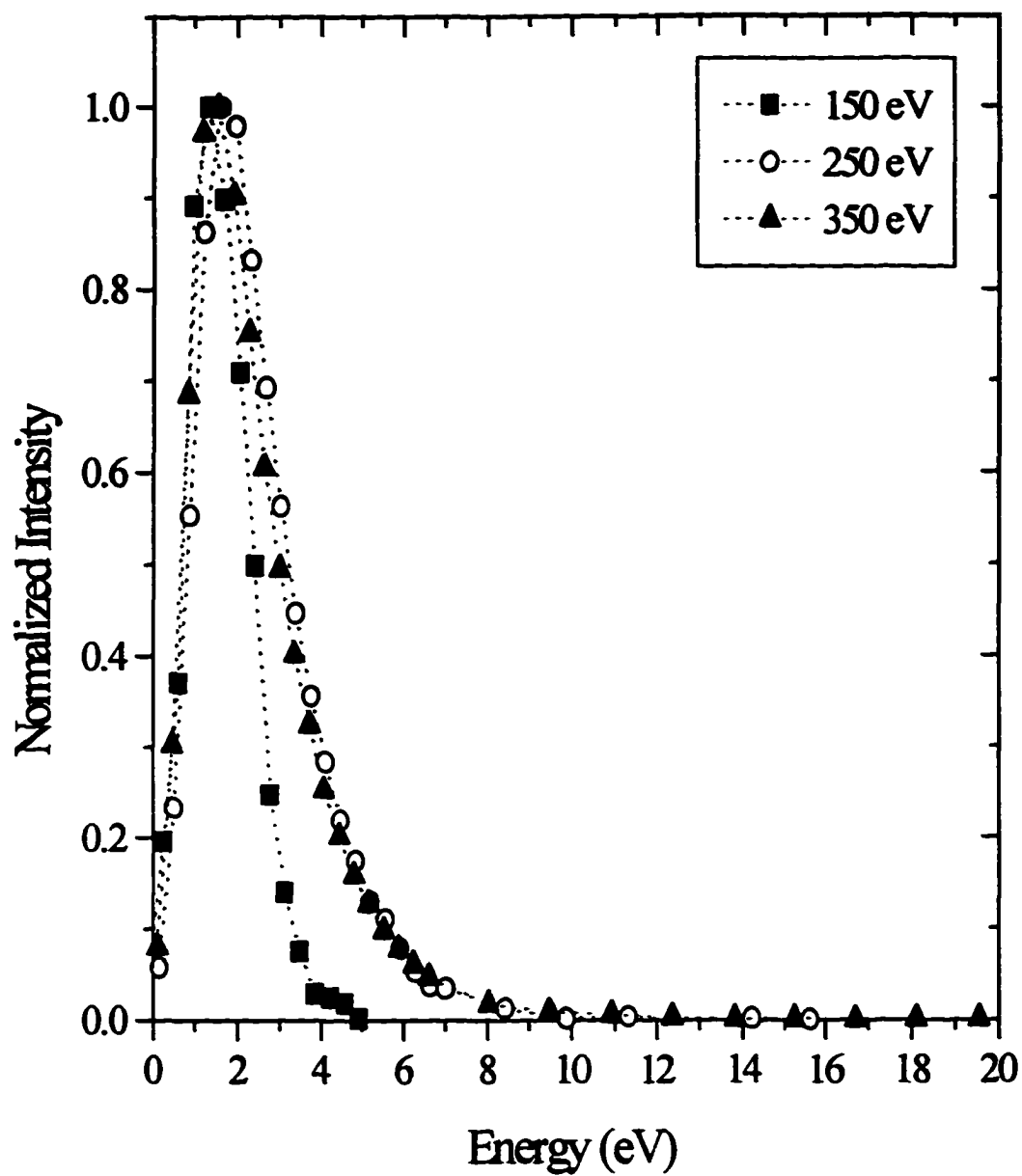
Fig. 4.8 Normalized secondary electron kinetic energy distributions for a 10 L oxygen exposed Mo surface at Na^+ impact energies of (■) 150 eV, (○) 250 eV and (▲) 350 eV. Note the absence of energetic electrons, compared to the energetic ions observed in Fig. 4.7.

coverage and impact energy was also observed in the energy distributions for an Al surface, and the general shapes of the distributions for the two surfaces are similar. However, the distributions (both electron and ion) associated with the Mo surface do peak at slightly higher kinetic energies, and the tail of high energy O^- ions is slightly more pronounced for the Mo surface.

4.2 Molybdenum (100)

The Mo (100) surface provides for better surface characterization in these emission experiments since the ordered structure of the single crystal gives both the arrangement of the Mo atoms in the surface layer and possible oxygen adsorption sites on the surface. Experiments on Mo (100) also enable a comparison of the emission from an ordered, well characterized surface and that from a disordered surface with many crystal planes, grain boundaries, etc. Molybdenum's common crystal phase is a body centered cubic (bcc) with a lattice constant of 3.15 Å at room temperature. The surface unit cell of the Mo (100) surface has a surface layer (S) of Mo atoms, evenly spaced 3.15 Å apart as shown in Fig. 5.9. The subsurface layer (S - 1) lies 1.57 Å below the surface layer with a Mo atom centered between the four atoms of the surface layer, and the third layer (S - 2) lies directly beneath the first representing an ABA... form of stacking. The Mo (100) single crystal sample used in the experiments has been polished to orientation of 0.5° [56].
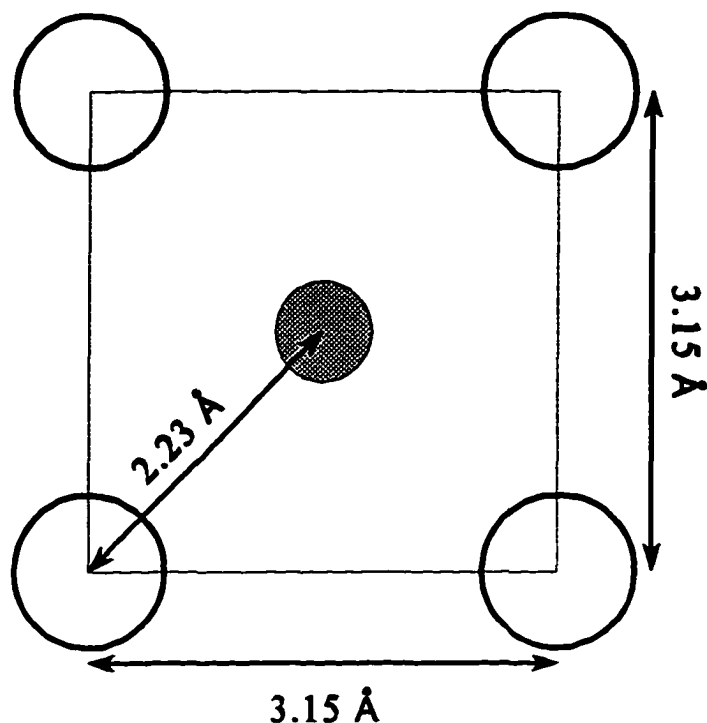
Fig. 4.9 Geometrical arrangement of the atoms for the surface unit cell Mo (100) surface (bcc lattice). The large circles represent Mo atoms in the surface layer (S), and the small grey circles are atoms in the second layer (S - 1). Atoms in the third layer (S - 2) lie directly beneath those in the surface layer. The separation between layers is 1.57 Å.

4.2.1 Oxygen Adsorption on Molybdenum (100)

The oxygen uptake of the Mo (100) surface is roughly an order of magnitude faster than for Al. AES studies of O adsorption on Mo (100) show [69]: (1) a linear uptake of oxygen for exposures up to ~ 1 L; (2) the O uptake begins to saturate at an exposure of ~ 3.5 L; and (3) complete saturation of the surface occurs at exposures above 10 L. The results of an AES study of oxygen adsorption on the Mo (100) surface specific to these experiments are in good agreement with those of Riwan, et al. [69] as

shown in Fig. 4.10a. Accumulated oxygen, alters the work function of the Mo (100) surface, where the change in the work function is dependent on the exposure. As seen in Fig. 4.10b, ϕ initially decreases with exposure, reaching a minimum at 1.25 L, and for exposures above 2 L, ϕ increases to 1.5 eV above that for a clean surface (clean Mo (100), ϕ = 4.53 eV).

Low Energy Electron Diffraction (LEED) studies of oxygen adsorption on Mo (100) show basically three phases of room temperature adsorption [69]. For low exposures, the growth of a c(2x2) O structure is observed which has a maximum intensity at ~ 1 L ($\Theta_S \approx 0.5$) implying that O_2 dissociates on the surface. The decrease in ϕ, for exposures up to 1.25 L, is ascribed to the incorporation of O atoms into the surface layer. For exposures between 1 and 3.5 L, a pattern consistent with the growth of two-dimensional Mo (110) p (2x2) O microfacets are observed. The increase in ϕ in this range of exposure is attributed to the higher work function of the Mo (110) surface, 5.11 eV. Finally, above 4 L, the surface flattens again, suggesting the growth of surface oxides.

A more recent Scanning Tunneling Microscopy (STM) investigation [70] observed the growth of surface Mo_4O_4 clusters at low exposures as shown in Fig. 4.11a. At higher exposures, an oxygen-induced (2x1) structure on the Mo (100) surface was observed as illustrated in Fig. 4.11b. The O atoms are assumed to arrange along either side of a row of Mo atoms, and due to charge transfer between the O and Mo atoms (i.e. O sits on the surface as O^-), there is a missing row of Mo atoms between two neighboring rows of Mo atoms. In this study, the initial lowering of ϕ is attributed to the lower work function of the Mo_4O_4 clusters, whereas at higher exposures, the increase in ϕ is attributed to the
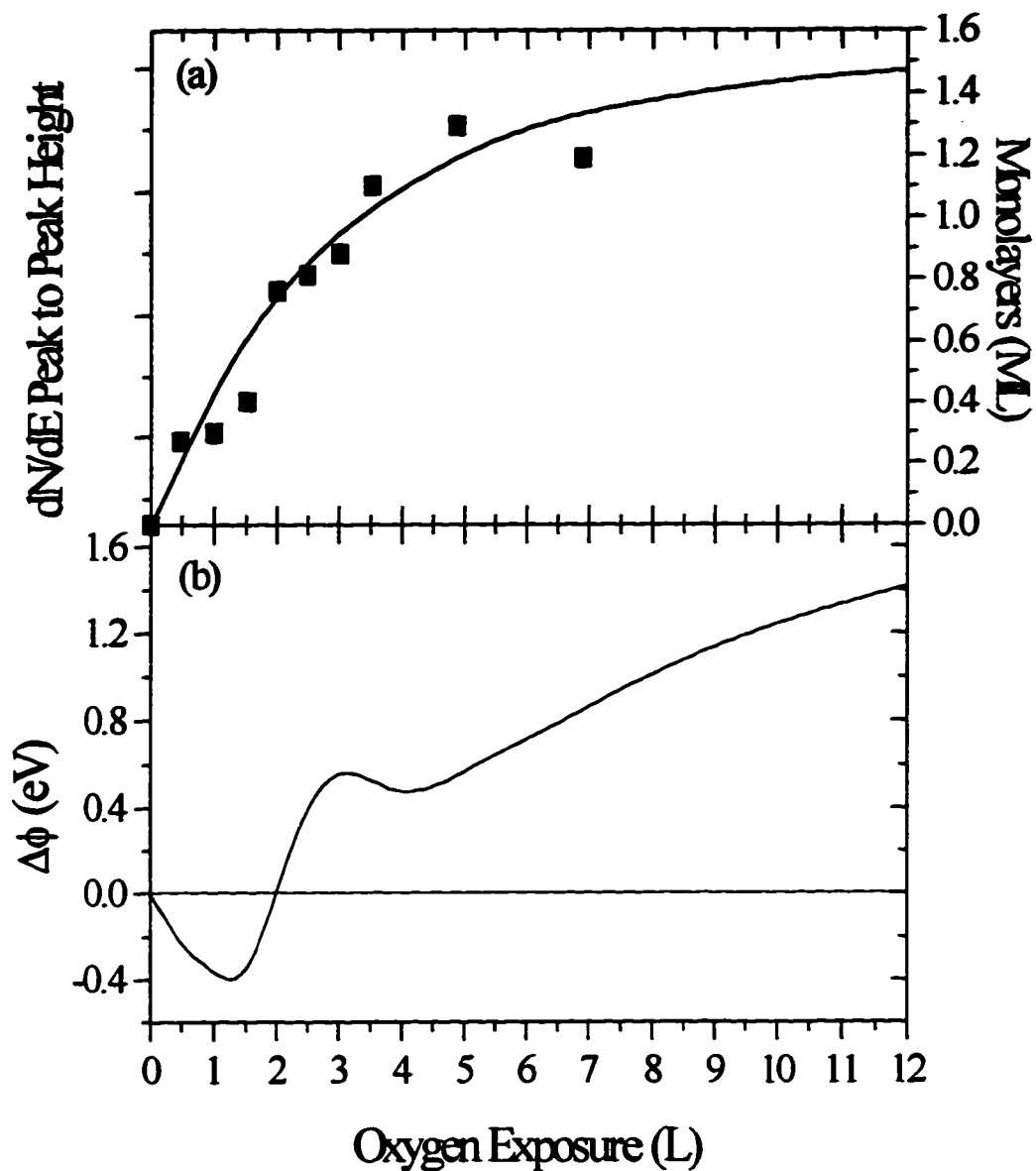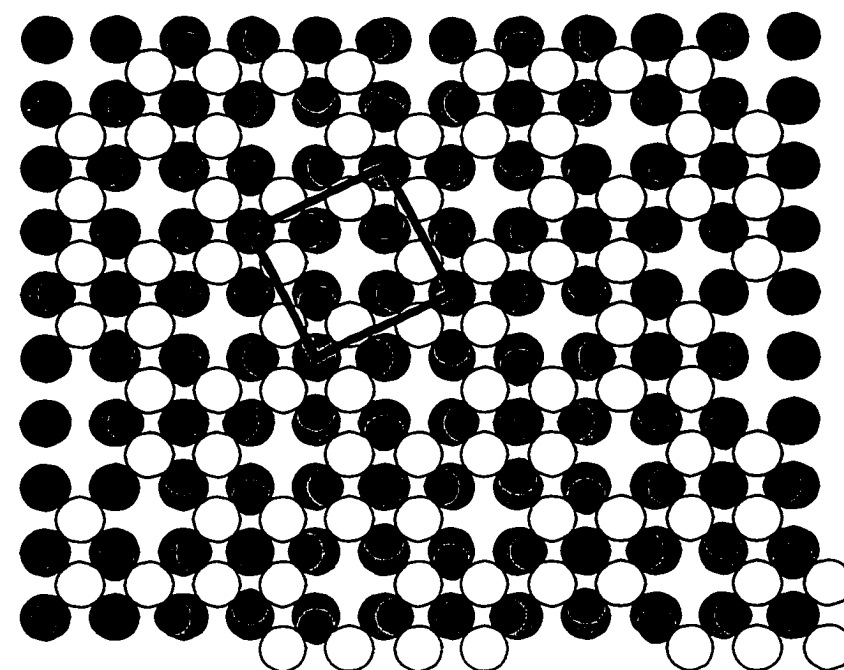
Fig. 4.10 (a) Oxygen (■) AES peak height as a function of oxygen exposure of the Mo (100) surface. The solid line and the right hand scale are the results of Riwan, et al. in Ref. [68]. (b) Change in the work function of the Mo (100) surface as a function of oxygen exposure from Ref. [69].

(a) (√5x√5) Structure on Mo(100)

(b) (2x1) Structure on Mo(100).
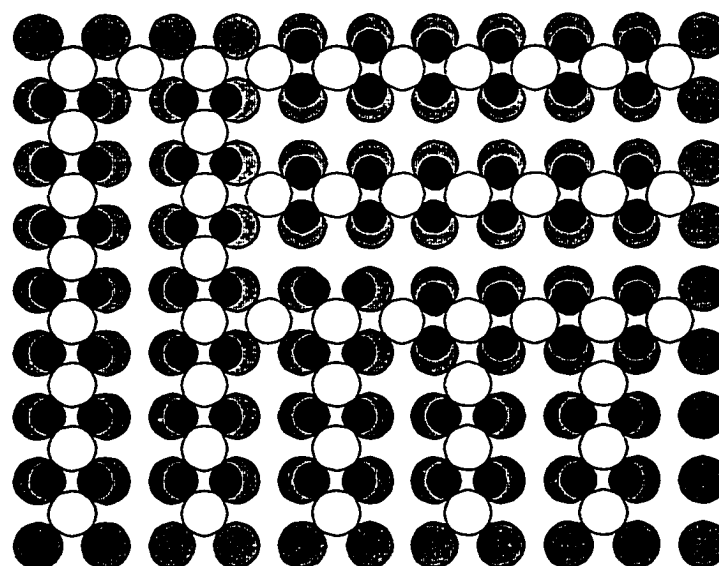
● Oxygen   ○ S layer Mo   ◕ S-1 layer Mo

Fig. 4.11 (a) Structural model of (√5x√5) O structure on Mo (100). The square represents the surface unit cell. (b) (2x1) O structure on Mo (100) with the "missing row" feature. These models are taken from Xu and Simon Ng in Ref. [70].

formation of a surface dipole moment owing to the charge transfer between O and Mo atoms. Though the results of these two experiments may differ on the exact modification of the surface due to oxygen exposure, they do provide several insights on the O/Mo (100) system. First, molecular oxygen dissociates on a Mo (100) surface as it adsorbs. Second, adsorbed O resides essentially as O⁻ on a Mo (100) surface. Third, clearly there are at least two different, exposure dependent structures which form on the Mo (100) surface which have significantly different effects on the work function.

As previously mentioned, AES was available for the analysis of the Mo (100) surface and was used to verify that the surface was free of contaminants following the cleaning procedure. The same extraction/analysis system used to analyze the secondary electrons and sputtered negative ions was used to analyze the Auger electrons, and 3 keV AES spectra for an oxygen covered surface and a clean surface (after a sputter/heat/ sputter cycle) are shown in Fig. 4.12. The 186 eV and 221 eV Mo Auger signals are easily identifiable on the secondary electron distribution, and the inset shows the 509 eV O signals of the clean and oxygen covered surfaces. The overall shape of the spectrum simply reflects the transmission efficiency of the extraction system and the EEA at high kinetic energies. In practice and as a time saving technique, it was usually only necessary to monitor the O AES signal (rather than the full spectrum) after several cycles of cleaning the surface to ensure that all of the oxygen had been removed from the surface following repeated exposure experiments.

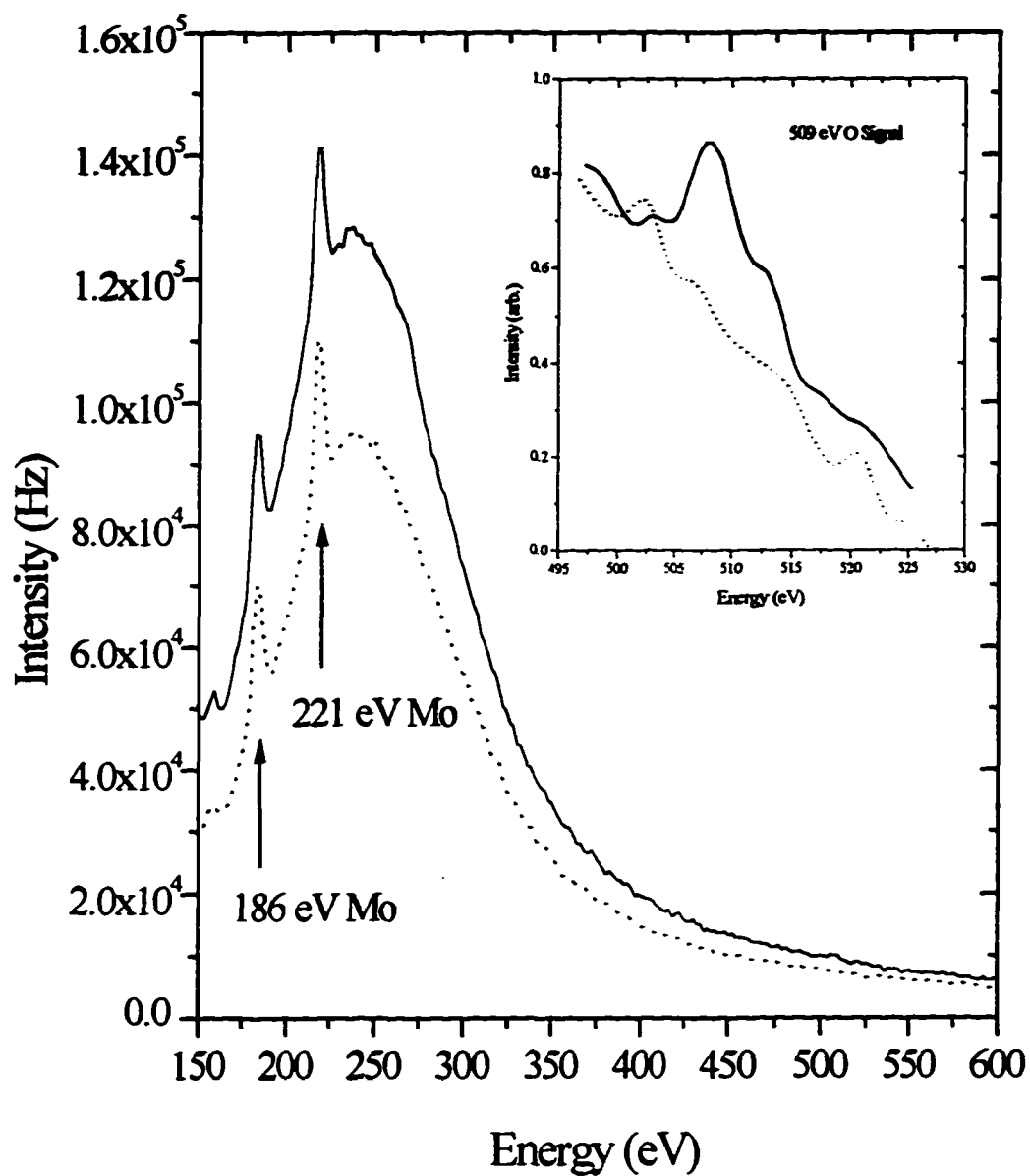**Fig. 4.12** Raw AES spectra (E_p = 3 keV) for (·····) clean and (——) oxygen exposed Mo (100) surfaces. The overall shape of the secondary electron distribution is simply a function of the detection efficiency of the extraction system at high kinetic energies. The Mo Auger peaks at 186 eV and 221 eV are easily identified. The inset shows the O Auger peak 509 eV for the surface before and after cleaning.

4.2.2 Molybdenum (100) - Results

4.2.2.1 Yields

As was the case with polycrystalline Mo, the negative ions were identified by TOF mass spectroscopy. Three TOF spectra for a moderate oxygen exposure of ~ 3 L at impact energies of 150 eV, 250 eV and 350 eV are shown in Fig. 4.13. The negative ions observed in these spectra are O^-, H^-, O_2^- and Na^-, however O^- still dominates the yield of negative ions, and thus, $Y_X^- \approx Y_O^-$ again. These TOF spectra were obtained *after* measurements of the ion and electron kinetic energy distributions, and it should be noted that some sputtered Na^- (~ 24 μs) is observed at an impact energy of 450 eV. The sputtering of Na^- arises from Na which accumulates on the surface during the energy distribution measurements, and thus care was taken to limit the total Na^+ dose of the surface during the measurements. Determining the TOF mass spectra after the energy distribution runs verified that the contribution of sputtered Na^- to the total negative ion yield was negligible. SIMS TOF spectra of the surface, prior to lengthy exposures to the Na^+ beam, show no evidence of sputtered Na^- from the surface. As for the previous studies of the polycrystalline surfaces, O^- was also the dominant negative ion observed at all other impact energies and oxygen exposures.

The secondary electron and oxygen negative ion yields for a Mo (100) surface exposed to ~ 3 L of oxygen are shown as a function impact energy in Fig. 4.14. Both yields share an impact energy threshold at 50 eV, and both are observed to increase with impact energy up to 300 eV. Y_O^-(3 L) exceeds Y_e^-(3 L) for impact energies below 200 eV, however Y_e^- is rapidly increasing with impact energy, dominating the negative emission at
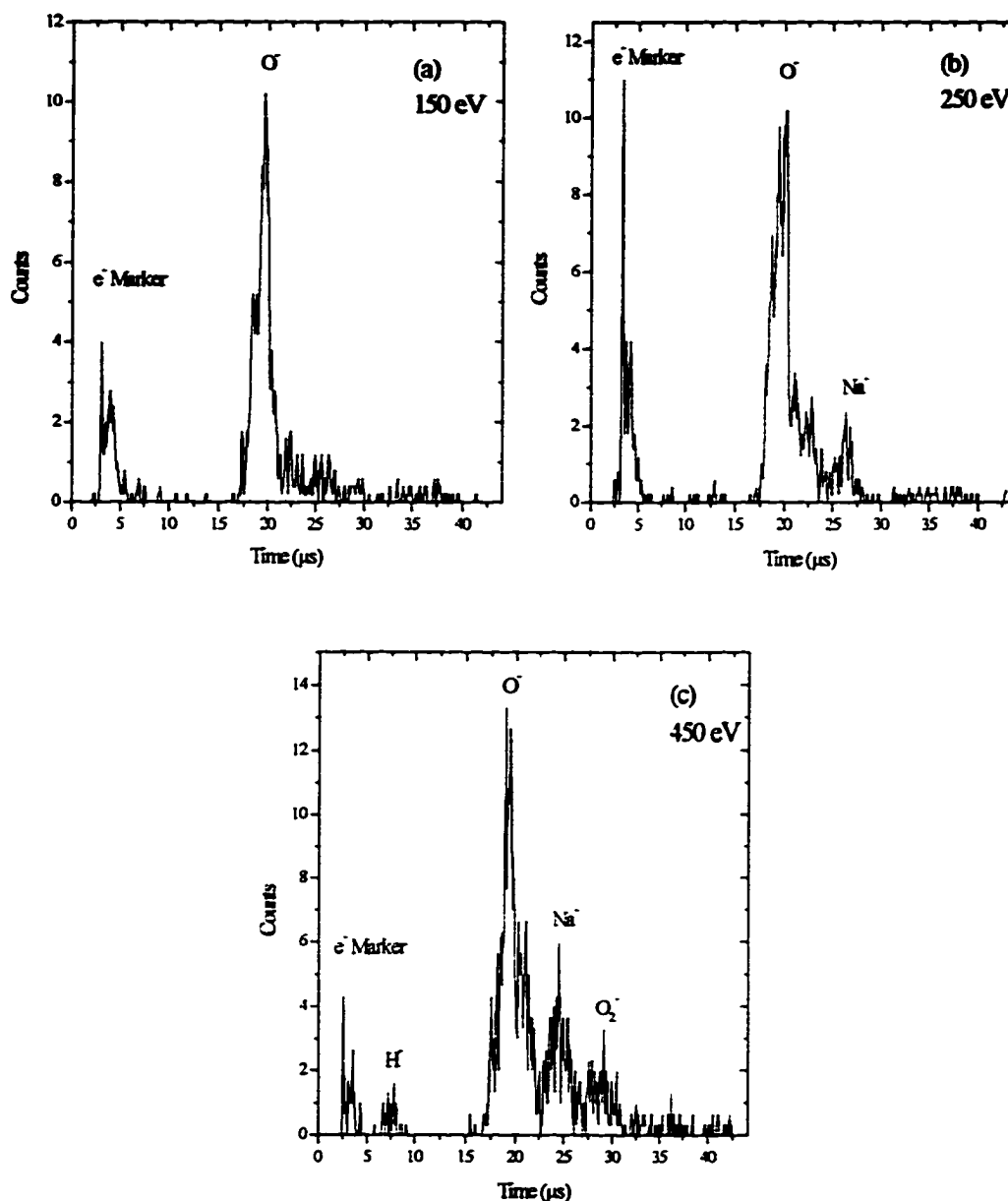
Fig. 4.13 TOF mass spectra of the negative ions for a Mo (100) surface exposed to ~ 3 L of oxygen for impact energies of (a) 150 eV, (b) 250 eV and (c) 450 eV. In each case, the electron signal is at ~ 4 µs and the dominant negative ion observed is O⁻, at a flight time of ~ 16 µs relative to the electron signal (i.e., at a total flight time of ~ 20 µs). The minority species observed, primarily at higher impact energies, include H⁻ (7.5 µs), Na⁻ (25 µs) and O_2^- (28 µs). The slight shift in the peak positions in the TOF spectra to shorter times is due to the shorter time of flight of the Na⁺ ions to the surface at higher impact energies.

Fig. 4.14 Absolute (■) total, (●) O⁻ and (△) secondary electron yields as a function of impact energy for a Mo (100) surface exposed to ~ 3 L of oxygen.
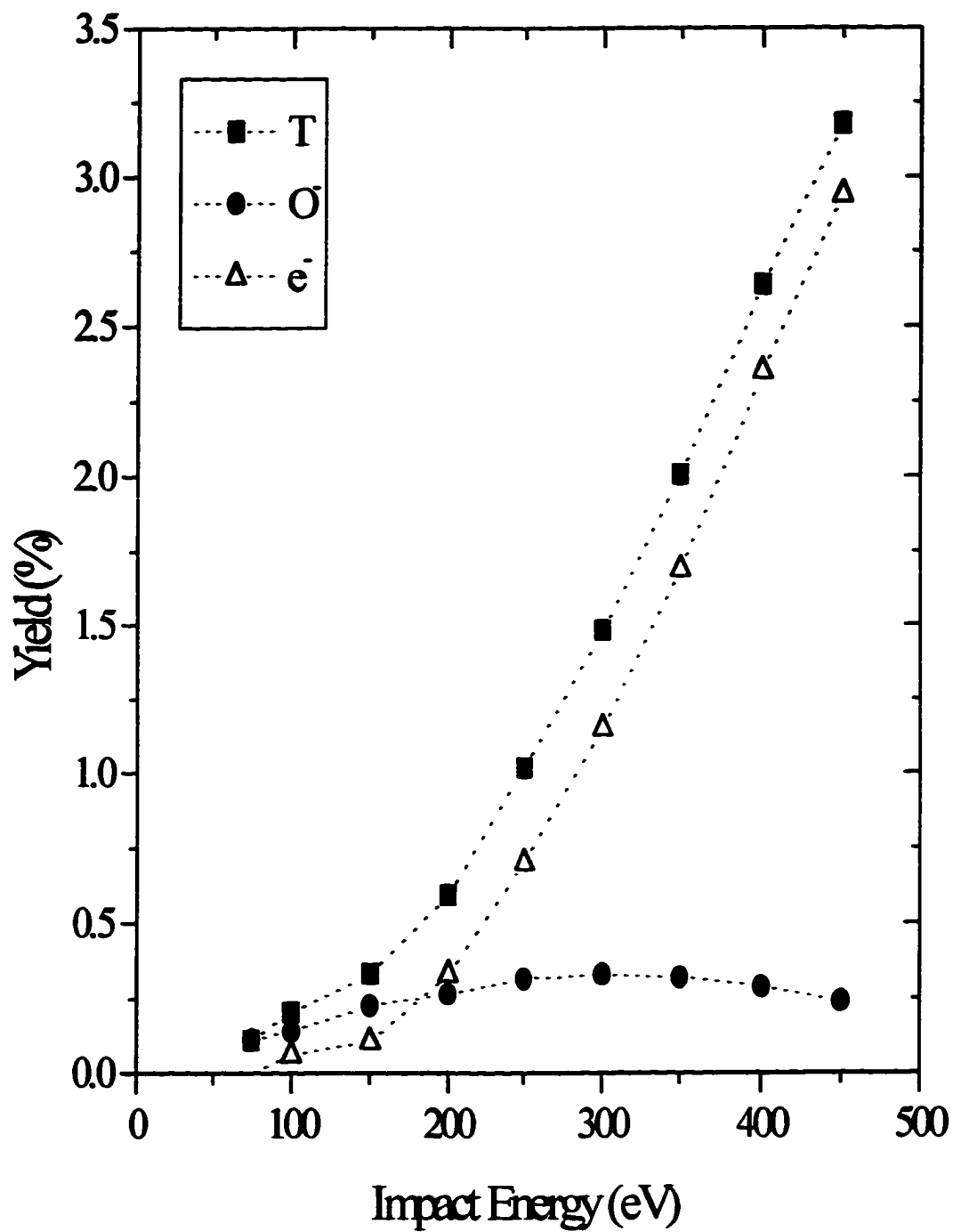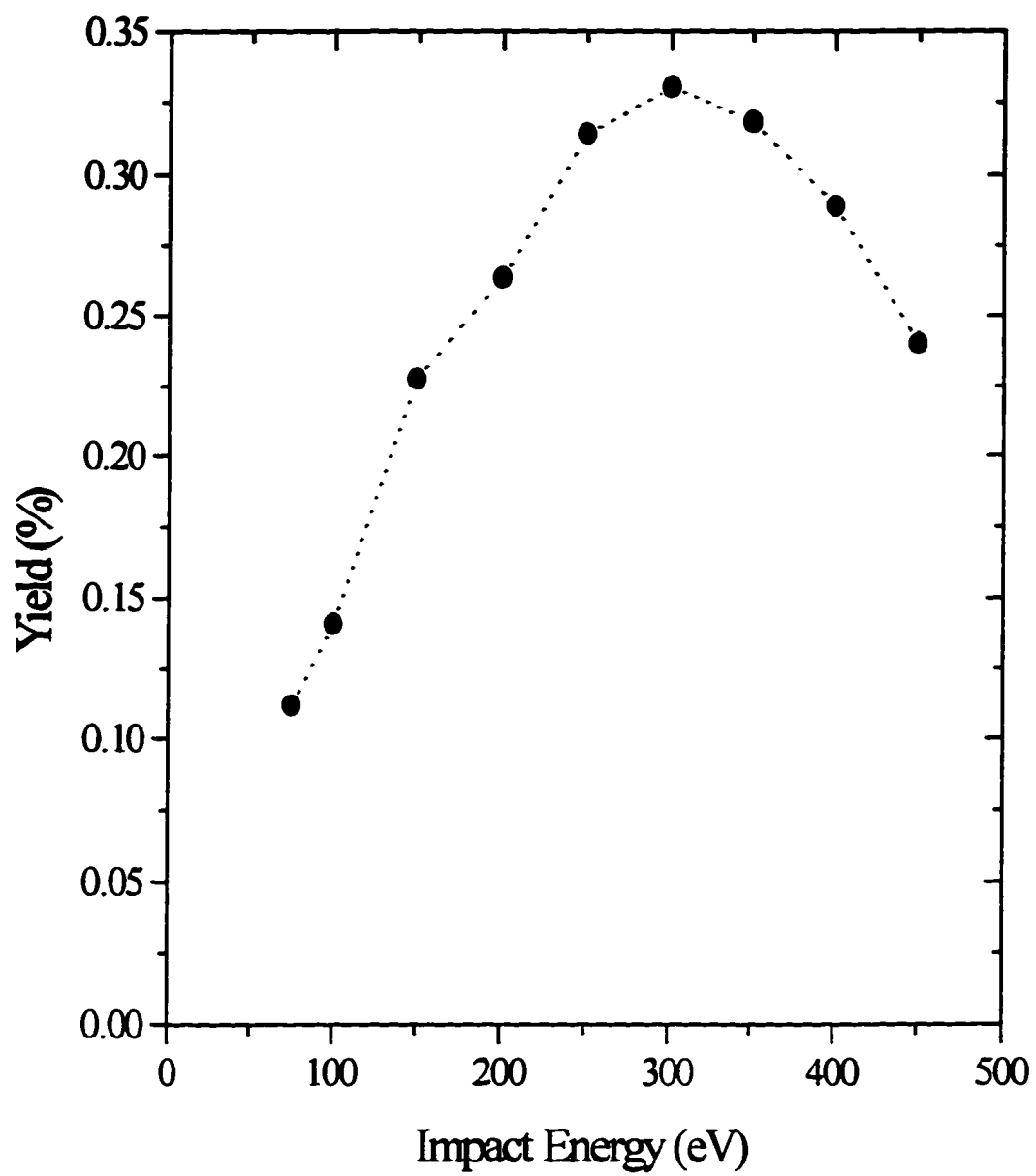
Fig. 4.15 Absolute O⁻ yield as a function of impact energy for a Mo (100) surface exposed to ~ 3 L of oxygen.

the highest impact energies. Even though $Y_O^-(3\ L)$ actually begins to decrease for impact energies above 300 eV as seen in Fig. 4.15, the total yield continues to increase linearly. The oxygen coverage dependence of the yields is shown in Figs. 4.16 and 4.18 where the yields are shown as functions of oxygen exposure for impact energies of 250 and 450 eV respectively. An approximately linear increase in $Y_e^-(\Theta_s)$ is observed for exposures up to 3 - 4 L where the rate of increase of $Y_e^-(\Theta_s)$ and $Y_O^-(\Theta_s)$ decreases, and the yields themselves begin to approach saturation values. Similar to Al and Mo, adsorbed oxygen has a greater effect on secondary electron emission as seen in the electron-ion ratios, Y_e^- $(\Theta_s)/Y_O^-(\Theta_s)$, in Figs. 4.17a and 4.19a. Finally, similar to the results for polycrystalline Mo, the maxima in $dY_e^-(\Theta_s)/d\Theta_s$ occur at ~ 1.75 L as shown in Figs. 4.17b and 4.19b.

Fig. 4.16 Absolute (●) O⁻ and (△) secondary electron yields as a function of oxygen exposure of a Mo (100) surface at an impact energy of 250 eV.

Fig. 4.17 (a) Electron-ion ratio ($\blacksquare$), Y_e^-/Y_O^- and (b) the change in the electron yield ($\blacktriangle$), $dY_e^-(\Theta_S)/d\Theta_S$, as a function of oxygen exposure of the Mo (100) surface at an impact energy of 250 eV.

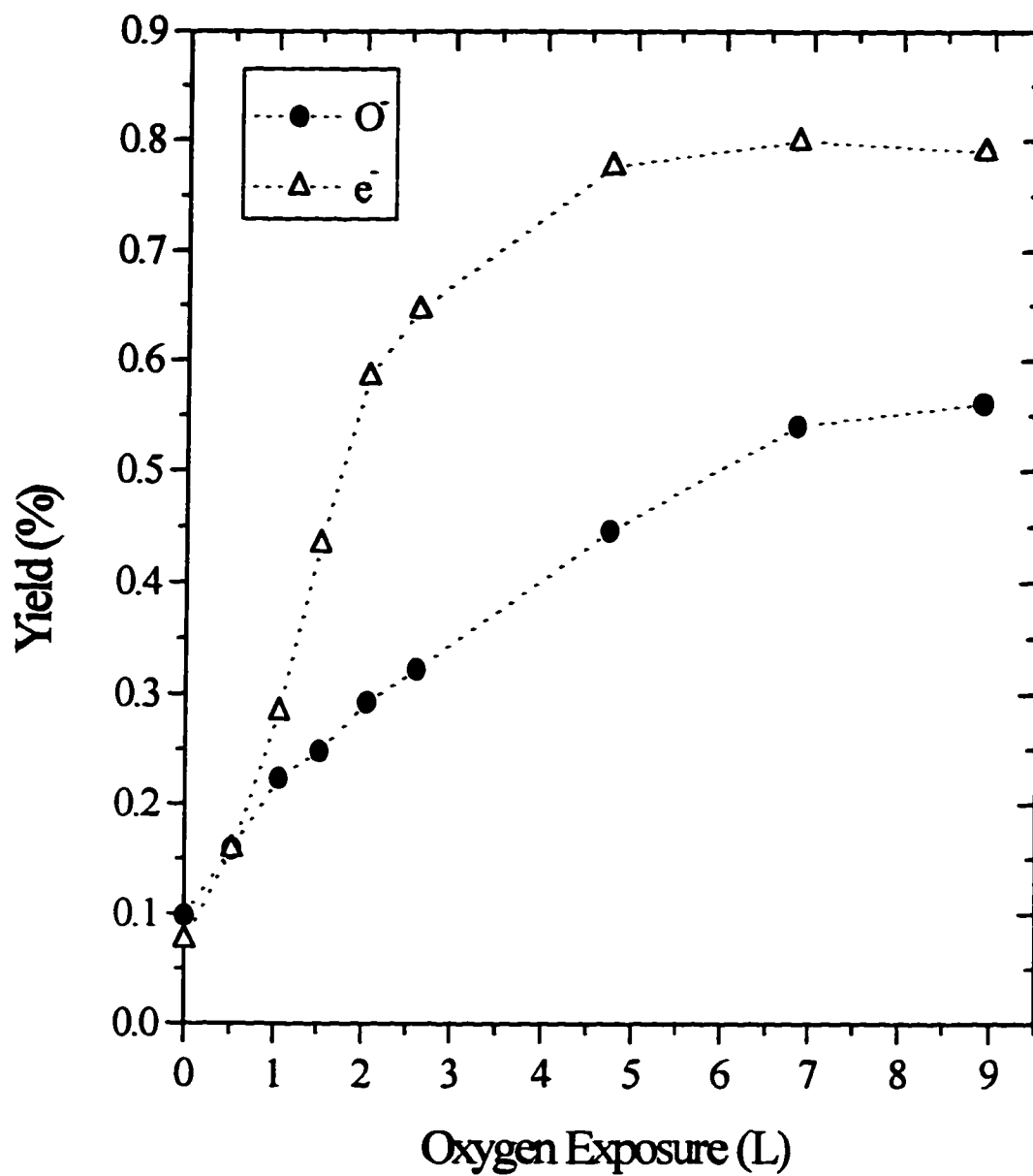**Fig. 4.18** Absolute (•) O⁻ and (▵) secondary electron yields as a function of oxygen exposure of a Mo (100) surface at an impact energy of 400 eV.

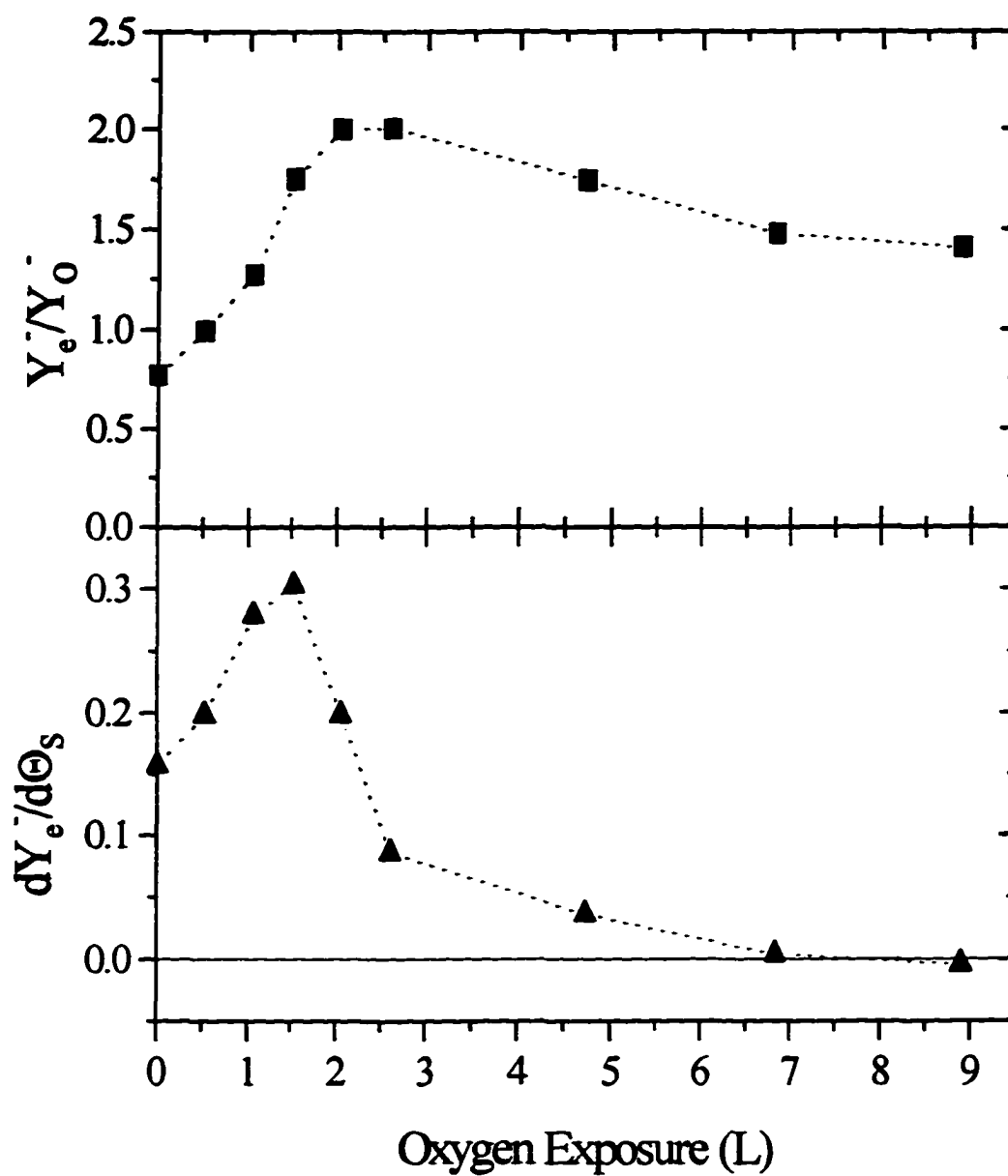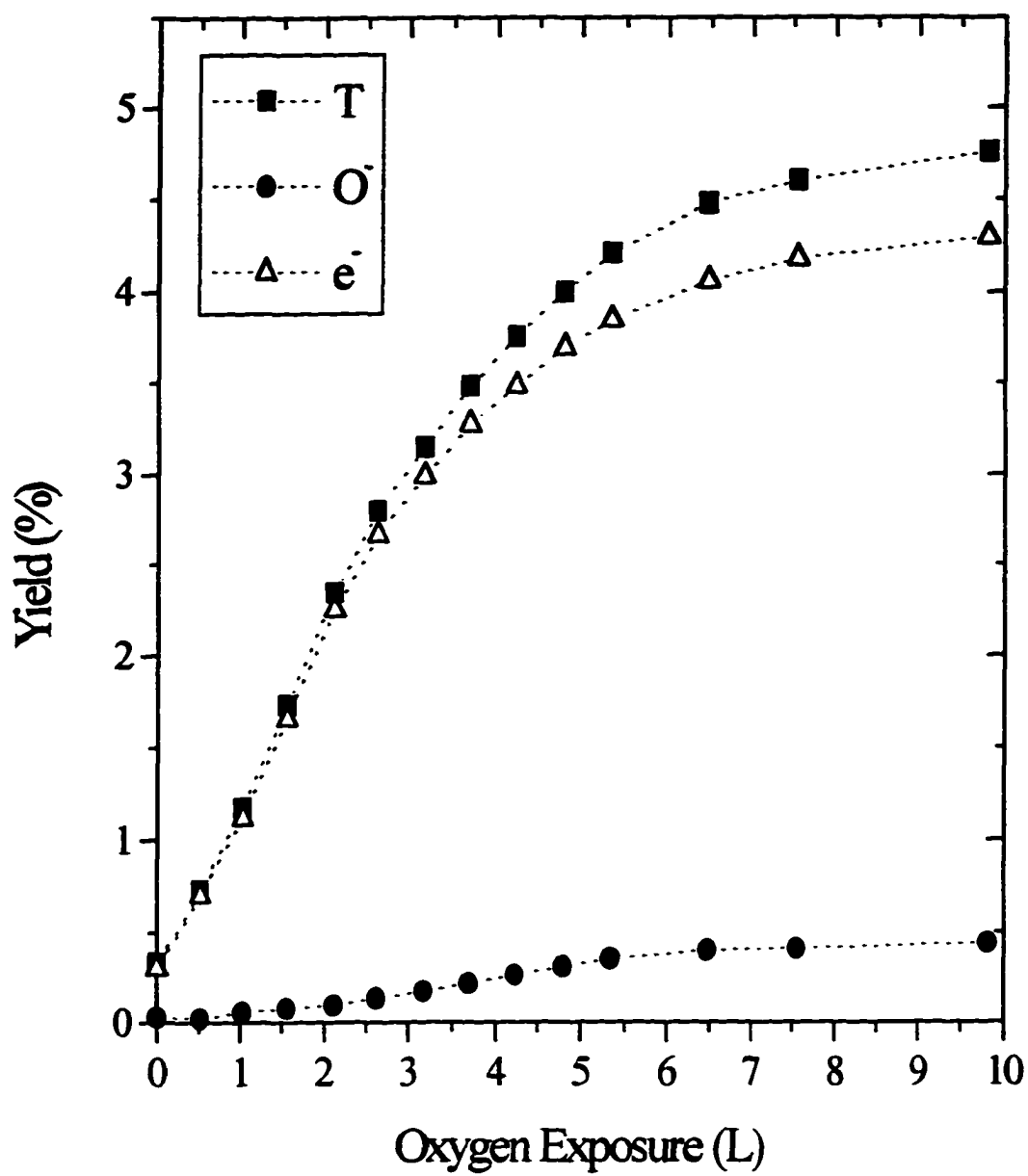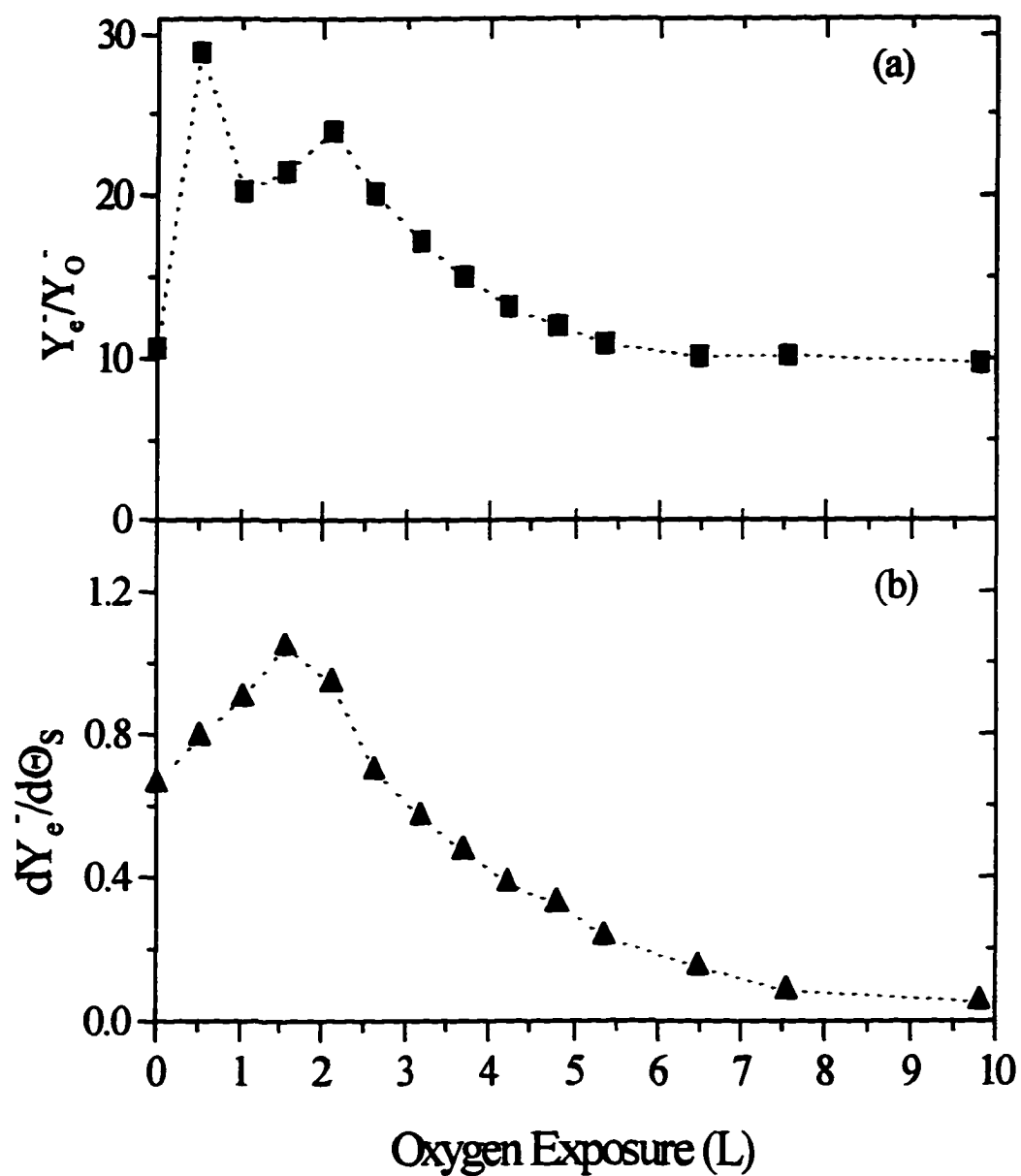**Fig. 4.19** (a) Electron-ion ratio (■), Y_e^-/Y_O^- and (b) the change in the electron yield (▲), $dY_e^-(\Theta_S)/d\Theta_S$, as a function of oxygen exposure of the Mo (100) surface at an impact energy of 400 eV.

4.2.2.2 Kinetic Energy Distributions

Normalized kinetic energy distributions for secondary electrons and O^- sputtered from Mo (100) at impact energies of 150 eV, 250 eV and 450 eV and an oxygen exposure of ~ 3 L are shown in Fig. 4.20(a - c). The ion distributions are normalized with respect to the low energy peak such that the leading edges of the distributions align, setting the zero of the energy scale. All the O^- distributions have a sharp peak at ~ 1.8 eV and a significant, low level, high energy tail. The shapes of the O^- distributions and their most probable kinetic energies are independent of impact energy as illustrated in Fig. 4.20d. As before, ion distributions for other exposures vary only in intensity of the O^-. The normalized secondary electron kinetic energy distributions are shown in Fig. 4.20(a - c) with their accompanying ion distributions. The electron distributions are normalized simply to their maxima. The electron distributions are fairly sharp, and are observed to be only weakly dependent on impact energy, peaking at 1.4 eV, 1.6 eV and 2.1 eV for impact energies of 150 eV, 250 eV and 450 eV respectively. The full width, half maxima are also observed to slightly increase with impact energy from 1.75 - 2.25 eV. Finally, similar to the ions, the amount of oxygen exposure affects only the intensity of the distributions.

4.3 Polycrystalline Molybdenum and Molybdenum (100) Discussion

4.3.1 Secondary Ion and Electron Emission

Similar to the results for the sputtering of O^- from an Al surface, the sputtered O^- kinetic energy distributions from an oxygen covered Mo surface are narrow and at low energies, unable to be accounted for by the collision cascade alone. Using the framework

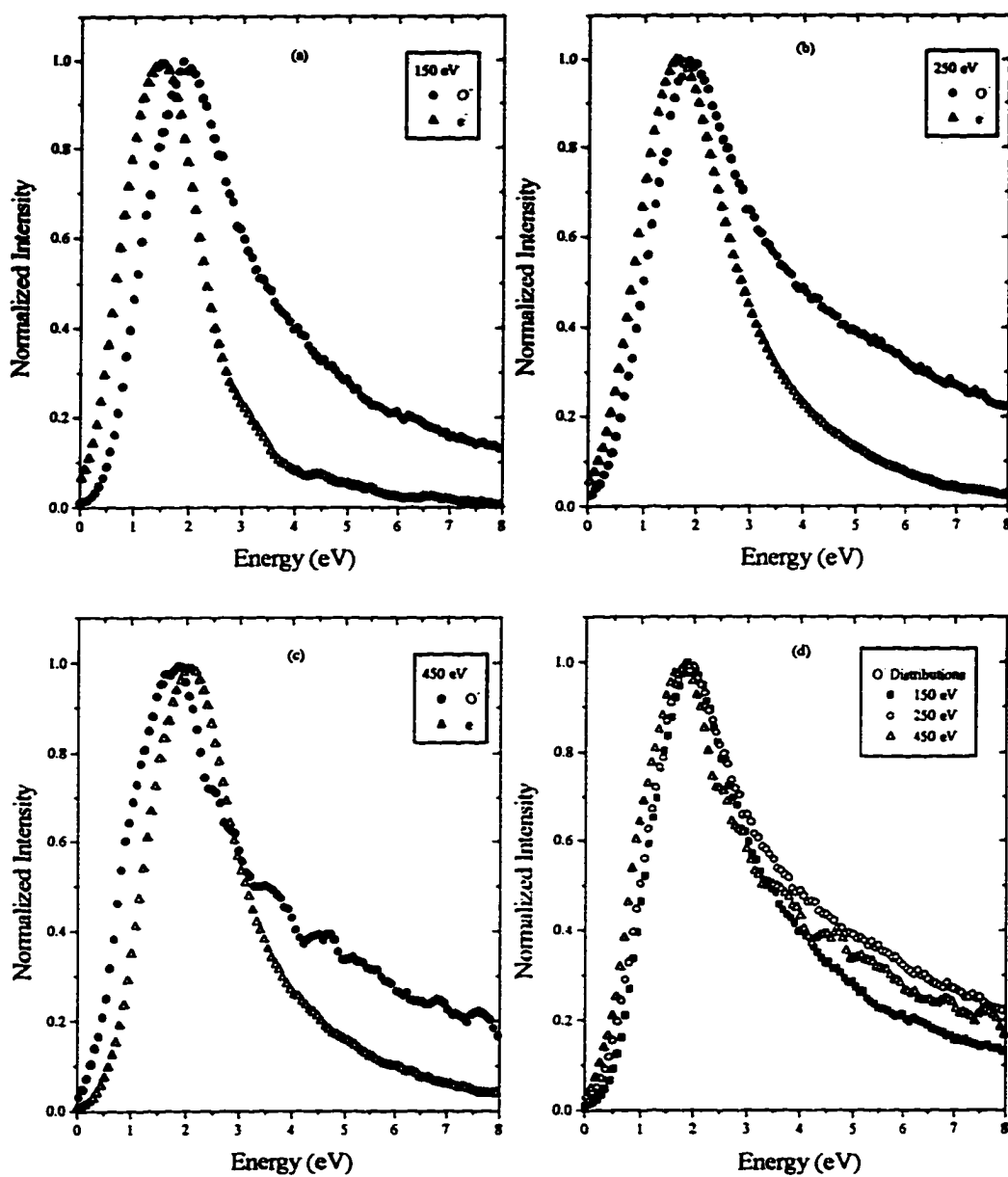**Fig. 4.20** Normalized sputtered (●) O⁻ and (△) secondary electron kinetic energy distributions for a Mo (100) surface exposed to ~ 3 L of oxygen at collision energies of (a) 150 eV, (b) 250 eV and (c) 450 eV. (d) O⁻ kinetic energy distributions for (a - c).

developed for the description of O⁻ and secondary electron emission from Al, the emission

from the Mo and Mo (100) surfaces can be accounted for by slight changes in the fitting

parameters of the model. The O⁻ kinetic energy distributions for the three impact energies

of 150 eV, 250 eV and 350 eV and the sum of the collision cascade and the excitation

mechanism distributions predicted by Eqs. 3.8 and 3.19 are shown in Fig. 4.21. The

parameters used in generating the fits are summarized in Tables 4.1 and 4.2. The sums of

the two distributions provide reasonable fits to the experimentally observed O⁻

distributions, with the collision cascade providing a portion of the high energy tail. The

relative contribution of the excitation mechanism to the collision cascade is approximately

2.0:1. The corresponding secondary electron kinetic energy distributions, predicted by

Eq. 3.22 with the parameters listed in Table 4.2, are shown with the experimental results

for impact energies of 150 eV, 250 eV and 350 eV in Fig. 4.22. Again, the model

provides quite a reasonable fit to the experimental observations.

The O⁻ kinetic energy distributions for the Mo (100) surface are quite similar to

those of the polycrystalline Mo surface and again, the distributions cannot be accounted

for by the collision cascade alone. The O⁻ kinetic energy distributions for Na⁺ impacting a

Mo (100) surface exposed to 3 L of oxygen and the theoretical distributions predicted by

Eqs. 3.8 and 3.19 are shown in Fig. 4.23 for impact energies of 150 eV, 250 eV and

450 eV. The secondary electron kinetic energy distributions for the same conditions and

the resulting electron distributions predicted by Eq. 3.22 are shown in Fig. 4.24 for each

impact energy. The parameters (summarized in Tables 4.1 and 4.2) have been adjusted to

fit the sum of the two calculated distributions to the experimentally observed O⁻
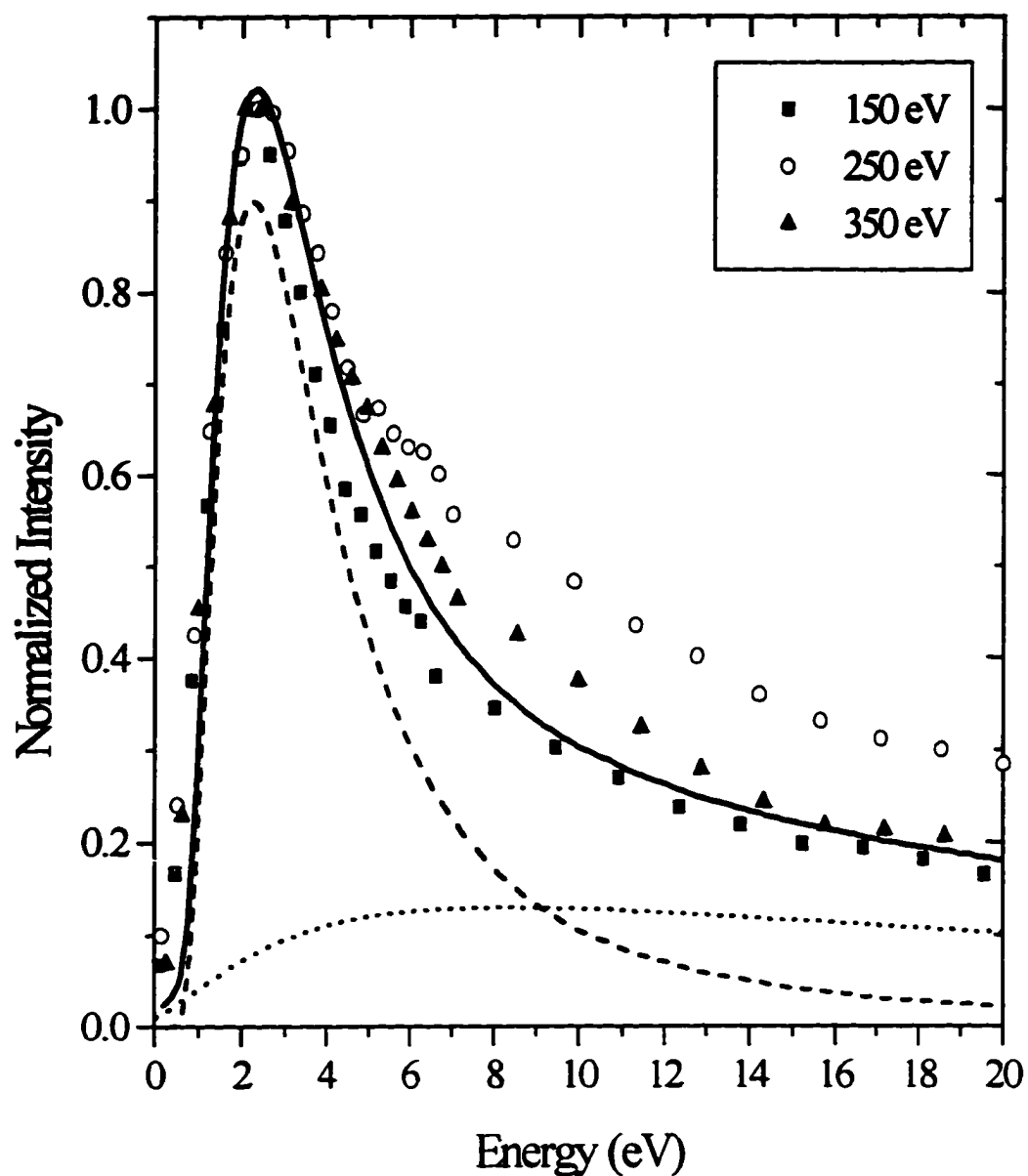
Fig. 4.21 Sputtered O⁻ kinetic energy distributions for Na⁺ impacting a polycrystalline Mo surface exposed to 10 L of oxygen at impact energies of (■) 150 eV, (○) 250 eV and (▲) 350 eV and the sum (———) of the calculated collision cascade and excitation mechanism kinetic energy distributions. Collision cascade (••••) and excitation mechanism (– – – –) kinetic energy distributions predicted by Eqs. 3.8. and 3.19 respectively. The relative contribution of the excitation mechanism to the collision cascade in the total fit is 2.0:1.

Fig. 4.22 Secondary electron kinetic energy distributions for Na⁻ impacting a polycrystalline Mo surface exposed to 10 L of oxygen at impact energies of (■) 150 eV, (○) 250 eV and (▲) 350 eV and the theoretical (——) energy distribution of the excitation mechanism predicted by Eq. 3.22.
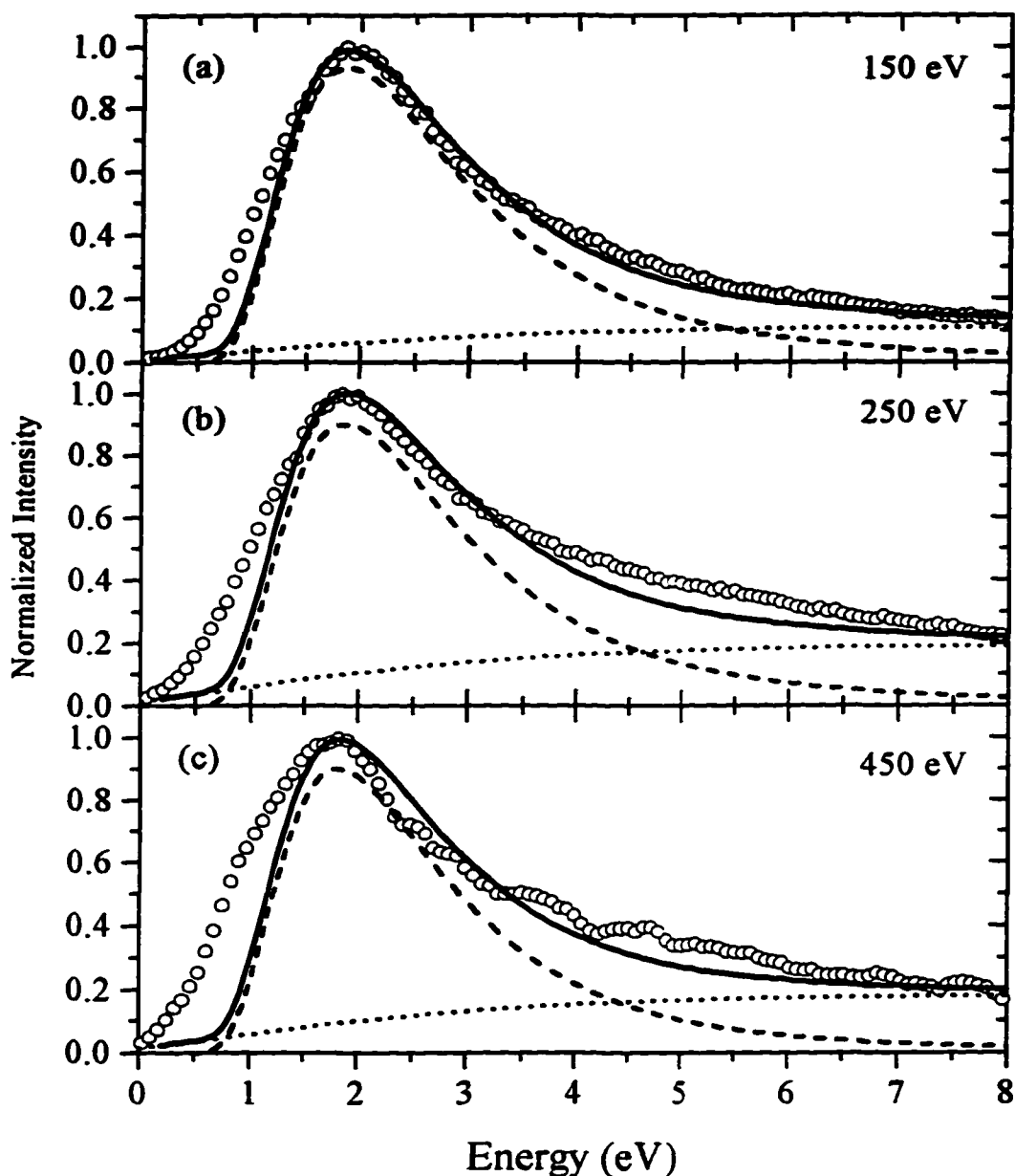
Fig. 4.23 Sputtered (O) O⁻ kinetic energy distributions for Na⁻ impacting a Mo (100) surface exposed to 3 L of oxygen at impact energies of (a) 150 eV, (b) 250 eV and (c) 450 eV and the theoretical (——) kinetic energy distributions. Collision cascade (····) and excitation mechanism (----) kinetic energy distributions predicted by Eqs. 3.8 and 3.19 respectively. The relative contributions of the excitation mechanism to the collision cascade in the total fits are (a) 3.5:1, (b) 2.0:1 and (c) 1.9:1.

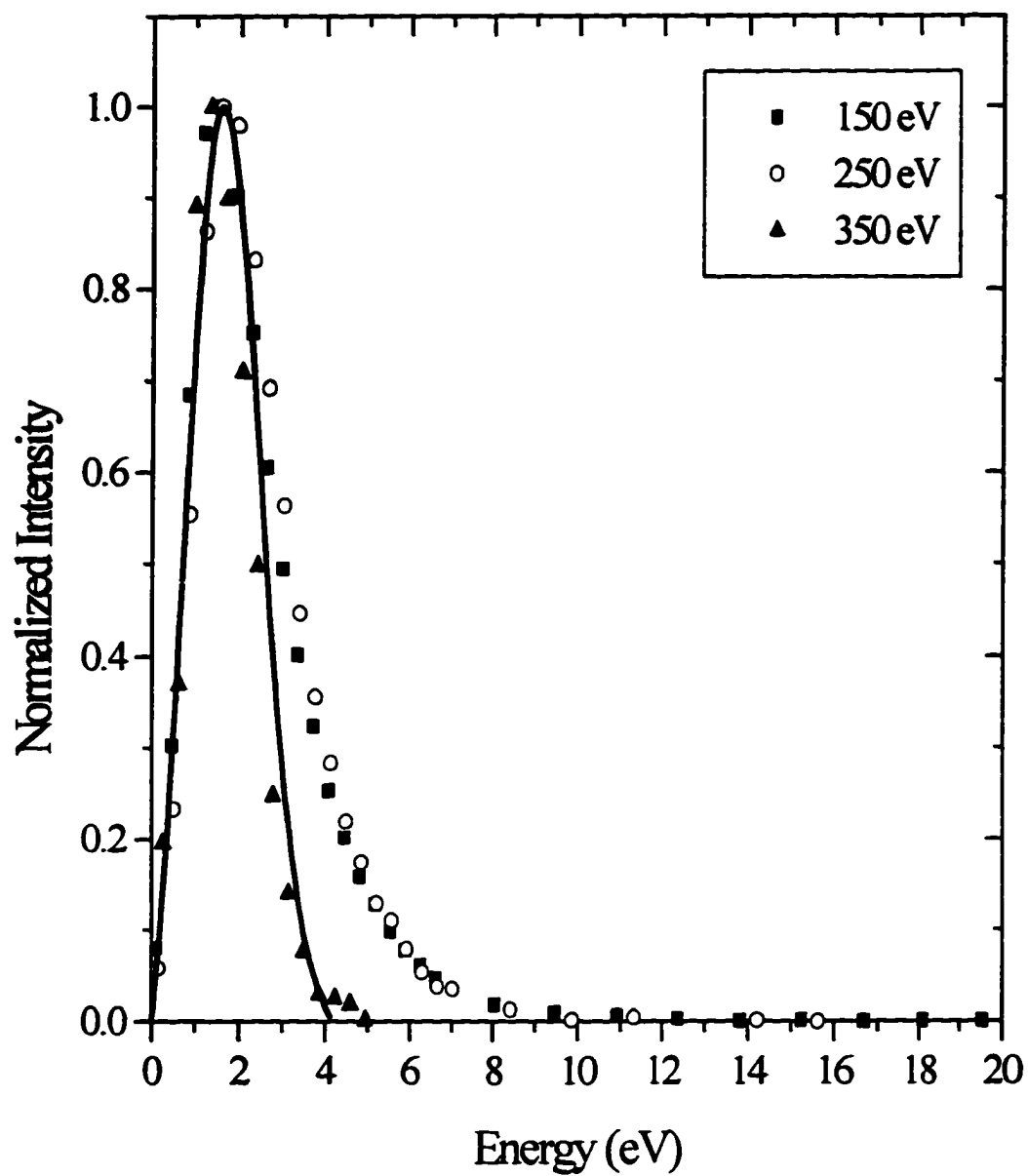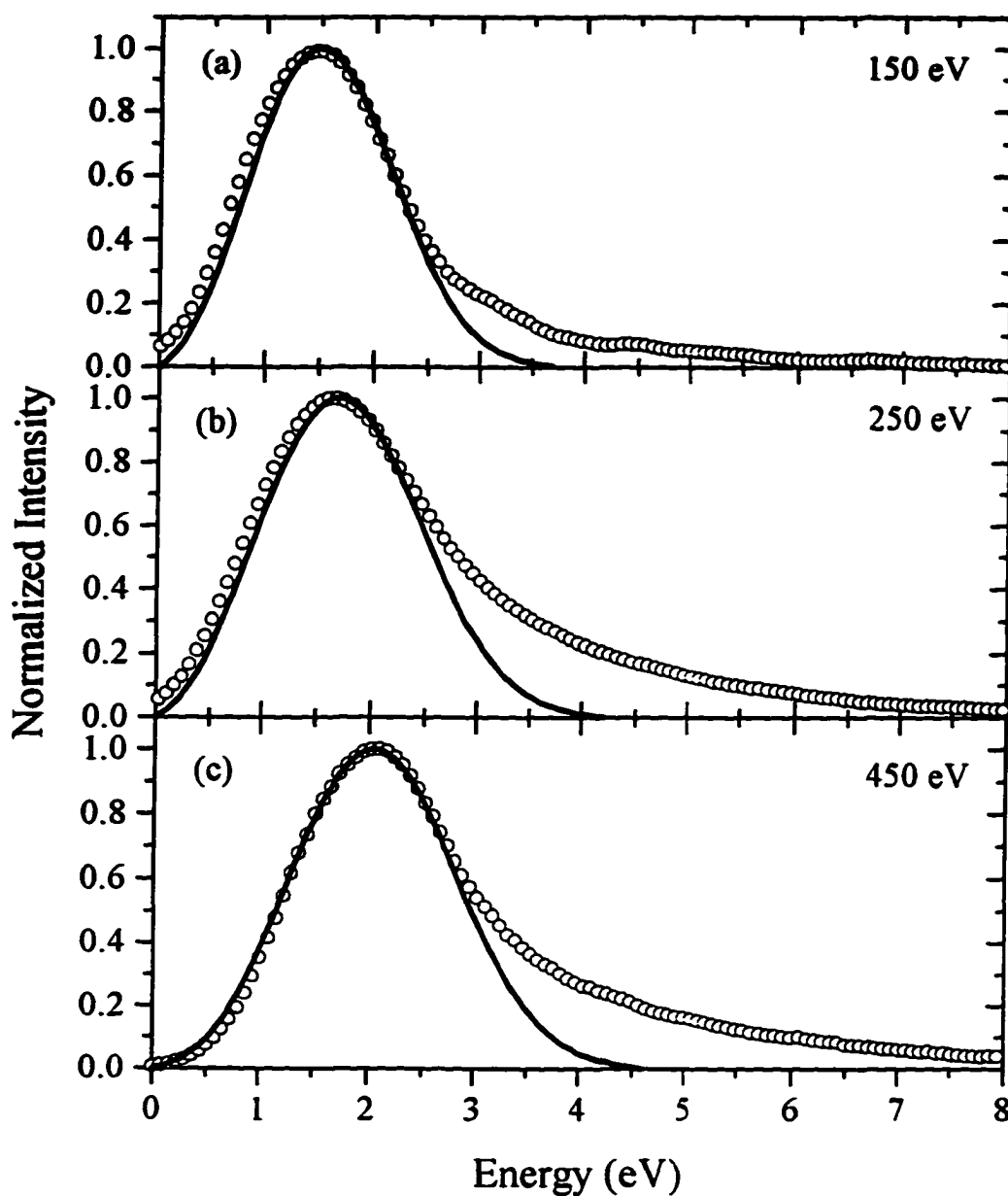**Fig. 4.24** Experimental (o) secondary electron kinetic energy distributions for Na^+ impacting a Mo (100) surface exposed to 3 L of oxygen at impact energies of (a) 150 eV, (b) 250 eV and (c) 350 eV and the theoretical (———) energy distributions of the excitation mechanism predicted by Eq. 3.22.

distribution for each impact energy. As before with the other surfaces, the collision cascade provides a portion of the high energy tail, while the excitation mechanism supplies the narrow, low energy feature and the secondary electron distribution.

Table 4.1   Collision Cascade Parameters

Parameter		Mo (poly)	Mo (100)
$m_\ell = 0$	Δ_{Mo}	2.414 eV	2.414 eV
$m_\ell = 0$	γ_M	$0.731 \ a_o^{-1}$	$0.731 \ a_o^{-1}$
$m_\ell = \pm 1$	Δ_{Mo}	3.172 eV	3.172 eV
$m_\ell = \pm 1$	γ_M	$0.630 \ a_o^{-1}$	$0.630 \ a_o^{-1}$
z_c		$3.0 \ a_o$	$3.0 \ a_o$
C		2.0 eV	2.0 eV
U		1.0 eV	1.0 eV

Table 4.2   **Excitation Mechanism Parameters**

Parameter	Mo (poly)	Mo (100) 150 eV	Mo (100) 250 eV	Mo (100) 450 eV
E_s	3.0 eV	3.0 eV	3.0 eV	3.1 eV
K_i	0.1 eV	0.1 eV	0.1 eV	0.1 eV
E_n	1.44 eV $a_o^{-\frac{1}{2}}$	1.15 eV $a_o^{-\frac{1}{2}}$	1.46 eV $a_o^{-\frac{1}{2}}$	1.76 eV $a_o^{-\frac{1}{2}}$
F_x	0.8 eV a_o^{-1}	0.75 eV a_o^{-1}	0.85 eV a_o^{-1}	0.85 eV a_o^{-1}
b	0.3 a_o^{-2}	0.5 a_o^{-2}	0.5 a_o^{-2}	0.5 a_o^{-2}
z_{eq}	3.0 a_o	3.0 a_o	3.0 a_o	3.0 a_o
z_x	5.2 a_o	5.0 a_o	5.0 a_o	5.4 a_o
Δ_{Vo}	0.0215 eV	0.0215 eV	0.0215 eV	0.0215 eV
γ_V	0.119 a_o^{-1}	0.119 a_o^{-1}	0.119 a_o^{-1}	0.2 a_o^{-1}
Δ_{Mo}	1.0 eV	1.0 eV	1.0 eV	1.0 eV
γ_M	0.9 a_o^{-1}	0.7 a_o^{-1}	0.7 a_o^{-1}	0.65 a_o^{-1}

4.3.2 Surface Comparison

The similarity of the results for the Mo and the Mo (100) surfaces is remarkable considering the disorder of the polycrystalline surface relative to the (100) surface. The oxygen adsorption sites on the (100) surface are uniform, independent of the amount of oxygen exposure. Though oxygen forms different, ordered structures with surface Mo atoms at low and high coverages, both structures provide the same oxygen adsorption sites. The polycrystalline surface, in addition to multiple crystal surfaces, has crystal grain boundaries, fissures and numerous other defects which all provide excellent oxygen adsorption sites, which may be vastly different from those on the Mo (100) surface. Despite these differences, the kinetic energy distributions for the two surfaces are essentially the same, both in the shapes and most probable kinetic energies of the distributions. These distributions also are, for the most part, independent of impact energy and oxygen coverage of the surface. Additionally, the absolute yields of both the negative ions and the electrons at the same oxygen exposure are approximately equal in magnitude. These facts suggest that the mechanism by which O^- and secondary electrons are ejected from the surface, initiated by the impact of a low ionization potential, low energy ion, is the result of a molecular excitation. In short, for significant secondary electron and negative ion emission, there must be oxygen on the metal's surface, but, to first order, it does not matter where the oxygen is adsorbed nor how it is bound.

Though there is not enough information known about the diatomic Mo-O system to present a molecular diagram representing the ion-surface interaction, it is of interest to examine the parameters used in the excitation model to fit the Mo and Mo (100) results in

relation to those for Al. First, a slight decrease in the equilibrium distance, z_{eq}, $(z_{eq}(Al) = 3.17\ a_o$ and $z_{eq}(Mo) = 3.0\ a_o)$ is consistent with the slightly higher work function of the Mo surfaces $(\phi(Al) = 4.2\ eV$ and $\phi(Mo) = 4.6\ eV)$. Second, the increase in the energy at the most probable excitation distance, $E_s(z_{eq})$, $(E_s(Al) = 1.4\ eV$, $E_s(Mo) \approx 3.0\ eV)$ and the shifting of the crossing point, z_x, of the molecular curves farther from the surface $(z_x(Al) = 7.5\ a_o$, $z_x(Mo) \approx 10\ a_o)$ would result in an upward shift in energy of the whole $(MoO^-)^*$ curve compared to that for $(AlO^-)^*$. The bond strength of the diatomic MoO molecule is $\sim 5.0\ eV$ $(D_o^o(Al) = 5.27\ eV)$, and thus the potential curve for MoO would be expected to be similar to that for AlO. Thus, in a low energy collision, O^- is less likely to be excited to the higher excitation energy, $E_s \sim 3.0\ eV$, above the vacuum level (required to fit the results for the Mo and Mo (100) surfaces) and accordingly, a lower absolute yield of O^- can be expected compared to Al. Interestingly, this is in fact observed to be the case.

In conclusion, the results for the three metal surfaces studied here are quite similar and the differences in the parameters required to fit the observed kinetic energy distributions are in agreement with the macroscopic differences between Al/O and Mo/O. For all of the surfaces, an energetic threshold of 40 -50 eV is observed for secondary electron and negative ion emission. In the excitation mechanism, the common threshold would depend upon the probability for excitation of the $(AlO^-)_{surface}$ or the $(MoO^-)_{surface}$. Cross sections for these excitation processes have not been measured, but they can be expected to be sharply increasing functions of energy for collision energies up to 1 keV. Finally, it is clear that adsorbed oxygen leads to a significant increase in secondary

electron and negative ion emission from metal surfaces during low energy bombardment by low ionization potential ions. For each surface, the adsorbed oxygen leads to an order of magnitude increase in Y_e^- at low impact energies, and though the uptake of oxygen by the Al surface may be slower by a factor of $\sim$ 10, the yields have essentially the same dependence on oxygen *coverage*.

CHAPTER 5

CONCLUSIONS

The scope of this investigation was to examine collision-induced, secondary electron and negative ion emission processes from adsorbate-covered, metal surfaces. Specifically, the initial intention was to answer three simple questions. First, why and to what extent does oxygen on a metal surface lead to an increase in the secondary electron coefficient? Second, by what process does the impact of a low ionization potential positive ion with this surface, eject an electron into the vacuum during the low energy collision? And third, could conventional models for the sputtering of ions from metals be used to describe the sputtering of negative ions from an adsorbed oxygen layer on a metal surface? To pursue these goals, experiments were performed on well-characterized, vacuum prepared metal surfaces with controlled amounts of oxygen coverage. In practice, the surface of every device is covered to some extent with oxygen which can affect secondary emission processes rather dramatically, *viz.*, the yield of electrons from oxygen covered surface can be several orders of magnitude greater than that from a clean surface. Therefore, developing an understanding of the role that oxygen plays in the dynamics of these emission processes and quantifying the effect of coverage on the emission is vital to any process involving the interaction of energetic particles with surfaces.

The absolute yields and kinetic energy distributions of negative ions and secondary electrons for collisions of positive sodium ions with polycrystalline aluminum and molybdenum and molybdenum (100) surfaces have been measured as a function of the

111

oxygen coverage for impact energies below 500 eV. The results of these experiments allow for some general conclusions about secondary electron and negative ion emission from low energy collisions of low ionization potential ions with metal surfaces to be made. First, it is clear that when there is adsorbed oxygen on metal surfaces, the secondary electron and negative ion emission resulting from collisions of low energy ions with those surfaces can be significant. Without the oxygen on the surface, there is essentially no electron emission. Second, the predominant negative ion species sputtered from a metal surface with up to a few monolayers of oxygen coverage is O^-. Third, the energy distribution of the sputtered O^- is characterized by a sharp, low energy peak followed by a low level, high energy tail. Both the shape and the most probable kinetic energy of these distributions are independent of impact energy and oxygen coverage. Finally, the secondary electrons ejected from the surface have a narrow energy distribution (FWHM $\leq$ 2 eV) centered at approximately the most probable kinetic energy of the ions. Similar to O^-, the shape of the distribution and most probable kinetic energy of the secondary electrons are independent of both the collision energy and oxygen coverage of the surface.

The source of the secondary electrons observed in these experiments cannot be from potential emission since the ionization potential of Na (5.1 eV) is much less than twice the work function of Al ($\sim$ 4.2 eV) or Mo ($\sim$ 4.6 eV). Nor is it likely that the electrons come from direct kinetic emission due to the improbability of kinetic emission at these low impact energies. The lack of any discreet structure in the secondary electron kinetic energy distributions suggests that the electrons do not arise from the autoionizing O^{**} or autodetaching $(O^-)^*$. Other possible sources of secondary electron emission were

investigated, including the correlated, simultaneous emission of both an electron and a negative ion. However, an exhaustive time-of-flight autocorrelation study showed no evidence of the simultaneous emission of negative ions and electrons. Thus, the secondary electrons must come from another emission mechanism with a strong dependence on the amount of oxygen coverage on the surface.

The sputtering of oxygen negative ions from the three surfaces also provided some difficulties when trying to describe the sputtering event in terms of a conventional collision cascade. The sputtering of O^- from an Al surface provided an excellent opportunity to apply the collision cascade theory since the O^- affinity level widths, needed to calculate the survival probabilities, had been calculated specifically for the O^- in front of an Al surface [51]. Theoretical kinetic energy distributions for the surviving O^- ions, sputtered by the collision cascade, were calculated, however the calculated distributions bear little resemblance to the experimental observations. The maximum in the distribution function, calculated with the collision cascade model, occurs at much higher kinetic energies than are observed, and there are no plausible parameter adjustments which can bring the calculation into accord with the observations. The inadequacy of the conventional description also was evident in attempting to model the low energy sputtering of O^- from the Mo surfaces. Thus, while the conventional collision cascade model may provide a fair description of the sputtering event for neutral atoms at high collision energies, it does not adequately describe the low energy sputtering of O^- from metal surfaces.

The lack of a suitable description for low energy secondary electron emission and the sputtering of negative ions lead us to propose an excitation/desorption mechanism to

augment the collision cascade and to provide a mechanism for secondary electron emission. Several features, most notably, the invariance of the electron and ion kinetic energy distributions with impact energy and the similarity of the most probable kinetic energy, lend support to the suggested mechanism. In the model, O^- is collisionally excited into an $(AlO^-)^*$ $\{(MoO^-)^*\}$ repulsive state, and then the negative ion can exit the surface, or it can decay by electron emission to the metal or by electron emission to the vacuum. The resulting kinetic energy distribution of the ions desorbing via this mechanism, together with the distribution generated by the collision cascade, can provide a reasonable fit to the observed ion kinetic energy distribution. This mechanism also provides for the possibility of secondary electron emission through the decay of O^- by emission to the vacuum. The resulting secondary electron kinetic energy distribution can be calculated, providing a reasonable fit to the experimental observations. The simple molecular curves used in the model are clearly representative of a whole family of potential curves and are only intended to be a representation of the true ion-surface interaction, and the parameters used in fitting the results are non-unique. Yet, with plausible estimations, both the negative ion and secondary electron kinetic energy distributions can be easily reproduced. The differences in the parameters used in fitting the electron and ion distributions are consistent with the properties of the Al and Mo surfaces.

As an illustration of the feasibility of the excitation mechanism, the absolute survival probabilities predicted by the excitation mechanism can be compared to the experimental results for a Mo (100) surface with ~ 1 ML O atom coverage at an impact energy of 250 eV. The experimentally measured yields are: $Y_{O^-} = 0.5\%$ and $Y_{e^-} = 0.8\%$.

The fit for the ion kinetic energy distribution indicates that the relative contribution of the excitation mechanism to the collision cascade in the total fit is approximately 2:1. Thus, the oxygen negative ion yield due to the exciation mechanism can be estimated to be, $Y_O^-(ex) \approx 0.33\%$. The survival probability can be integrated to obtain the theoretical total survival probability for the ions,

$$P_{ion}^{ex} = \int_0^\infty S_{ion}^{ex}(E)dE = 2.3\%, \qquad (5.1)$$

and for the secondary electrons,

$$P_e^{ex} = \int_0^\infty S_{ion}^{ex}(E)dE = 9.2\%. \qquad (5.2)$$

The surface unit cell for the Mo (100) surface has an area of ~ 10 Å^2, and therefore, at 1 ML O coverage, there is roughly 1 O atom per unit cell adsorbed on the surface. Though the cross sections for excitation have never been measured specifically for this projectile-target system, they are typically of the order of a few Å^2 (1 - 3 Å^2) at these collision energies. So, taking $\sigma_{ex} = 1.5$ Å^2, the predicted yields due to the excitation mechanism would be:

$$Y_O^-(\text{theoretical}) = \left(\frac{\sigma_{ex}}{10 Å^2} \right) \cdot P_{ion}^{ex} = 0.34\%, \qquad (5.3)$$

and

$$Y_e^-(\text{theoretical}) = \left(\frac{\sigma_{ex}}{10\,\text{Å}^2}\right) \cdot P_e^{ex} = 1.4\%. \qquad (5.4)$$

These predicted yields are in quite reasonable agreement with the exprimentally measured yields both in magnitude and in the ratio of electrons to ions.

Additionally, the model also predicts the different dependence of the yields on the work function of the surface. In the model, a decrease in the work function corresponds to an increase in the equlibrium distance, z_{eq}, from the surface as shown in Fig. 5.1. For example, let us use the parameters for the Mo (100) surface at an impact energy of 250 eV and assume a decrease in the work function of the surface, $\Delta\phi = \phi - \phi' \approx 0.4$ eV, such that z_{eq} increases from 3.0 a_o to 3.5 a_o. The total integrated survival probability for the ions increases 65 % while that for the secondary electrons increases only 14 % as the equilibrium distance is increased from 3.0 a_o to 3.5 a_o. Thus, changes in the work function have a greater effect on the negative ion emission which is in fact, observed to be the case as seen in Figs. 4.5b and 4.5d.

Further investigation of the excitation/desorption mechanism will come through other experiments involving excitation of the O^- residing on the surface by other means. One possibility is through the photoexcitation (photodesorption) of O^- by UV photons in the range of 5 - 10 eV. Preliminary investigations in this lab indicate that ~ 5.4 eV UV photons are just barely able to photoexcite and desorb O^- from the Mo (100) surface (partially covered with Na to minimize ϕ). However, the flux of photodesorbed O^- is
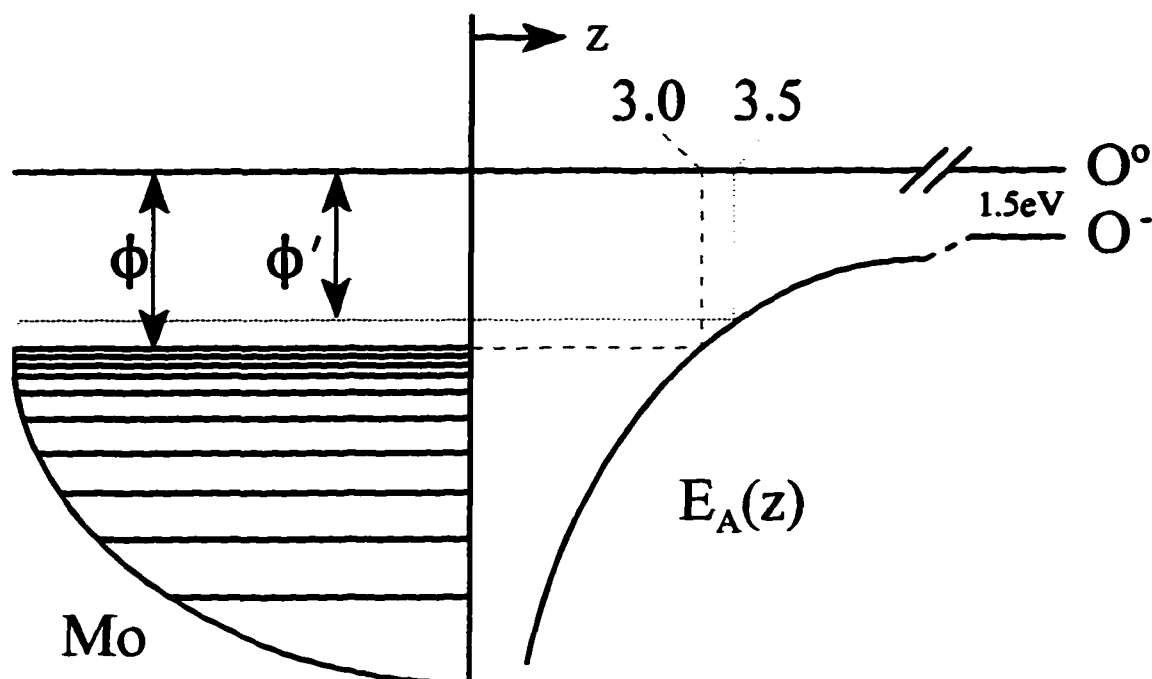
Fig. 5.1 Relationship between the change in the work function, $\Delta\phi = \phi - \phi'$, and the equilibrium distance, z_{eq}.

insufficient to make measurements of their kinetic energies practical with the present equipment. A higher intensity light source providing a continuous spectra of UV photons will be needed to provide adequate photoexcitation of the AlO^- (MoO^-) leading to the desorption of O^-. Excitation also could be provided by bombarding the surface with fast neutral atoms, and presumably the relative yields and kinetic energy distributions would be largely unaffected. Absolute yield measurements of the secondary electrons and the negative ions, generated by collisions of fast neutrals with the surface, would be difficult owing to the fact that determining the absolute number of neutrals arriving at the surface is not an easy task. On the other hand, kinetic energy distributions of the ions and

electrons can be determined in the present apparatus for collisions of Ar^o with the surface for energies possibly as low as ~ 500 eV.

Finally, the similarity of the results for the three surfaces, namely the dependence of the yields on oxygen coverage, the similar shapes and kinetic energies of the ion and electron energy distributions and the invariance of these distributions with both impact energy and oxygen coverage is remarkable. Though the emission from the surfaces may vary in magnitude, the fact that the kinetic energy distributions of the ions and electrons are unchanged suggests that they are ejected from the surface by a common process. Different macroscopic properties of the surfaces, e.g., the work functions, affect the magnitude of ion emission, but they have a somewhat lesser effect on secondary electron emission. Adsorbed oxygen on the surface of a metal, independent of that substrate, significantly affects the low energy, ion-induced secondary electron emission.

The proposed desorption mechanism also can be used to describe the secondary electron and negative ion emission from a metal surface with other electronegative adsorbates such as chlorine. If chlorine was adsorbed on the surface, and it was desorbed through the excitation mechanism, one might expect a smaller electron-negative ion ratio owing to the higher electron affinity of Cl^- compared to O^-. Presumably, the width for electron emission to the vacuum would be smaller (than that for O^-), and the majority of the Cl^- exiting the surface would survive its journey into the vacuum as a negative ion. During these experiments, a limited effort was made with the Al surface to investigate the possible effects of other adsorbates (CO_2 and H_2S but not Cl_2) on secondary emission, and they seemed to have little effect on the emission. In order to develop a practical

understanding of ion and electron emission for other adsorbates, information about the adsorption (sticking coefficient, dissociation, etc.) and how that adsorbate interacts with atoms of the substrate, must be known.

It is clear that surface conditions dominate the ion-induced emission as evidenced by the time and care which is absolutely essential to produce clean, well-characterized surfaces and reproducible results in an ultrahigh vacuum environment. Without this surface preparation and careful control of the conditions thereafter, even relatively simple experiments, such as yield measurements, could have never been repeated. Perhaps the challenges faced in preparing experimentally suitable surfaces and then ultimately understanding the interactions of ions, atoms and electrons with those surfaces are because, as Wolfgang Pauli knew, "the surface was invented by the devil."

REFERENCES

[1] G. Lakits, F. Aumayr, M. Heim and H. Winter, Phys. Rev. A **42**, 5780 (1990).

[2] H. Winter, F. Aumayr and G. Lakits, Nucl. Instrum. Methods B **58**, 301 (1991).

[3] H. Brenten, H. Müller and V. Kempter, Surf. Sci. **271**, 103 (1992).

[4] E.V. Alonso, M.A. Alurralde and R.A. Baragiola, Surf. Sci. **166**, L155 (1986).

[5] R.A. Baragiola, in: *Low Energy Ion-Surface Interactions*, edited by J.W. Rabalais (Wiley, New York, 1993).

[6] J.C. Tucek, S.G. Walton and R.L. Champion, Phys. Rev. B **53**, 14127 (1996).

[7] D.H. Baker, L.D. Doverspike and R.L. Champion, Phys. Rev. A **46**, 296 (1992).

[8] J. Ferrón, E.V. Alonso, R.A. Baragiola and A. Olivia-Florio, Surf. Sci. **120**, 427 (1982).

[9] P.C. Smith, B. Hu and D.N. Ruzic, J. Vac. Sci. Technol. A **12**, 2692 (1994).

[10] K. Wittmaack, Surf. Sci. **112**, 168 (1981).

[11] R.A. Baragiola, J. Ferrón and G. Zampieri, Nucl. Instrum. Methods B **2**, 614 (1984).

[12] M.L. Yu, Phys. Rev. Lett. **40**, 574 (1978); Phys. Rev. B **26**, 4731 (1982).

[13] M. Bernheim and F. Le Bourse, Nucl. Instrum. Methods B **27**, 94 (1987).

[14] B. Svensson and G. Holmén, J. Appl. Phys. **52**, 6928 (1981).

[15] *Sputtering by Particle Bombardment I*, edited by R. Behrisch (Springer-Verlag, Berlin, 1981).

[16] *Sputtering by Paritcle Bombardment III*, edited by R. Behrisch and K. Wittmaack (Springer-Verlag, Berlin, 1991).

[17] M. Urbassek, Nucl. Instrum. Methods B **4**, 356 (1984).

[18] R.A. Brizzolara, C.B. Cooper and T.K. Olson, Nucl. Instrum. Methods B **35**, 36 (1988).

[19] M. Kaminsky, *Atomic and Ionic Impact Phenomena on Metal Surfaces*, (Academic, New York, 1965), p. 263ff.

[20] R.A. Baragiola, Rad. Effects **61**, 47 (1982).

[21] E.W. Thomas, Vacuum **34**, 1031 (1984).

[22] S. Valeri, Surf. Sci. Repts. **17**, 85 (1993).

[23] W.R. Grove, Philos. Mag. **5**, 203 (1858).

[24] J.P. Gassiot, Philos. Trans. R. Soc. London **148**, 1 (1858).

[25] J. Plücker, Ann. Phys. (Leipzig) **103**, 88 (1858).

[26] A. Günterschulze, J. Vac. Sci. Technol. **3**, 360 (1953).

[27] M.W. Thompson, Philos. Mag. **18**, 377 (1968).

[28] P. Sigmund, in Ref. [12].

[29] A. Blandin, A. Nourtier and D.W. Hone, J. Phys. **37**, 396 (1976).

[30] G. Blaise and A. Nourtier, Surf. Sci. **90**, 495 (1979).

[31] J.K. Nørskov and B.I. Lundqvist, Phys. Rev. B **19**, 5661 (1979).

[32] R. Brako and D.M. Newns, Surf. Sci. **108**, 253 (1981).

[33] N.D. Lang, Phys. Rev. B **27**, 2019 (1983).

[34] N.D. Lang and J.K. Nørskov, Physica Scripta T **6**, 15 (1983).

[35] M.L. Yu and N.D. Lang, Nucl. Instrum. Methods B **14**, 403 (1986).

[36] M.L. Yu, Phys. Rev. Lett. **47**, 1325 (1981).

[37] E. Stoffels, W. W. Stoffels, D. Vender, M. Kando, G. M. W. Kroesen and F. J. de Hoog, Phys. Rev. E **51**, 2425 (1995).

[38] H. You, N. M. D. Brown and K. Al-Assadi, Surf. Sci. **284**, 263 (1993).

[39] M. Saitoh, K. Kanazawa, T. Momose, H. Ishimaru, N. Ota and J. Uramoto, J. Vac. Sci. Technol. A 11, 2518 (1993).

[40] J. Kawata, K. Ohya and I. Mori, Jap. J. Appl. Phys. 31, 1453 (1992); Jap. J. Appl. Phys. 31, 2560 (1992).

[41] W. Eckstein, W. von der Linden and V. Dose, Nucl. Instrum. Methods B 95, 14 (1995).

[42] M.B. Hendricks, P.C. Smith, D.N. Ruzic, A. Leybovich and J.E. Poole, J. Vac. Sci.Technol. A 12, 1408 (1994).

[43] Z. Q. Xie and C. M. Lyneis, Rev. Sci. Instrum. 65, 2947 (1994).

[44] P. J. Hargis, et al., Rev. Sci. Instrum. 65, 140 (1994).

[45] J. K. Olthoff, R. J. Van Brunt, S. B. Radovanov, J. A. Rees and R. Surowiec, J. Appl. Phys. 75, 115 (1994).

[46] G. Drechsler, C.-Bässmann, W.-D. v. Fraunberg, U. Boesl and E. W. Schlag, Rev. Sci. Instrum. 65, 3172 (1994).

[47] J. H. Arps, M. E. Miklis and R. A. Weller, Rev. Sci. Instrum. 65, 1575 (1994).

[48] V. Dangendorf, A. Demian, H. Friedrich, V. Wagner, A. Akkerman, A. Breskin, R. Chechik and A. Gibrekhterman, Nucl. Instrum. Methods A 350, 503 (1994).

[49] J. L. Allen, S. L. Espy, Y. Yao, I. F. Urazgil'din, R. G. Albridge, A. V. Barnes and N.H. Tolk, Bull. Rus. Acad. Sci. 58, 887 (1994).

[50] I.P. Batra and L. Kleinman, J. Electron Spectrosc. Relat. Phenom. 33, 175 (1984).

[51] B. Bahrim, D. Teillet-Billy and J.P. Gauyacq, Phys. Rev. B 50, 7860 (1994); Surf. Sci. 316, 189 (1994).

[52] Spectra-Mat Corp., Watsonville, CA.

[53] Idaho National Engineering Laboratory, Boise, ID.

[54] Johnson Matthey, Ward Hill, MA.

[55] Aldrich Chemical Company, Inc., Milwaukee, WI.

[56] Aithaca Chemical Corp., Uniondale, NY.

[57] W.H. Krueger and S.R. Pollack, Surf. Sci. **30**, 263 (1972).

[58] V.K. Agarwala and T. Fort, Surf. Sci. **45**, 470 (1974).

[59] P.H. Dawson, Surf. Sci. **57**, 229 (1976).

[60] D.J. O'Connor, E.R. Wouters, A.W. Denier van der Gon, J. Vrijmoeth, P.M. Zagwijn, W.F J. Slijkerman, J.W.M. Frenken, and J.F. van der Veen, Surf. Sci. **287/288**, 438 (1993).

[61] A.M. Bradshaw, P. Hofmann, and W. Wyrobisch, Surf. Sci. **68**, 269 (1977).

[62] V.A. Esaulov, L. Guillemot and S. Lacombe, Nucl. Instrum. Methods B **90**, 305 (1994).

[63] Y. Yamauchi and R. Shimizu, Jpn. J. of Appl. Phys. **22**, L227 (1983).

[64] Y. Yamamura, T. Takiguchi and H. Kimura, Nucl. Instrum. Methods B **78**, 337 (1993).

[65] W. Eckstein, C. García-Rosales, J. Roth and J. Lásló, Nucl. Instrum. Methods B **83**, 95 (1993).

[66] D.J. Oostra, R.P. van Ingen, A. Haring, A.E. de Vries and F. W. Saris, Phys. Rev. Lett. **61**, 1392 (1988).

[67] F. Penent, J.P. Grouard, R.I. Hall, J.L. Montmagnon, R.L. Champion, L.D. Doverspike and V.A. Esaulov, J. Phys. B: At. Mol. Phys. **20**, 6065 (1987).

[68] D. Spence, Phys. Rev. A **12**, 721 (1975).

[69] R. Riwan, C. Guillot and J. Paigne, Surf. Sci. **47**, 183 (1975).

[70] H. Xu and K.Y.Simon Ng, Surf. Sci. **356**, 19 (1996).

VITA

John Christopher Tucek

Born in Plainfield, New Jersey, on October 30, 1969 to John R. and Arlene N. Tucek. Graduated from North Allegheny High School, Wexford, Pennsylvania in June 1988. Graduated from the University of Notre Dame, Notre Dame, Indiana with his Bachelor of Science in physics, May 1992. Received his Master of Science in physics from the College of William and Mary, Williamsburg, Virginia in May 1994. Completed the requirements for the Doctor of Philosophy degree at the College of William and Mary, Williamsburg, Virginia on June 20, 1997.